

SYNTHESIS OF BLACK TITANIUM DIOXIDE AND EFFECT OF CALCINATION CONDITIONS
AND REDUCING AGENT ON PHOTOCATALYTIC DEGRADATION OF METHYL ORANGE



A Thesis Submitted in Partial Fulfillment of the Requirements
for the Degree of Master of Engineering in Chemical Engineering

Department of Chemical Engineering

Faculty of Engineering

Chulalongkorn University

Academic Year 2018

Copyright of Chulalongkorn University

การสังเคราะห์แบคทีโอเทเนียมไดออกไซด์และผลของสภาวะการเผาและตัวรีดิวซ์ต่อการสลายสีย้อม
เมทิลออเรนจ์ที่เร่งปฏิกิริยาด้วยแสง



วิทยานิพนธ์นี้เป็นส่วนหนึ่งของการศึกษาตามหลักสูตรปริญญาวิศวกรรมศาสตรมหาบัณฑิต
สาขาวิชาวิศวกรรมเคมี ภาควิชาวิศวกรรมเคมี
คณะวิศวกรรมศาสตร์ จุฬาลงกรณ์มหาวิทยาลัย
ปีการศึกษา 2561
ลิขสิทธิ์ของจุฬาลงกรณ์มหาวิทยาลัย

Thesis Title	SYNTHESIS OF BLACK TITANIUM DIOXIDE AND EFFECT OF CALCINATION CONDITIONS AND REDUCING AGENT ON PHOTOCATALYTIC DEGRADATION OF METHYL ORANGE
By	Mr. Saran Saensook
Field of Study	Chemical Engineering
Thesis Advisor	Akawat Sirisuk, Ph.D.

Accepted by the Faculty of Engineering, Chulalongkorn University in Partial
Fulfillment of the Requirement for the Master of Engineering

..... Dean of the Faculty of Engineering
(Associate Professor SUPOT TEACHAVORASINSKUN,
D.Eng.)

THESIS COMMITTEE

..... Chairman
(Associate Professor TAWATCHAI CHARINPANITKUL, Ph.D.)

..... Thesis Advisor
(Akawat Sirisuk, Ph.D.)

..... Examiner
(Associate Professor KASIDIT NOOTONG, Ph.D.)

..... External Examiner
(Assistant Professor Soipatta Soisuwan, Ph.D.)

ศรัณญ์ แสนสุข : การสังเคราะห์แบล็คไทเทเนียมไดออกไซด์และผลของสภาวะการเผาและตัวรีดิวซ์ต่อการสลายสีย้อมเมทิลออเรนจ์ที่เร่งปฏิกิริยาด้วยแสง. (SYNTHESIS OF BLACK TITANIUM DIOXIDE AND EFFECT OF CALCINATION CONDITIONS AND REDUCING AGENT ON PHOTOCATALYTIC DEGRADATION OF METHYL ORANGE) อ.ที่ปรึกษาหลัก : อ. ดร.อัครวัต ศิริสุข

งานวิจัยนี้ได้ทำการศึกษาการสังเคราะห์และการประยุกต์ใช้ตัวเร่งปฏิกิริยาแบล็คไทเทเนียมไดออกไซด์ในการสลายสารละลายสีย้อมเมทิลออเรนจ์ด้วยแสง โดยนำตัวเร่งปฏิกิริยาไทเทเนียมไดออกไซด์ที่เตรียมด้วยวิธีการโซลเจล จากนั้นใช้โซเดียมโบโรไฮไดรด์เป็นตัวรีดิวซ์เพื่อที่จะสังเคราะห์แบล็คไทเทเนียมไดออกไซด์ จึงได้ทำการออกแบบสภาวะการสังเคราะห์ตัวเร่งปฏิกิริยาเป็นแบบ 2x2x3 แฟกทอเรียล เพื่อประเมินนัยสำคัญของปัจจัยที่ใช้ในการสังเคราะห์ ดังนี้ (1) อุณหภูมิการเผา (400 และ 500 องศาเซลเซียส); (2) เวลาการเผา (5 และ 10 ชั่วโมง); และ (3) สัดส่วนเชิงโมลของโซเดียมโบโรไฮไดรด์ที่ใช้ต่อไทเทเนียมไดออกไซด์ (0:1, 0.5:1 และ 1:1 ตามลำดับ) ค่าการกำจัดสารละลายสีย้อมเมทิลออเรนจ์ภายใต้แสงยูวีและแสงวิสิเบิลเป็นตัวตอบสนองสำหรับการวิเคราะห์ความแปรปรวนทางสถิติ ก่อนทำการทดลองการเร่งปฏิกิริยาด้วยแสง ตัวเร่งปฏิกิริยาถูกกวนในที่มืดเป็นเวลา 1 ชั่วโมง จากนั้นทดลองภายใต้แสงยูวีและแสงวิสิเบิลเป็นเวลา 3 ชั่วโมง และทำการวัดความเข้มข้นของเมทิลออเรนจ์ด้วยเครื่อง UV-Vis spectrophotometer จากผลการทดลองพบว่า ตัวเร่งปฏิกิริยาแบล็คไทเทเนียมไดออกไซด์ที่ทำการเผาที่อุณหภูมิ 500 องศาเซลเซียส เป็นเวลา 10 ชั่วโมง โดยสัดส่วนเชิงโมลของโซเดียมโบโรไฮไดรด์ต่อไทเทเนียมไดออกไซด์เท่ากับ 1:1 ให้ค่าประสิทธิภาพสูงสุดที่ร้อยละ 82.17 ภายใต้แสงยูวีและร้อยละ 71.92 ภายใต้แสงวิสิเบิล เป็นผลมาจากการที่ตัวเร่งปฏิกิริยาที่สังเคราะห์ได้มีความไม่สมบูรณ์แบบตามผิวหน้าอยู่มาก ซึ่งเป็นตัวดักจับอิเล็กตรอนบนพื้นผิวของตัวเร่งปฏิกิริยา มันจะช่วยลดการกลับมารวมกันของคู่อิเล็กตรอนและโฮล อีกทั้งสามารถลดช่องว่างของระดับชั้นพลังงานและมีความสามารถในการดูดซับแสงในช่วงวิสิเบิลได้มากขึ้น ส่งผลให้เกิดการกระตุ้นของอิเล็กตรอนจากการดูดซับพลังงานแสงที่มากขึ้น จากผลการวิเคราะห์ทางสถิติพบว่า อิทธิพลหลักคือปัจจัยทั้งสามและผลของปฏิสัมพันธ์ระหว่างปัจจัย (1) และ (3) และ ปัจจัย (2) และ (3) ในการสังเคราะห์ตัวเร่งปฏิกิริยาไทเทเนียมไดออกไซด์มีผลต่อการสลายสารละลายเมทิลออเรนจ์อย่างมีนัยสำคัญทั้งในสภาวะที่ใช้แสงยูวีและวิสิเบิล

สาขาวิชา วิศวกรรมเคมี
ปีการศึกษา 2561

ลายมือชื่อนิสิต
ลายมือชื่อ อ.ที่ปรึกษาหลัก

6070319421 : MAJOR CHEMICAL ENGINEERING

KEYWORD: Photocatalytic degradation; Methyl Orange; Black titanium Dioxide;
Defect engineering; Factorial experimental design

Saran Saensook : SYNTHESIS OF BLACK TITANIUM DIOXIDE AND EFFECT OF
CALCINATION CONDITIONS AND REDUCING AGENT ON PHOTOCATALYTIC
DEGRADATION OF METHYL ORANGE. Advisor: Akawat Sirisuk, Ph.D.

This research studied the synthesis and application of black titanium dioxide in the photocatalytic degradation of methyl orange (MO). First, titanium dioxide was prepared via a sol-gel method. Then sodium borohydride was used as the reducing agent in order to synthesize black titanium dioxide. Thus, a 2x2x3 factorial experimental design was employed to assess the significance of the following three factors: (A) calcination temperature (400 and 500 °C); (B) calcination time (5 and 10 h); and (C) the molar ratio of NaBH₄ to TiO₂ used (0:1, 0.5:1, and 1:1). The removal of MO under UV and visible light were the responses for the analysis of variance. Prior to the photocatalytic experiment, the catalyst was stirred in the dark for one hour before irradiation by either UV or visible light bulbs for three hours. The concentration of MO was measured by UV-Vis spectrophotometer. The highest conversion of MO (82.17% under UV irradiation and 71.92% under visible irradiation) was obtained by black titanium dioxide that was calcined at 500 °C, 10 h, molar ratio of NaBH₄ to TiO₂ of 1:1. The catalyst contained the largest amount of surface defect, which trapped photoexcited electrons on the surface and prevent the recombination of electrons and holes. Moreover, the band gap of black TiO₂ was narrower and the light absorption in the visible region was enhanced, leading to more photogeneration of charge carriers. From statistical analysis, three main effects and their interactions between factors A and C and factors B and C in the synthesis of white and black TiO₂ catalysts were significant for both photocatalytic degradation of MO under UV and visible light.

Field of Study: Chemical Engineering Student's Signature

Academic Year: 2018 Advisor's Signature

ACKNOWLEDGEMENTS

This thesis would not have been completed without the support from the following individuals. Firstly, I appreciate valuable suggestions or guidances and supports on this research from my thesis advisor, Dr. Akawat Sirisuk of the Center of Excellence on Catalysis and Catalytic Reaction Engineering, Faculty of Engineering, Chulalongkorn University.

In addition, I would like to thank all members at Center of Excellence in Catalysis and Catalytic Reaction Engineering, who always give the assistance and encouragement along this research.

Most importantly, I would like to thanks for kindness from Department of Chemical Engineering and the Center of Excellence on Catalysis and Catalytic Reaction Engineering, Chulalongkorn University for giving me the scholarship to study here and to support me for personal expenses and doing the research.

Finally, I would like to express my gratitude to my family for their encouragements and supports throughout. This accomplishment would not occur without them.

จุฬาลงกรณ์มหาวิทยาลัย
CHULALONGKORN UNIVERSITY

Saran Saensook

TABLE OF CONTENTS

	Page
.....	iii
ABSTRACT (THAI).....	iii
.....	iv
ABSTRACT (ENGLISH).....	iv
ACKNOWLEDGEMENTS.....	v
TABLE OF CONTENTS.....	vi
LIST OF TABLES.....	x
LIST OF FIGURES.....	xv
CHAPTER 1 INTRODUCTION.....	1
1.1 Rationale.....	1
1.2 Objectives.....	4
1.3 Research scopes.....	4
1.3.1 Synthesis of black titanium dioxide.....	4
1.3.2 The characterization of the photocatalysts by several techniques.....	5
1.3.3 The photocatalytic activity testing.....	5
1.3.4 Statistical Analysis.....	6
CHAPTER 2 THEORY.....	7
2.1 Titanium dioxide.....	7
2.1.1 Physical and chemical properties.....	7
2.1.2 Applications of titanium dioxide.....	9
2.1.3 Titanium dioxide synthesis method.....	11

2.1.3.1 Sol-gel method	11
2.2 Black titanium dioxide	13
2.2.1 Properties of black titanium dioxide.....	13
2.2.2 Applications of black titanium dioxide.....	15
2.3 Photocatalytic Process	16
2.3.1 Titanium dioxide photocatalysis.....	16
2.4 An effective reducing agent: Sodium Borohydride.....	18
2.5 Azo dye	19
2.5.1 Methyl Orange	19
CHAPTER 3 LITERATURE REVIEWS	20
3.1 Effect of calcination temperature and time on properties and photocatalytic activities of titanium dioxide	20
3.2 Effect of a reducing agent on properties and photocatalytic activities of black titanium dioxide.	24
CHAPTER 4 EXPERIMENTAL.....	28
4.1 Materials.....	28
4.2 Preparation of black titanium dioxide catalysts	28
4.2.1 Preparation of titanium dioxide via sol-gel method.....	30
4.2.2 Preparation of black titanium dioxide by the chemical reduction method	30
4.3 Photocatalytic experiments	31
4.4 Physical and electrochemical characterization.....	33
4.4.1 X-ray diffraction (XRD).....	33
4.4.2 Nitrogen physisorption.....	33
4.4.3 Photoluminescence spectroscopy (PL).....	33

4.4.4 X-ray photoelectron spectroscopy (XPS).....	33
4.4.5 UV-visible reflectance spectroscopy (UV-Vis).....	34
4.4.6 Fourier transform infrared spectroscopy (FTIR)	34
4.5 Statistical analysis.....	35
CHAPTER 5 RESULTS AND DISCUSSION.....	36
5.1 Characterization of the catalysts	36
5.1.1 Phase structure analysis (XRD)	36
5.1.2 Measurement of specific surface area and pore structure	40
5.1.3 X-ray photoelectron spectra (XPS) analysis	48
5.1.4 Photoluminescence (PL) spectra analysis.....	58
5.1.5 UV-visible reflectance spectra (UV-Vis) analysis	61
5.1.6 Fourier transform infrared spectroscopy (FTIR) analysis	66
5.2 Photocatalytic activity	69
5.2.1 The photocatalytic degradation of methyl orange under UV light	70
irradiation.....	70
5.2.2 The photocatalytic degradation of methyl orange under visible light.....	81
irradiation.....	81
5.3 Statistical Analysis	91
5.3.1 The effects of catalyst preparation parameters on the removal of.....	91
methyl orange in the photocatalytic degradation under UV light irradiation....	91
5.3.2 The effects of catalyst preparation parameters on the removal of.....	100
methyl orange in the photocatalytic degradation under visible light irradiation	
.....	100
CHAPTER 6 CONCLUSIONS.....	110

6.1 Conclusions	110
6.2 Recommendations for future studies	111
REFERENCES	112
APPENDICES.....	120
APPENDIX A CALCULATION OF CATALYST PREPARATION	121
APPENDIX B CALCULATION OF THE CRYSTALLITE SIZE	122
APPENDIX C CALCULATION OF THE AMOUNT OF ANATASE, RUTILE, AND BROOKITE PHASES.....	124
APPENDIX D CALIBRATION CURVE OF METHYL ORANGE	126
APPENDIX E CALCULATION FROM XPS SPECTRA RESULTS	127
APPENDIX F CALCULATION OF THE BAND GAP FROM UV-VIS SPECTRA.....	130
APPENDIX G THE PROPERTIES OF LIGHTING INSTRUMENT	132
APPENDIX H THE MATHEMATICAL MODEL FROM STATISTICAL ANALYSIS	133
APPENDIX I GRAPHS FROM STATISTICAL ANALYSIS.....	144
VITA.....	149

LIST OF TABLES

	Page
Table 1.1 Preparation parameters for the synthesis of black TiO ₂ , used in this study.	5
Table 2.1 Properties of Titanium dioxide (TiO ₂).....	8
Table 2.2 The examples of applications in many fields of TiO ₂ nanomaterials.....	10
Table 2.3 Preparation methods and properties of black TiO ₂ nanomaterials.....	13
Table 2.4 The properties of black titanium dioxide.....	14
Table 2.5 Some applications of black TiO ₂ nanomaterials.....	15
Table 4.1 Chemicals used in the study.....	28
Table 4.2 Preparation parameters for the synthesis of black TiO ₂ , used in this study	29
Table 4.3 List of all TiO ₂ catalysts in this study.....	30
Table 5.1 All white and black TiO ₂ catalysts that were used in this study.....	38
Table 5.2 Weight fraction of anatase, rutile and brookite and crystallite size of TiO ₂ that used as starting materials for synthesis of black TiO ₂	38
Table 5.3 Specific surface area, average pore size diameter, and total pore volume of TiO ₂ and black TiO ₂ at various conditions.....	41
Table 5.4 The peak area ratios of titanium for TiO ₂ calcined at 400 °C 5 h for various amount of reducing agent from XPS results.....	50
Table 5.5 The percentage of peak area of oxygen for TiO ₂ calcined at 400 °C 5 h for various amount of reducing agent from XPS results.	51
Table 5.6 The peak area ratios of titanium for TiO ₂ calcined at 400 °C 10 h for various amount of reducing agent from XPS results.....	52
Table 5.7 The percentage of peak area of oxygen for TiO ₂ calcined at 400 °C 10 h for various amount of reducing agent from XPS results.	53

Table 5.8 The peak area ratios of titanium for TiO ₂ calcined at 500 °C 5 h for various amount of reducing agent from XPS results.....	54
Table 5.9 The percentage of peak area of oxygen for TiO ₂ calcined at 500 °C 5 h for various amount of reducing agent from XPS results..	55
Table 5.10 The peak area ratios of titanium for TiO ₂ calcined at 500 °C 10 h for various amount of reducing agent from XPS results.....	56
Table 5.11 The percentage of peak area of oxygen for TiO ₂ calcined at 500 °C 10 h for various amount of reducing agent from XPS results.	57
Table 5.12 The comparison of the band gap energy from UV-Vis absorption spectra of titanium dioxide and black titanium dioxide catalysts that synthesized at were various conditions.	65
Table 5.13 The removal of methyl orange from photocatalytic degradation and adsorption under UV light irradiation over white TiO ₂ and black TiO ₂ , which were calcined at 400 °C.	73
Table 5.14 The removal of methyl orange from photocatalytic degradation and adsorption under UV light irradiation over white TiO ₂ and black TiO ₂ , which were calcined at 500 °C.....	74
Table 5.15 The methyl orange conversion, pseudo-first order rate constant, and coefficient of determination (R ²) for photocatalytic degradation under UV light irradiation over whiteTiO ₂ and black TiO ₂ , which were calcined at 400 °C.....	77
Table 5.16 The methyl orange conversion, pseudo-first order rate constant, and coefficient of determination (R ²) for photocatalytic degradation under UV light irradiation over whiteTiO ₂ and black TiO ₂ , which were calcined at 500 °C.....	80
Table 5.17 The removal of methyl orange from photocatalytic degradation and adsorption under visible light irradiation over white TiO ₂ and black TiO ₂ calcined at 400 °C.	84

Table 5.18 The removal of methyl orange from photocatalytic degradation and adsorption under visible light irradiation over white TiO ₂ and black TiO ₂ calcined at 500 °C.....	84
Table 5.19 The methyl orange conversion, pseudo-first order rate constant, and coefficient of determination (R ²) for photocatalytic degradation under visible light irradiation over whiteTiO ₂ and black TiO ₂ , which were calcined at 400 °C.....	88
Table 5.20 The methyl orange conversion, pseudo-first order rate constant, and coefficient of determination (R ²) for photocatalytic degradation under visible light irradiation over whiteTiO ₂ and black TiO ₂ , which were calcined at 500 °C.....	90
Table 5.21 The removal of methyl orange from photocatalytic degradation under UV light irradiation over all TiO ₂ catalysts from the 2 x 2 x 3 factorial design study...	92
Table 5.22 The analysis of variance (ANOVA) of the removal of methyl orange from photocatalytic degradation and adsorption under UV light irradiation.....	93
Table 5.23 The analysis of variance (ANOVA) of the removal of methyl orange from photocatalytic degradation, excluding the adsorption under UV light irradiation..	94
Table 5.24 The model summary from the analysis of variance (ANOVA) of the removal of methyl orange from photocatalytic degradation under UV light irradiation.....	95
Table 5.25 Fits and diagnostics for all observations of the removal from photocatalytic degradation and adsorption under UV light irradiation.....	98
Table 5.26 Fits and diagnostics for all observations of the removal from photocatalytic degradation, excluding the adsorption under UV light irradiation.....	99
Table 5.27 The removal of methyl orange from photocatalytic degradation under visible light irradiation over all TiO ₂ catalysts from the 2 x 2 x 3 factorial design study.....	100

Table 5.28 The analysis of variance (ANOVA) of the removal from photocatalytic degradation and adsorption under visible light irradiation.....	102
Table 5.29 The analysis of variance (ANOVA) of the removal from photocatalytic degradation, excluding the adsorption under visible light irradiation.....	103
Table 5.30 The model summary from the analysis of variance (ANOVA) of the removal of methyl orange from photocatalytic degradation under visible light irradiation.....	104
Table 5.31 Fits and diagnostics for all observations of the removal from photocatalytic degradation and adsorption under visible light irradiation..	108
Table 5.32 Fits and diagnostics for all observations of the removal from photocatalytic degradation, excluding adsorption under visible light irradiation.....	109
Table C.1 Height of the intensity of TiO ₂ from Origin Pro 2018.....	125
Table E.1 The peak area of titanium for T400-5 from XPS.....	128
Table E.2 The peak area of oxygen for T400-5 from XPS.....	129
Table G.1 The properties of light bulbs for using in the photocatalytic degradation.....	132
Table H.1 Values of operating variables used in the 2 x 2 x 3 factorial design study.....	133
Table H.2 Estimated regression coefficients for the removal of methyl orange from the photocatalytic degradation under UV light irradiation that included adsorption of BT500-10-1 catalyst (from Table H.3).....	134
Table H.3 Estimated regression coefficients for the removal of methyl orange from the photocatalytic degradation under UV light irradiation that included adsorption.....	136

Table H.4 Estimated regression coefficients for the removal of methyl orange from the photocatalytic degradation under UV light irradiation, excluding the adsorption.....	138
Table H.5 Estimated regression coefficients for the removal of methyl orange from the photocatalytic degradation under visible light irradiation that included adsorption.....	140
Table H.6 Estimated regression coefficients for the removal of methyl orange from the photocatalytic degradation under visible light irradiation, excluding the adsorption ..	142



LIST OF FIGURES

	Page
Figure 2.1 Rutile (a), Anatase (b) and Brookite (c) phases of crystalline TiO ₂	9
Figure 2.2 Applications fields of TiO ₂ nanoparticles	9
Figure 2.3 Sol-gel method: the hydrolysis, condensation and calcination process in synthesizing the crystalline anatase, rutile, and brookite TiO ₂ nanoparticles	12
Figure 2.4 Principal photocatalytic process in the TiO ₂ nanoparticles	16
Figure 2.5 Structure of methyl orange	19
Figure 3.1 The XRD patterns of TiO ₂ nanoparticles	21
Figure 3.2 Effect of calcination temperature	21
Figure 3.3 HRTEM images of black TiO ₂ taken from (a) the {001} and (b){101} crystal faces	27
Figure 4.1 The photocatalytic reactor set for the experiments	32
Figure 5.1 XRD patterns of TiO ₂ and black TiO ₂ calcined at 400 °C for different calcination time and molar ratio of reducing agent.....	39
Figure 5.2 XRD patterns of TiO ₂ and black TiO ₂ calcined at 500 °C for different calcination time and molar ratio of reducing agent.....	39
Figure 5.3 N ₂ adsorption-desorption isotherm curves of (a) T400-5, (b) BT400-5-0.5 and (c) BT400-5-1.....	42
Figure 5.4 BJH pore size distribution plots of (a) T400-5, (b) BT400-5-0.5 and (c) BT400-5-1.....	42
Figure 5.5 N ₂ adsorption-desorption isotherm curves of (d) T400-10, (e) BT400-10-0.5 and (f) BT400-10-1	43
Figure 5.6 BJH pore size distribution plots of (d) T400-10, (e) BT400-10-0.5 and (f) BT400-10-1	43

Figure 5.7 N ₂ adsorption-desorption isotherm curves of (g) T500-5, (h) BT500-5-0.5 and (i) BT500-5-1	44
Figure 5.8 BJH pore size distribution plots of (g) T500-5, (h) BT500-5-0.5 and (i) BT500-5-1	44
Figure 5.9 N ₂ adsorption-desorption isotherm curves of (j) T500-10, (k) BT500-10-0.5 and (l) BT500-10-1	45
Figure 5.10 BJH pore size distribution plots of (j) T500-10, (k) BT500-10-0.5 and (l) BT500-10-1	45
Figure 5.11 XPS spectra; Ti 2p of (a) T400-5, (b) BT400-5-0.5 and (c) BT400-5-1	50
Figure 5.12 XPS spectra; O 1s of (a) T400-5, (b) BT400-5-0.5 and (c) BT400-5-1	51
Figure 5.13 XPS spectra; Ti 2p of (d) T400-10, (e) BT400-10-0.5 and (f) BT400-10-1	52
Figure 5.14 XPS spectra; O 1s of (d) T400-10, (e) BT400-10-0.5 and (f) BT400-10-1	53
Figure 5.15 XPS spectra; Ti 2p of (g) T500-5, (h) BT500-5-0.5 and (i) BT500-5-1	54
Figure 5.16 XPS spectra; O 1s of (g) T500-5, (h) BT500-5-0.5 and (i) BT500-5-1	55
Figure 5.17 XPS spectra; Ti 2p of (j) T500-10, (k) BT500-10-0.5 and (l) BT500-10-1	56
Figure 5.18 XPS spectra; O 1s of (j) T500-10, (k) BT500-10-0.5 and (l) BT500-10-1	57
Figure 5.19 Photoluminescence spectra of (a) T400-5, (b) BT400-5-0.5 and (c) BT400-5-1 with the excitation wavelength at 325 nm	59
Figure 5.20 Photoluminescence spectra of (d) T400-10, (e) BT400-10-0.5 and (f) BT400-10-1 with the excitation wavelength at 325 nm	59
Figure 5.21 Photoluminescence spectra of (g) T500-5, (h) BT500-5-0.5 and (i) BT500-5-1 with the excitation wavelength at 325 nm	60
Figure 5.22 Photoluminescence spectra of (j) T500-10, (k) BT500-10-0.5 and (l) BT500-10-1 with the excitation wavelength at 325 nm	60

Figure 5.23 Photoluminescence spectra of all catalysts; (a)-(l) with the excitation wavelength at 325 nm.....	61
Figure 5.24 UV-Vis absorption spectra of (a) T400-5, (b) BT400-5-0.5, (c) BT400-5-1, (d) T400-10, (e) BT400-10-0.5, (f) BT400-10-1, (g) T500-5, (h) BT500-5-0.5, (i) BT500-5-1, (j) T500-10, (k) BT500-10-0.5 and (l) BT500-10-1	62
Figure 5.25 Tauc plot of the band gap energy derived from UV-Vis absorption spectra of (a) T400-5, (b) BT400-5-0.5 and (c) BT400-5-1	63
Figure 5.26 Tauc plot of the band gap energy derived from UV-Vis absorption spectra of (d) T400-10, (e) BT400-10-0.5 and (f) BT400-10-1	63
Figure 5.27 Tauc plot of the band gap energy derived from UV-Vis absorption spectra of (g) T500-5, (h) BT500-5-0.5 and (i) BT500-5-1	64
Figure 5.28 Tauc plot of the band gap energy derived from UV-Vis absorption spectra of (j) T500-10, (k) BT500-10-0.5 and (l) BT500-10-1	64
Figure 5.29 FTIR spectra of (a) T400-5, (b) BT400-5-0.5 and (c) BT400-5-1 with the wavenumber from 4000 to 500 cm^{-1}	67
Figure 5.30 FTIR spectra of (d) T400-10, (e) BT400-10-0.5 and (f) BT400-10-1 with the wavenumber from 4000 to 500 cm^{-1}	67
Figure 5.31 FTIR spectra of (g) T500-5, (h) BT500-5-0.5 and (i) BT500-5-1 with the wavenumber from 4000 to 500 cm^{-1}	68
Figure 5.32 FTIR spectra of (j) T500-10, (k) BT500-10-0.5 and (l) BT500-10-1 with the wavenumber from 4000 to 500 cm^{-1}	68
Figure 5.33 Photocatalytic degradation of methyl orange that included adsorption results under UV irradiation over (o) No catalyst, (a) T400-5, (b) BT400-5-0.5, and (c) BT400-5-1	71

Figure 5.34 Photocatalytic degradation of methyl orange that included adsorption results under UV irradiation over (d) T400-10 , (e) BT400-10-0.5, and (f) BT400-10-1	71
Figure 5.35 Photocatalytic degradation of methyl orange that included adsorption results under UV irradiation over (g) T500-5, (h) BT500-5-0.5 and (i) BT500-5-1	72
Figure 5.36 Photocatalytic degradation of methyl orange that included adsorption results under UV irradiation over (j) T500-10, (k) BT500-10-0.5 and (l) BT500-10-1	72
Figure 5.37 Photocatalytic degradation of methyl orange results under UV irradiation over (o) No catalyst, (a) T400-5, (b) BT400-5-0.5 and (c) BT400-5-1	75
Figure 5.38 Pseudo first-order plots for the photocatalytic degradation of methyl orange under UV irradiation over (o) No catalyst, (a) T400-5, (b) BT400-5-0.5 and (c) BT400-5-1	76
Figure 5.39 Photocatalytic degradation of methyl orange results under UV irradiation over (d) T400-10, (e) BT400-10-0.5, and (f) BT400-10-1	76
Figure 5.40 Pseudo first-order plots for the photocatalytic degradation of methyl orange under UV irradiation over (d) T400-10, (e) BT400-10-0.5, and (f) BT400-10-1...	77
Figure 5.41 Photocatalytic degradation of methyl orange results under UV irradiation over (g) T500-5, (h) BT500-5-0.5, and (i) BT500-5-1	78
Figure 5.42 Pseudo first-order plots for the photocatalytic degradation of methyl orange under UV irradiation over (g) T500-5, (h) BT500-5-0.5, and (i) BT500-5-1	78
Figure 5.43 Photocatalytic degradation of methyl orange results under UV irradiation over (j) T500-10, (k) BT500-10-0.5, and (l) BT500-10-1.....	79

Figure 5.44 Pseudo first-order plots for the photocatalytic degradation of methyl orange under UV irradiation over (j) T500-10, (k) BT500-10-0.5, and (l) BT500-10-1 79

Figure 5.45 Photocatalytic degradation of methyl orange that included adsorption results under visible light irradiation over (o) No catalyst, (a) T400-5, (b) BT400-5-0.5, and (c) BT400-5-1..... 82

Figure 5.46 Photocatalytic degradation of methyl orange that included adsorption results under visible light irradiation over (d) T400-10 , (e) BT400-10-0.5, and (f) BT400-10-1 82

Figure 5.47 Photocatalytic degradation of methyl orange that included adsorption results under visible light irradiation over (g) T500-5, (h) BT500-5-0.5, and (i) BT500-5-1 83

Figure 5.48 Photocatalytic degradation of methyl orange that included adsorption results under visible light irradiation over (j) T500-10, (k) BT500-10-0.5, and (l) BT500-10-1 83

Figure 5.49 Photocatalytic degradation of methyl orange results under visible light irradiation over (o) No catalyst, (a) T400-5, (b) BT400-5-0.5, and (c) BT400-5-1 86

Figure 5.50 Pseudo first-order plots for the photocatalytic degradation of methyl orange under visible light irradiation over (o) No catalyst, (a) T400-5, (b) BT400-5-0.5, and (c) BT400-5-1..... 86

Figure 5.51 Photocatalytic degradation of methyl orange results under visible light irradiation over (d) T400-10, (e) BT400-10-0.5, and (f) BT400-10-1..... 87

Figure 5.52 Pseudo first-order plots for the photocatalytic degradation of methyl orange under visible light irradiation over (d) T400-10, (e) BT400-10-0.5, and (f) BT400-10-1 87

Figure 5.53 Photocatalytic degradation of methyl orange results under visible light irradiation over (g) T500-5, (h) BT500-5-0.5, and (i) BT500-5-1	88
Figure 5.54 Pseudo first-order plots for the photocatalytic degradation of methyl orange under visible light irradiation over (g) T500-5, (h) BT500-5-0.5, and (i) BT500-5-1	89
Figure 5.55 Photocatalytic degradation of methyl orange results under visible light Irradiation over (j) T500-10, (k) BT500-10-0.5, and (l) BT500-10-1	89
Figure 5.56 Pseudo first-order plots for the photocatalytic degradation of methyl orange under visible light irradiation over (j) T500-10, (k) BT500-10-0.5, and (l) BT500-10-1	90
Figure B.1 The diffraction peak of TiO ₂ that was calcined at 400 °C for five hours for calculation of the crystallite size.....	123
Figure D.1 The calibration curve of methyl orange from scanning by UV-Vis spectrophotometer Perkin-Elmer 650.....	126
Figure E.1 The XPS spectra for TiO ₂ nanoparticles; Ti 2p for T400-5.....	127
Figure E.2 The XPS spectra for TiO ₂ nanoparticles; O 1s for T400-5.....	129
Figure F.1 The band gap of TiO ₂	131
Figure I.1 Pareto chart of the standardized effects on the removal percentage of methyl orange under UV light irradiation that included adsorption (a); under UV light irradiation, excluding the adsorption (b); under visible light irradiation that included adsorption (c); under visible light irradiation, excluding the adsorption (d).....	144

Figure I.2 The plot of normal probability of residuals (a); residuals versus observation order (b); residuals versus fits (c); residuals versus factor A (d); residuals versus factor B (e); residuals versus factor C (f) for the removal percentage of methyl orange under UV light irradiation that included adsorption	145
Figure I.3 The plot of normal probability of residuals (a); residuals versus observation order (b); residuals versus fits (c); residuals versus factor A (d); residuals versus factor B (e); residuals versus factor C (f) for the removal percentage of methyl orange under UV light irradiation, excluding the adsorption	146
Figure I.4 The plot of normal probability of residuals (a); residuals versus observation order (b); residuals versus fits (c); residuals versus factor A (d); residuals versus factor B (e); residuals versus factor C (f) for the removal percentage of methyl orange under visible light irradiation that included adsorption	147
Figure I.5 The plot of normal probability of residuals (a); residuals versus observation order (b); residuals versus fits (c); residuals versus factor A (d); residuals versus factor B (e); residuals versus factor C (f) for the removal percentage of methyl orange under visible light irradiation, excluding the adsorption	148

CHAPTER 1

INTRODUCTION

1.1 Rationale

At present, the organic pollutants in wastewater are dangerous problems in the global chemical industries such as paper, food, leather, paints, and textiles industries. The dye is the most important chemical compound used in these chemical industries, but it is the main pollutant in the industrial wastewater due to their toxicity and carcinogenesis. Azo dyes are one of the toxic materials which are widely used in the manufacturing process of textile and other related industries. Therefore, the removal of azo dye from wastewater is crucial for solving this problem. There are several traditional ways for the wastewater treatment including physical, chemical, and biological method. Biological treatment is an eco-friendly and cost-effective method, but it is limited to laboratory scale such as microbial and enzymatic degradation. The removal of azo dyes by physical and chemical treatment has high operating cost, low efficiency, and the generation of toxic by-products. These drawbacks have to improve to be an economical and effective method [1-3]. One promising method for wastewater treatment for removal of azo dyes is semiconductor photocatalysis because of its many advantages, such as the absence of by-product, easy operation, and cleanliness.

The photocatalytic activity of titanium dioxide (TiO_2) has been studied by Fujishima and Honda [4] for a long time since the early period of the 20th century. In the first period, the investigation of the photolysis of water has been studied by using a single crystal TiO_2 semiconductor electrode because it consisted of a positive charge of valence band edge, which can oxidize water to oxygen. Later, they discovered that the photolysis of water could not proceed in the powder system, so the photocatalysis had been invented for the production of hydrogen and oxygen from water and organic compound in the powder system. There were several experiments about TiO_2 photocatalysis under UV or visible light to purify wastewater

and polluted air because its reaction efficiency and stability were much higher than those of other semiconductors. However, its application was still limited in the real industry technology at that time [5].

Titanium dioxide (TiO_2) has been commonly used as white pigment or photocatalyst for pollutant removal. It possesses many advantages due to their excellent photocatalytic properties, good long-term stability, low cost, and non-toxicity. Its drawback is the large band gap energy that allows the photocatalyst to be activated under UV irradiation only, so its application under visible light or direct solar light is limited [5-7].

A number of strategies have been made to increase the photocatalytic activity under both UV and visible light region, especially for extending the light absorption wavelength range to the visible light region and to retard the recombination of photo-excited electrons and holes. These strategies include non-metal or transition metal doping, anchoring of noble metals, surface defect engineering, and textural designing by adding the catalyst supports to the photocatalyst [6-8]. Surface defect engineering is an interesting strategy to improve photocatalytic activity of TiO_2 because it has a potential to modify the electronic and optical properties of nanomaterials for use in various photocatalytic applications [9]. An effective nanomaterial has been developed and it is called “black titanium dioxide”.

Black titanium dioxide was discovered by Chen et al. [10] since 2011 and has triggered worldwide research interests with new expectation to enhance photocatalytic activity, resulting from a defect-rich or amorphous surface layer with black color. It is capable of utilizing both UV and visible light, especially for visible light region, for photocatalytic pollution removal and hydrogen generation from water [11].

Various methods can be employ to synthesize black TiO_2 nanomaterials, including hydrogenation or hydrogen thermal treatment, hydrogen plasma treatment, chemical reduction, electrochemical reduction, and chemical oxidation. Although these different synthesis methods had given the similar appearance of black TiO_2 , their microstructures may differ due to the differences in preparation parameters.

The chemical reduction method is an effective approach of surface defect engineering to be synthesis of black TiO₂ due to it can bring about defects into semiconductors with the high temperature treatment under inert atmosphere by using different reducing agents such as sodium borohydride (NaBH₄), calcium hydride (CaH₂), hydrazine (N₂H₄), aluminum, magnesium, lithium, or even reducing solvents like ethylene glycol and glycerol [9, 11].

Sodium borohydride (NaBH₄) is a reducing reagent used in the chemical reduction method to synthesize black TiO₂ due to its high ability in reducing Ti(IV) to Ti(III), which increases the donor density or oxygen vacancies and enhances the electrical conductivity as well as charge separation between the electrons and holes. During the NaBH₄ reduction process, oxygen vacancies are introduced on the surface of TiO₂ because NaBH₄ has strong reducibility to react with the lattice oxygen atoms. Surface oxygen vacancies serve as charge carrier or surface electrons trapping sites and consequently inhibit the charge recombination and increase the photocatalytic activity of TiO₂ under visible light region as well as UV light region [9, 11-12].

In previous studies, NaBH₄ was used as the reducing agent to synthesize black TiO₂ in the difference method. In 2014, Fang et al. [13] studied the preparation of Ti³⁺ self-doped TiO₂ via treatment by the different amount of NaBH₄, which was added into the sol of TiO₂ in the first step before calcination and then was used for the photocatalytic degradation of rhodamine B under visible light irradiation. In 2017, Liu et al. [14] studied the preparation of black TiO₂ by a certain amount of NaBH₄ powder, which was mixed with anatase TiO₂ nanoparticles (commercial catalyst), then mixed powder was ground and calcined under an inert atmosphere in the different calcination temperature, resulting in the different colors of black TiO₂. However, the synthesis of black titanium dioxide by TiO₂ that was synthesized via a sol-gel method has not been done before.

In this research, we investigated the photocatalytic degradation of methyl orange in aqueous phase over titanium dioxide (white TiO₂) and black titanium dioxide (black TiO₂) catalysts that were synthesized under different conditions. First,

white TiO_2 was synthesized via a sol-gel method and then converted to black TiO_2 by chemical reduction method and using NaBH_4 as a reducing agent. The factorial experimental design was employed to study the main effects and the interaction effects of the three factors in the synthesis of black TiO_2 , including calcination temperature (factor A), calcination time (factor B), and the molar ratio of reducing agent (NaBH_4) to titanium dioxide catalyst (factor C). The conversions for photocatalytic degradation of methyl orange under both UV and visible light irradiations after 180 minutes were the response used in the statistical analysis.

1.2 Objectives

1. To synthesize black TiO_2 nanoparticles from white TiO_2 by NaBH_4 reduction process in order to improve the photocatalytic degradation of methyl orange under UV and visible light irradiations.
2. To study the main effects and the interaction effects of the three factors in the synthesis of black TiO_2 , using statistical analysis of variances.

1.3 Research scopes

1.3.1 Synthesis of black titanium dioxide

1. Prepare titanium dioxide nanoparticles by a sol-gel method.
2. Prepare black titanium dioxide nanoparticles by chemical reduction method, using sodium borohydride (NaBH_4) as a reducing agent.
3. Using a $2 \times 2 \times 3$ factorial experimental design for the synthesis of titanium dioxide and black titanium dioxide are listed in Table 1.1.

Table 1.1 Preparation parameters for the synthesis of black TiO₂, used in this study

Run	Calcination temperature (°C) (Factor A)	Calcination Time (hours) (Factor B)	Molar ratio of NaBH ₄ / TiO ₂ (Factor C)	Nomenclature
1	400	5	0:1	T400-5
2	500	5	0:1	T500-5
3	400	10	0:1	T400-10
4	500	10	0:1	T500-10
5	400	5	0.5:1	BT400-5-0.5
6	500	5	0.5:1	BT500-5-0.5
7	400	10	0.5:1	BT400-10-0.5
8	500	10	0.5:1	BT500-10-0.5
9	400	5	1:1	BT400-5-1
10	500	5	1:1	BT500-5-1
11	400	10	1:1	BT400-10-1
12	500	10	1:1	BT500-10-1

1.3.2 The characterization of the photocatalysts by several techniques.

1. X-ray diffraction (XRD)
2. Nitrogen physisorption
3. Photoluminescence spectroscopy (PL)
4. X-ray photoelectron spectroscopy (XPS)
5. UV-visible reflectance spectroscopy (UV-Vis)
6. Fourier transform infrared spectroscopy (FTIR)

1.3.3 The photocatalytic activity testing

1. The photocatalytic activity of the photocatalyst was measured for the photodegradation of methyl orange under either UV or visible light.

2. The concentration of methyl orange from photodegradation was measured by UV-visible spectrophotometer at $\lambda_{\max} = 464 \text{ nm}$.

1.3.4 Statistical Analysis

In this research, a factorial design of experiments was adopted to investigate the effects of catalyst preparation parameters on the photocatalytic degradation of methyl orange. In a 2x2x3 factorial experimental design, three factors are selected, namely, calcination temperature (factor A), calcination time (factor B), and the molar ratio of NaBH_4 to TiO_2 (factor C). These factors are varied as followed

- Two levels of factor A (400, 500 °C)
- Two levels of factor B (5, 10 h)
- Three levels of factor C (0:1, 0.5:1, and 1:1)

In this study, the significance of the three factors and their interactions was investigated. The removal percentage of methyl orange was considered as a response. Minitab Statistical Software (Minitab Release 16) was used in an analysis of the results.

This thesis arranged as follows:

Chapter 1 presented the introduction, objective, and scope of this study.

Chapter 2 presented the theory of photocatalysis including the information about TiO_2 and black TiO_2 catalysts and principles of photocatalytic process.

Chapter 3 presented the literature reviews of previous works related to this research.

Chapter 4 presented the synthesis of TiO_2 and black TiO_2 , the photocatalytic testing, and characterization techniques for this study.

Chapter 5 presented the characterization and experimental results and discussion.

Chapter 6 presented conclusions and recommendations for future works.

CHAPTER 2

THEORY

2.1 Titanium dioxide

Titanium dioxide (TiO_2) or titania is well-researched material since its physical, chemical, optical, and electrical properties have the stability as well as its non-toxicity, low cost, and can also use in a commercial way such as pigments, paints, coatings and the UV absorbers in sunscreens and cosmetics [15-16]. TiO_2 belongs to the family of transition metal oxides, have been widely studied in many fields including catalysis, photocatalysis, a superhydrophilic and antibacterial agent, and nano-paint in the civil. A lot of efforts have been to the study of TiO_2 nanomaterial produced many promising applications in the various area which range from photovoltaics and photocatalysis to photo-electrochromic and various sensors. These applications can generally be categorized into “energy” and “environmental” types, many of types depending on the properties of the TiO_2 material, the modification of the TiO_2 material host (e.g. ,with inorganic and organic dyes), and also on the interactions with the environment. In the past decades, the exponential growth of research activities has been seen in nanotechnology and nanoscience. When the size of nanomaterial reduced smaller down to nanometer scale, new physical and chemical properties come out [17].

2.1.1 Physical and chemical properties

In recent year, TiO_2 nanomaterials have been applied in the photocatalytic activity due to its interest in general properties, but its physical and chemical properties depend on the crystalline phase, size, and shape of particles. TiO_2 nanomaterials exist in three different polymorphs or phases: anatase, rutile, and brookite, respectively shown in Figures 2.1 (a, b, and c) [17-18].

Various phases of crystalline TiO_2 have a different bandgap that anatase TiO_2 of 3.2 eV, and rutile TiO_2 of 3.0 eV. These can determine the photocatalytic activity of TiO_2 due to it could be varied the charge transport

behaviors of electrons and holes. Anatase phase has a crystalline structure that corresponds to the tetragonal system, which is used mainly as a photocatalyst under UV irradiation and is also great interest especially for its key role in the transport of electrons in photovoltaic devices. Rutile phase also has a tetragonal structure and is mainly used as white pigment in the paint due to it has the lowest free energy and it is the most common natural form of TiO_2 . Brookite phase has an orthorhombic crystalline structure, which is not easily obtained synthetically and is also the rarest form of the natural. The transformation of anatase and brookite phases which are metastable polymorphs can occur a range of temperatures of 673-1473 K to transform exothermally and irreversibly into rutile phase depending on several factors such as the size of the particles, the presence of impurities, and whether the oxide is supported over another material. Rutile phase has the highest refractive index, and is the densest phase, while anatase is characterized by the widest bandgap. The properties of brookite fall between those of rutile and anatase as seen in Table 2.1 These properties make TiO_2 preferable for environmental applications [17-19].

Table 2.1 Properties of Titanium dioxide (TiO_2)

Properties of Titanium dioxide (TiO_2)	
Molecular Weight	79.866 g/mol
Density	3.77 g/cm ³ (Anatase) 4.11 g/cm ³ (Brookite) 4.24 g/cm ³ (Rutile)
Melting Point	1844 °C
Boiling Point	2973 °C
Refractive index (nD)	2.489 (Anatase) 2.584 (Brookite) 2.608 (Rutile)
Appearance	White solid
Solubility	Insoluble in water
Odor	Odorless

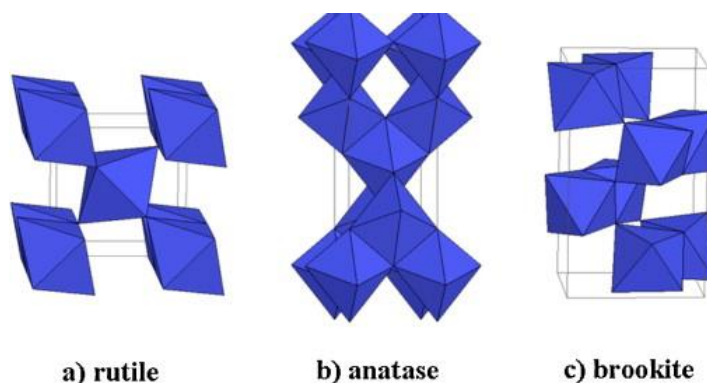


Figure 2.1 Rutile (a), Anatase (b) and Brookite (c) phases of crystalline TiO_2 [18]

2.1.2 Applications of titanium dioxide.

There are many applications of TiO_2 nanomaterials in the world, especially in the areas of new energy resources, environmental conservation, and other applications as seen in Table 2.2.

TiO_2 nanomaterials have been synthesized for use in many fields of applications due to the perfect properties included applications for water purification, air purification, decontamination, antibacterial, UV protection, sensing and paint, and photocatalysis, so they are important in our daily life.

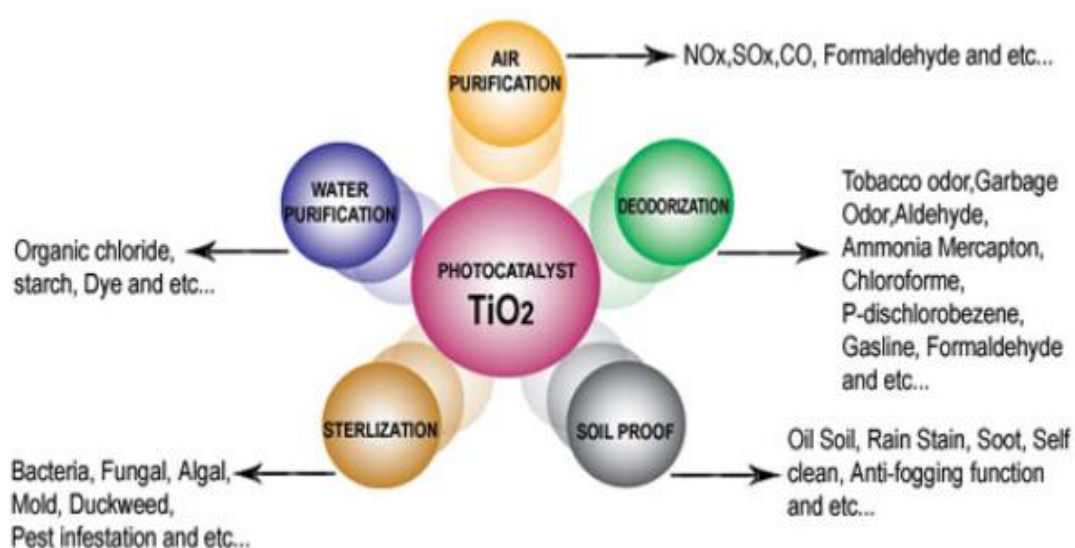


Figure 2.2 Applications fields of TiO_2 nanoparticles [17]

Table 2.2 The examples of applications in many fields of TiO₂ nanomaterials [21]

Applications	Process	Photocatalysts	Details
The environment	Degradation of Aqueous Pollutants	TiO ₂	TiO ₂ has facilitated many pollutant degradation processes such as the degradation of acid fushsin, the reduction of nitrate, the decomposition of acetaldehyde, and the dechlorination of CCl ₄ .
	Degradation of Air Pollutants	TiO ₂ /rGO TiO ₂ (P25)/N-doped carbon quantum dots	Studies on reducing the toxic Cr ⁶⁺ (hexavalent chromium) ion toxicity. It was first used as the photooxidation catalyst of NO under the irradiation of ultraviolet and visible light.
	Photocatalytic Hydrogen Generation	Oxidized graphitic C ₃ N ₄ /TiO ₂	It markedly increased the visible light photocatalytic activity for H ₂ evolution
The energy	Photocatalytic CO ₂ Reduction into Energy Fuels	Cu-doped TiO ₂	The photocatalytic performance of TiO ₂ in CO ₂ reduction process was enhanced by Cu doping on TiO ₂ .
	Solar Batteries	Ti@TiO ₂ nanowire array wire	It could be used as a photoanode in dye-sensitized solar cells; this configuration improved a conversion efficiency maintenance rate.
	Supercapacitors	Blue titanium oxide (B-TiO ₂)	It indicated excellent cycling stability with high capacitance retention.
Other applications	Antibacterial and Wound Healing	A TiO ₂ /Ag ₂ O hetero-structure	It can destroy all chemical contaminants but also kill microorganisms.
	Drug delivery carriers	H ₂ O ₂ -treated TiO ₂ nanoparticles	It acts as potential agents for enhancing the effects of radiation in the treatment of pancreatic cancer.

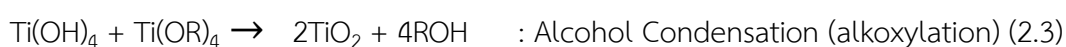
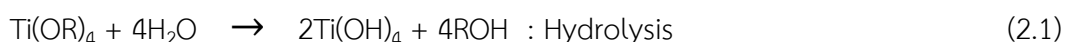
2.1.3 Titanium dioxide synthesis method

There are many techniques that can be used to synthesize TiO₂ nanomaterials, such as sol-gel method, chemical vapor deposition, liquid phase deposition, reactive sputtering, solvothermal process, reverse micelle method, electrochemical method, and hydrothermal treatment. The different method can give different surface properties such as surface area, pore volume, pore size, particle size, and also has different characteristics of phase and morphology [22].

2.1.3.1 Sol-gel method

The sol-gel method is one of the most widely used for the synthesis of TiO₂ nanomaterials, due to low processing temperature, high homogeneity, and stability of processing. Sol-gel method has been investigated for the optimal preparation conditions, such as the amount of solvent and water, the reflux temperature, the reflux time, pH, calcination temperatures because these conditions will affect the surface structure, crystalline phase, particle size, and photocatalytic activity of TiO₂ [22].

The sol-gel method is the process of transforming sol into gel. Sols are solid particles suspended in liquid, while gels are particulate networks of sols. The steps of the sol-gel method consist of two main reactions: hydrolysis and condensation before the calcination to obtain TiO₂ crystalline structure. For the synthesis of TiO₂ nanomaterials uses various precursors, including TiCl₃, Ti(OBu)₄, TiCl₄, TiBr₄, and Ti[OCH(CH₃)₂]₄ (TTIP). These precursors are then hydrolyzed by adding water, resulting in the formation of a complex in the step of condensation to obtain a three-dimensional network complex as shown in the following equations [23]:



Where **R** in the equation represents alkyl group, such as ethyl, i-propyl, n-butyl and so on.

The titanium precursor is often diluted before adding water so as to reduce the rapid reaction rate of the hydrolysis reaction. The precursor and water ratio can determine the size and morphology of TiO_2 nanomaterials. Higher ratio of water to precursor results in the formation and the aggregation of unstable colloidal and particles. For a lower ratio of water to precursor results in the monodisperse particle of 0.5-1 μm in diameter. Higher pH of solution contributes to an increased particle size of TiO_2 . The calcination process can determine the phase transformation, which is highly influenced by calcination temperature and time. The final structure of crystalline TiO_2 has three polymorphs as seen in Figure 2.3.

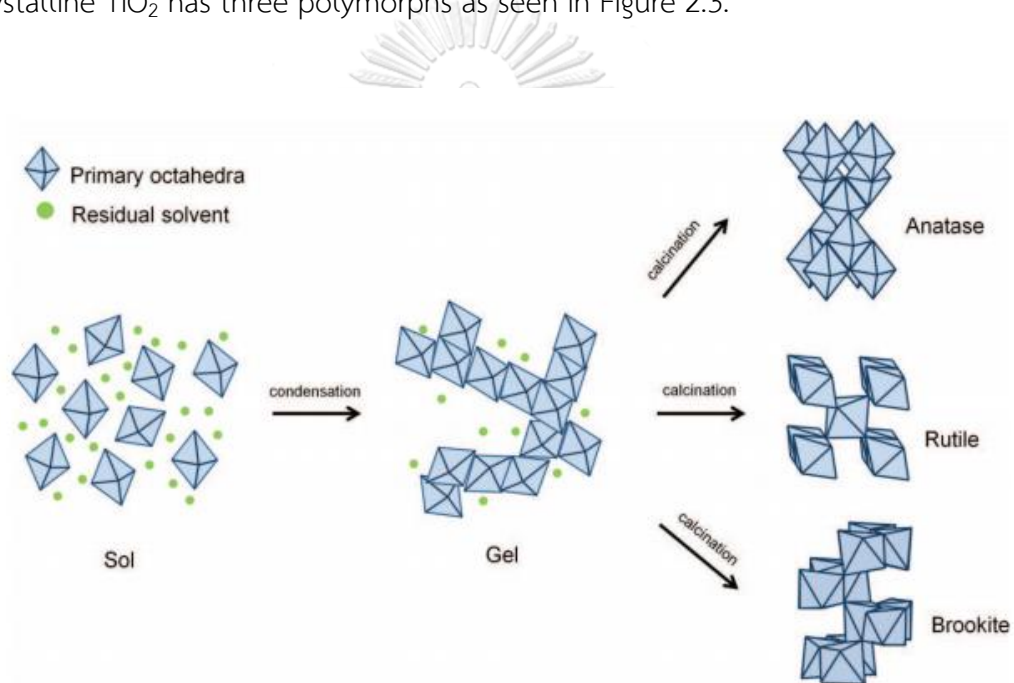


Figure 2.3 Sol-gel method: the hydrolysis, condensation and calcination process in synthesizing the crystalline anatase, rutile, and brookite TiO_2 nanoparticles [23]

2.2 Black titanium dioxide

Black titanium dioxide (TiO₂) nanomaterials were discovered in 2011 by Chen et al. [10]. It was the titanium dioxide (TiO₂) that underwent surface defect engineering to improve the optical light absorption and charge separation, thereby enhancing the photocatalytic activity of TiO₂. Black TiO₂ could possess a bandgap as narrow as 1.5 eV and a substantial solar-driven photocatalytic activity.

2.2.1 Properties of black titanium dioxide

The properties of black TiO₂ varied depending on the preparation method (as seen in Table 2.3) and the types of properties were reviewed in Table 2.4.

Table 2.3 Preparation methods and properties of black TiO₂ nanomaterials

Preparation method		Color	Properties
Chemical route	Hydrogenation	Black, blue to gray	core-shell structure, valence band shift, oxygen vacancies, Ti ³⁺ , Ti-H and Ti-OH group
	Chemical reduction (Mg, Al, NaBH ₄ , NaH)	Black, blue, dark gray, brown	core-shell structure, valence band shift, oxygen vacancies, Ti ³⁺ , Ti-H and Ti-OH group
	Chemical Oxidation	Black, blue to brown	valence band shift, oxygen vacancies, Ti ³⁺
Electrochemical	Electrochemical reduction	Black, blue	valence band shift, oxygen vacancies, Ti ³⁺
	Anodization annealing	Black	oxygen vacancies, Ti ³⁺
Physical	Ultra-sonication	Various degrees of blackness	amorphous, valence band shift, oxygen vacancies, Ti ³⁺ , Ti-H and Ti-OH group
	Laser modification	Black, gray	valence band shift, oxygen vacancies, Ti ³⁺ , surface disorder, Ti-H and Ti-OH

Table 2.4 The properties of black titanium dioxide [24-25]

Properties	Features	Research summaries
Structural	Disordered surface	<ul style="list-style-type: none"> ■ The surface of black TiO₂ has a disordered layer which obtained during the hydrogenation of TiO₂ under high pressure H₂ atmosphere. ■ The characteristic of a disordered surface shell is on all sides of a crystalline core in the black TiO₂. ■ A 2 nm disordered surface layer thickness was plated on a crystalline core. ■ Black TiO₂ nanoparticles were found to have a crystalline core- amorphous shell structure, which prepared by Al reduction, and H₂ plasma. ■ Black TiO₂ nanoparticles were found to have a thin disordered shell surrounding a nanocrystalline core, which obtained by pulsed laser vaporization method.
Chemical	Ti ³⁺ ions and Oxygen Vacancies	<ul style="list-style-type: none"> ■ The formation of oxygen vacancies and Ti⁴⁺ reduction to Ti³⁺ are sometime observed after hydrogen plasma treatment, pressurized hydrogenation, chemical reduction, chemical oxidation, and electrochemical reduction. ■ The treated temperature increased the oxygen vacancy in the hydrogenated TiO₂.
	Ti-H and Ti-OH Groups	<ul style="list-style-type: none"> ■ The content of Ti-H and Ti-OH groups appeared in hydrogenated black TiO₂, which changed after different hydrogenation treatment. ■ The intensity of the OH vibration mode band showed in the FTIR spectra was different after the hydrogenation treatment.
Optical	The optical absorption	<ul style="list-style-type: none"> ■ Black TiO₂ has long wavelength absorption from UV light region to visible and infrared region, indicating its same optical performance.
Electronic	Valence band edge	<ul style="list-style-type: none"> ■ Pure TiO₂ nanoparticles and hydrogenated TiO₂ had similar valence band shift, which was hardly influenced by the hydrogen treatment.

2.2.2 Applications of black titanium dioxide

There are many applications of black TiO₂ nanomaterials in the areas of photocatalysis, lithium-ion battery, supercapacitor, fuel cell, field emission, microwave absorption, cancer photothermal therapy, etc. (as seen in Table 2.5).

Table 2.5 Some applications of black TiO₂ nanomaterials [24]

Field	Photocatalysts	Examples of results in applications
Photocatalysis	Hydrogenated TiO ₂ nanobelts.	-There are excellent photocatalytic activities in the decomposition of methyl orange and water splitting for hydrogen production under visible light.
Lithium-ion battery	Black TiO ₂ nanocrystals	-There is excellent rate performance of lithium storage since the well-balanced Li ⁺ /e ⁻ diffusion.
Supercapacitor	Hydrogenated TiO ₂ nanotube arrays	- The excellent capacitive properties were attributed to increased density of hydroxyl group and enhanced carrier density.
Fuel cell	Hydrogenated TiO ₂ nanotube arrays combined with Sn/Pd/Pt	- When used it as the cathode in a fuel cell , exhibited excellent electrocatalytic activity , high durability and high power.
Field emission	Hydrogenated TiO ₂ nanotube arrays	- The good field emission performance was attributed to decreased work function and increased conductivity.
Microwave absorption	Black TiO ₂ nanoparticles	- It enhanced the properties of microwave absorption.
Cancer photothermal therapy	Hydrogenated black TiO ₂ nanoparticles coated with polyethylene glycol	- Photothermal conversion efficiency was obtained with a high anticancer effect and a low toxicity in vivo and in vitro.

2.3 Photocatalytic Process

Photocatalytic process or Photocatalysis is the reaction when the catalyst is activated by light or called a photoinduced reaction which composed of the photochemistry and catalysis with both light and a catalyst being desired to precipitate a chemical conversion. The photocatalytic process starts with the absorption of a photon with sufficient energy that can excite an electron to jump from the valence band to the conduction band and leave behind a hole in the valence band (as seen in Figure 2.4). As a result, electrons and holes are separated. The photocatalytic performance is affected by several parameters such as light intensity, wavelength, pH, mass/concentration, temperature, the nature of a photocatalyst, particle size, surface area, the adsorption nature, and concentration of the substrate [17, 19].

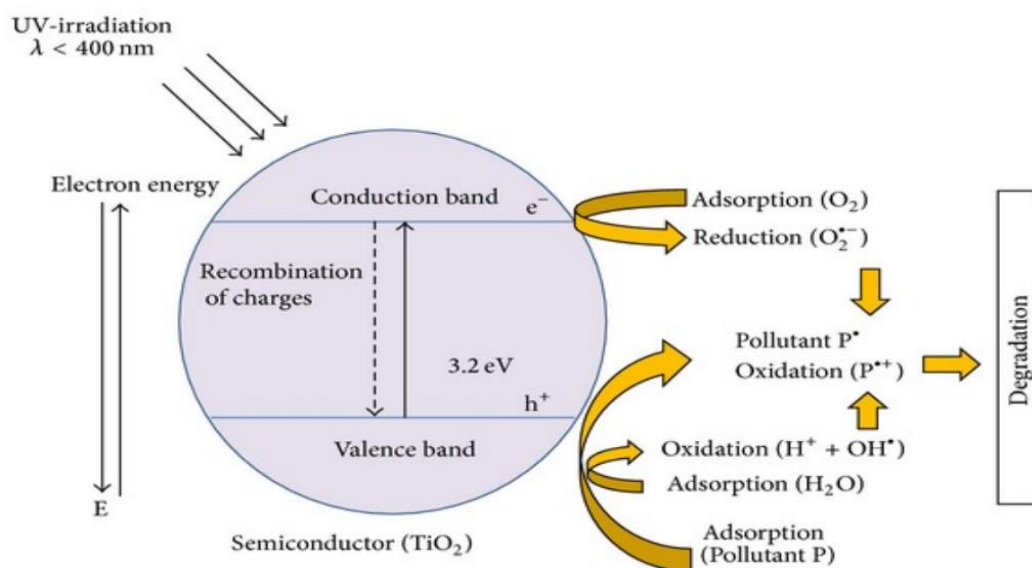


Figure 2.4 Principal photocatalytic process in the TiO_2 nanoparticles [17]

2.3.1 Titanium dioxide photocatalysis

The possible application for TiO_2 as a photocatalyst in a commercial scale water treatment facility is due to several factors [19]:

(a) Photocatalytic reactions do not encounter the disadvantage of

photolysis reactions in terms of the production of intermediate products because organic pollutants are usually completely mineralized to non-toxic substances such as CO₂, HCl, and water.

(b) A photocatalytic reaction takes place at room temperature.

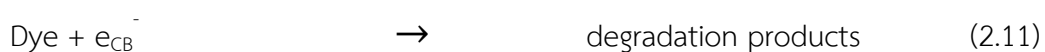
(c) Photoinduced electrons reduce sufficiently and photo-induced holes are extremely oxidizing to produce superoxides from dioxygen.

(d) The photocatalyst is inexpensive and can be supported on various substrates, such as fibers, glass, stainless steel, inorganic materials, sand, and activated carbons, and allow for continuous re-use.

For a photocatalyzed reaction, the prevention of the recombination of electrons and holes can improve photocatalytic activity since recombination is reaction competing with electron-acceptor and hole-donor, which can occur either in the bulk or at the surface of the semiconductor resulting in the release of heat and causes the reduction in the photocatalytic activity.

In this process, the UV light source used as the photon energy ($h\nu \geq E_g$), then the charge carrier or electron-hole pairs are generated.

The relevant reactions at the surface of TiO₂ photocatalyst causing the degradation of dyes can be expressed as follows [19]:



Where $h\nu$ is photon energy required to excite the semiconductor electron from the valence band (VB) region to conduction band (CB) region.

2.4 An effective reducing agent: Sodium Borohydride

Sodium borohydride (NaBH_4), or called sodium tetrahydroborate, is widely used as a reducing agent in laboratory and industrial applications. It has many advantages, including use in the catalytic hydrolysis due to its high potential to be used as hydrogen storage material for mobile application [26] or as a synthetic fuel for a direct borohydride fuel cell. Also, hydrogen storage material required good properties including fast sorption kinetics and convenient working temperatures and working pressures. There are many types of metal hydrides, e.g., LiBH_4 , $\text{Mg}(\text{BH}_4)_2$, and $\text{Ca}(\text{BH}_4)_2$, have been hindered by their high stability thus the desorption temperatures well above room temperature. The desorption temperature for metal hydride is the temperature at which hydrogen is released from a compound, depending on the experimental conditions. Desorption temperature of NaBH_4 was reported from the literature in the range from 400 to 595 °C [27].

Sodium borohydride (NaBH_4) was employed as a reducing agent to synthesize black TiO_2 via a chemical reduction method [14, 37-40]. The role of this reducing agent is to provide active hydrogen that created defects or oxygen vacancies in the nanomaterials.

2.5 Azo dye

Azo dyes are the most widely used industrial dyes in the paper, leather, cosmetics, pharmaceutical, and textile industries. Generally, an azo dye is an aromatic compound with one or more azo groups (-N=N-), nitrogen to nitrogen double bonds. This azo group has a stable molecular structure, which provides improved color fastness and resulting in strong resistance to degradation. Hence, the release of wastewater that contained azo dyes is dangerous for the aquatic life due to its toxicity. Therefore, degradation technology is crucial for solving this problem [28].

2.5.1 Methyl Orange

Methyl Orange (MO) is an azo dye used in the textile industries, especially in the study of textile wastewater decoloration and the degradation of contaminant [28]. This type of azo dye is a heterocyclic aromatic compound with chemical structure formula of $C_{14}H_{14}N_3NaO_3S$ (see Figure 2.5). Its IUPAC name is 4-[4-Dimethyl-amino)phenylazo] benzene sulfonic acid sodium salt and the molecular weight is 327.33 g/mol [29].

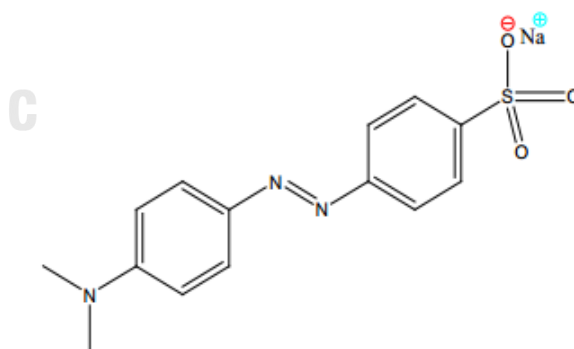


Figure 2.5 Structure of methyl orange [30]

CHAPTER 3

LITERATURE REVIEWS

This chapter contains literature reviews involving titanium dioxide and black titanium dioxide as the photocatalysts. This section discusses the effects of calcination temperature, calcination time, and a reducing agent on the photocatalytic purification of water or other reactions.

3.1 Effect of calcination temperature and time on properties and photocatalytic activities of titanium dioxide

Carrera et al. [31] studied the effect of the phase composition and crystallite size of sol-gel TiO₂ nanoparticles on the acetaldehyde photodecomposition. TiO₂ nanoparticles were prepared by a sol-gel method with different types of alcohol, including 2-propanol (P) or ethanol (E), and then were calcined at 200 and 500 °C for 3 h. Specific surface area of the samples calcined at 200 °C was three times higher than those calcined at 500 °C. Their average pore diameter and crystallite size were smaller, but pore volume was larger. This indicates the change in the pore structure when the calcination temperature was increased due to the sintering or phase transformation of the sol-gel TiO₂ nanoparticles. The nanoparticles calcined at 200°C showed higher efficiency in the acetaldehyde photodecomposition under 365-UV light because these nanoparticles had greater number of active sites. So the surface charge carrier transfer rate was enhanced in the photocatalytic reaction.

Guanyu et al. [32] studied the preparation of TiO₂ nanoparticles by a sol-gel method and photocatalytic properties on the degradation of phenol under UV light with a high pressure mercury lamp. TiO₂ nanoparticles were prepared by a sol-gel method with various amounts of distilled water and absolute ethyl alcohol and calcination temperatures. The optimum amount of distilled water and absolute ethyl

alcohol was 5 mL and 90 mL, respectively. The prepared TiO_2 was calcined at 300 °C, 400 °C, 500 °C, 525 °C, 550 °C, 575 °C, and 600 °C for 4 h, after grinding. When the temperature reached 500 °C, the anatase phase was present. A small amount of rutile phase appeared at 575 °C and became the major phase at 600 °C (see Figure 3.1). The catalyst with the most rutile phase had a low photocatalytic activity due to the disappearance of activity. The highest photocatalytic activity of phenol degradation was observed with TiO_2 that was calcined at 575 °C (see Figure 3.2).

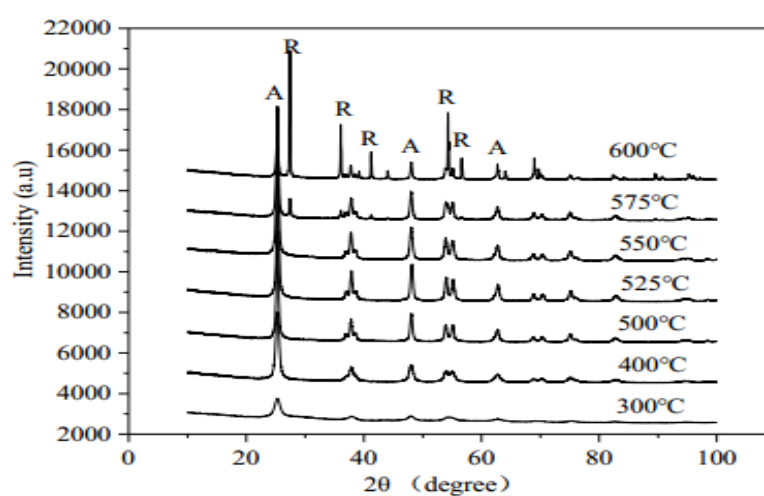


Figure 3.1 The XRD patterns of TiO_2 nanoparticles [32]

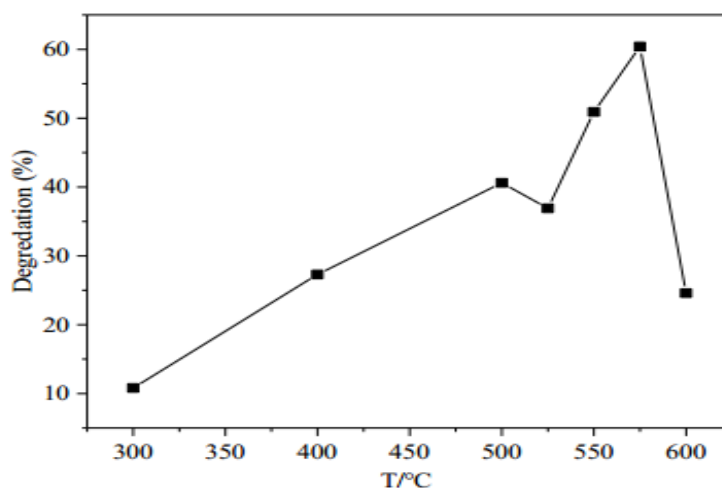


Figure 3.2 Effect of calcination temperature [32]

Hongmin et al. [33] studied the effect of TiO₂ calcination temperature on the photocatalytic oxidation of gaseous ammonia (NH₃) under UV and visible light. TiO₂ nanoparticles were prepared by a sol-gel method and were calcined in air at various temperatures (150°C, 200°C, 300°C, 400°C, 500°C, and 600°C) for 5 h. The catalysts were denoted as T₁₅₀, T₂₀₀, T₂₅₀, T₃₀₀, T₄₀₀, T₅₀₀, and T₆₀₀, respectively. From UV-absorption spectra, the samples that were calcined at 300 to 600 °C absorbed some light in the visible region ($\lambda > 400$ nm). The T₄₀₀ possessed the highest bandgap energy of 3.14 eV, similar to the commercial P25 catalyst (3.19 eV). The photoluminescence (PL) spectra were measured in the wavelength of 350-600 nm to investigate the efficiency of charge carrier trapping, transferring, and the separation of the photo-generated electron-hole pairs. The sequence of the PL intensities was in the order of P25 > T₆₀₀ > T₅₀₀ > T₄₀₀ > T₃₀₀ > T₁₅₀ > T₂₀₀. The samples calcined at lower calcination temperature had very high specific surface area (SSA), good crystallinity, and also low PL intensity, indicating the slow recombination rate of the photo-induced electron and holes. Nonetheless, they played no determining role in the photocatalytic oxidation of NH₃. The T₂₀₀ photocatalyst had low PL intensity and high SSA, but had few acid sites for NH₃ activation and adsorption. Meanwhile, T₄₀₀ had high PL intensity, moderate SSA, and the widest band gap, but it possessed the highest number of acid sites, so the T₄₀₀ catalyst demonstrated the highest photocatalytic activity of NH₃ removal under UV light.

Ashish et al. [34] studied the photocatalytic degradation of organic dye based on anatase and rutile TiO₂ nanoparticles which were prepared by modified sol-gel method. The process involved 2-propanol, and myristic acid, potato starch, or PVP as surfactant. Then the sample were calcined at 100 °C, 200 °C, 400 °C, and 800 °C for 2 h at a constant heating rate. The photocatalytic degradations of organic dyes, including methylene blue (MB), methyl orange (MO), rhodamine B (RB), indigo carmine (IC) and eriochrome black T (EBT) dye were studied under short and long UV irradiations. Anatase TiO₂ nanoparticles that were calcined at 400 °C retained a smaller size as compared with the rutile TiO₂. The XPS analysis of the catalysts to investigate the surface properties, indicated the higher calcination temperature

weakened the Ti-O-Ti bond and reduced the number of the oxygen vacancies or defects on the surface of anatase TiO₂. At about 800 °C no oxygen vacancies on the surface of rutile TiO₂ was observed. The photocatalytic degradation efficiency of various organic dyes from anatase TiO₂ was greater than that from rutile TiO₂ under short UV light irradiation.

Assia et al. [35] studied the synthesis, structural characterization, and photocatalytic activity of TiO₂ nanoparticles. The catalysts were prepared by a sol-gel method with titanium isopropoxide (TTIP), acetic acid, and anhydrous ethanol. The samples were then calcined at 500 °C for 5 and 10 h in order to investigate the effect of calcination time on the degradation of methylene blue. The XRD results showed that TiO₂ that was calcined at 500 °C consisted of the anatase phase and the particle or grain size increased with an increase in calcination time, but no change of the phase was observed. The results of the degradation of methylene blue had a higher photoreactivity of anatase phase compared to rutile or brookite phases.

Karpars et al. [36] studied the optical, photocatalytic, and structural properties of TiO₂-SiO₂ sol-gel coatings on high content SiO₂ enamel surface. The TiO₂-SiO₂ optical films were calcined at different times from 1 h and 10 h to investigate the effect of calcination time on the structural properties. The TiO₂-SiO₂ coatings that were calcined at 1 h have lower average roughness and smaller particles, compared with the coatings calcined at 10 h. When the calcination time increased, the crystal grew longer and light transmission decreased. From the photocatalytic experiment, the coating calcined for 1 h degraded 89.7% of methylene blue solution in 6 h, while the coating calcined for 10 h degraded 74.4% of methylene blue. This is attributed to the smaller grain size, and larger specific surface area. So the photocatalytic activity increased with decreasing the calcination time.

3.2 Effect of a reducing agent on properties and photocatalytic activities of black titanium dioxide.

Xinghang et al. [14] studied the synthesis of a black titania/graphene oxide nanocomposite films with excellent photothermal property for solar steam generation. A facile NaBH_4 -assisted method was used to synthesize black titania nanoparticles, which calcined at 400, 450, 500, 550, and 600 °C under an argon atmosphere for 4 h. Black titania nanoparticles with different colors were obtained from NaBH_4 reduction of anatase TiO_2 powder (molar ratio between TiO_2 : NaBH_4 is 1:1). From XRD results, the colored titania that calcined at a different temperature contained both anatase and brookite phases. When the calcination temperature increased, the diffraction peak became gradually smaller due to the effective reduction by NaBH_4 . This can be attributed to the formation of amorphous phase after the reduction process. From UV-vis spectra, the black titania that was reduced at 500 °C absorbed the longest amount of visible light. This is mainly due to the effective reduction process, which reduced Ti^{4+} to Ti^{3+} by introducing oxygen vacancies.

Huaqiao et al. [37] prepared colored TiO_2 nanoparticles with an enhanced solar-driven photocatalytic activity of methyl orange degradation and H_2 production from water under UV and visible light irradiations. The colored TiO_2 was prepared by a chemical reduction method, using P25 (Degussa) as a starting material with NaBH_4 as reductant. The product was then heated from room temperature to 300-400 °C for 5-60 minutes under an argon atmosphere. Controlling the reaction temperature and reaction time could change the color of TiO_2 from light blue to black. The black TiO_2 was produced by calcination at 350 °C for 60 minutes. From UV-vis spectra, the light absorption was better with increases in the reaction time and temperature. After the chemical reduction treatment, the concentration of oxygen vacancy increased and the crystalline lattice deformed. Oxygen vacancy was an electron donor site and could improve charge transport in TiO_2 . However, there were too many oxygen

vacancies, it could cause the photocatalytic activity would be negatively impacted. The best photocatalyst for the decomposition of methyl orange and H_2 production under UV and visible light irradiations was the one calcined at 300 °C for 50 minutes, which was more effective than P25 under the same experimental conditions.

Dessy et al. [38] studied the defect site enhancement relating to its photocatalytic activity performance of rhodamine B (RhB) by $NaBH_4$ -modified TiO_2 under solar light irradiation. $NaBH_4$ -assisted heat treatment was applied during the synthesis of defected TiO_2 nanopowders using a commercial fine anatase TiO_2 powder. The powder was then heated in the furnace to 300-450 °C for 1 h under an argon atmosphere. All catalysts contained the same anatase phase. When the temperature was increased during the heating process, the XRD peaks became smaller because the decomposition of $NaBH_4$ released the active hydrogen that attacked the crystal surface of TiO_2 , resulting the deformation of crystalline lattice and the creation of oxygen vacancies. The sample became black when treated at 400 or 450 °C. All modified TiO_2 were able to absorb light in the visible region while pristine TiO_2 has no absorption. PL analysis was conducted to study the behavior of light-generated electrons and holes in the photocatalysts. Gray TiO_2 (X300 and X350) exhibited similar peak intensities as pristine TiO_2 , while peak intensities of black TiO_2 (X400 and X450) were lowered. This suggested that black TiO_2 contained more defects than gray TiO_2 did. From XPS results, black TiO_2 contained a greater number of oxygen vacancies and larger defects because the defects formed on the surface. Meanwhile gray TiO_2 have possessed single vacancies and smaller defects, which were a bulk defect. These defects acted as the charge carrier traps and prevented the recombination of electrons and holes. From the photocatalytic activity of RhB degradation under visible light irradiation, gray TiO_2 samples (X300 and X350) completely decomposed RhB within 50 min because there were only the bulk defects that slowed down charge recombination. On the other hand black TiO_2 contained fewer surface defects than bulk defects and oxygen vacancies, resulting in a lower photocatalytic activity.

Miao et al. [39] prepared the reduced TiO₂ with tunable oxygen vacancies for catalytic oxidation of formaldehyde at room temperature. The reduced TiO₂ was prepared by a chemical reduction method using NaBH₄ as reducing agent and the commercial Degussa P25 as the precursor. Then TiO₂ was heated at 300 °C under N₂ atmosphere for the reduction time of 5, 15, 30, and 60 minutes. From XRD patterns, no additional peak of crystalline phase beside the original peaks corresponded to anatase and rutile was detected after the reduction process. However, the XRD peaks became smaller and broader with the longer reduction time, leading to the peak shifts and smaller particle size. BET surface area of the samples was in the range from 51.7 to 58.9 m² g⁻¹. The maximum value was obtained at the reduction time of 30 min, while the surface area declined to 54.0 m² g⁻¹ when the reduction time increased to 60 min as a result of the elimination of internal hydroxyls and pore collapse during the reduction treatment. UV-vis spectra indicated that the absorption of visible light (400-800 nm) with the longer reduction time. XPS spectra provided the characteristic peak assigned to Ti⁴⁺ bond and identified three types of surface oxygen species, including the lattice oxygen species, the surface adsorbed oxygen species, and the chemically-bonded water of reduced TiO₂. The fraction of lattice oxygen species decreased as the fraction of surface adsorbed oxygen species increased, thereby indicating the abundance of surface oxygen vacancies with an increase in the reduction time. The formaldehyde conversion of P25 was 51% after 20 min, while the reduced TiO₂ degraded about 94% of formaldehyde over the reduced TiO₂ at reduction time of 30 min; R-TiO₂-30 as a result of the oxygen vacancies generated on the surface of reduced TiO₂.

Xiuming et al. [40] studied the highly active black titanium dioxide/N-doped graphene quantum dots nanocomposites for sunlight-driven photocatalytic degradation of Rhodamine (RhB) dye. Black TiO₂ was prepared from anatase TiO₂ nanoparticles via NaBH₄ reduction treatment. The powder was heated at 400 °C for 12 h under an argon atmosphere. The HRTEM image of black TiO₂ nanoparticles (as seen in Figure 3.3) confirmed that the nanoparticles consisted of the crystalline core and a thin amorphous shell. The UV-visible absorption spectra indicated that black

TiO₂ had the narrower bandgap than the P25 TiO₂ (2.41 eV and 3.45 eV, respectively). The enhancement in the light absorption was consistent with the color change. The PL intensity of black TiO₂ was lower than that of P25 TiO₂ due to a slower recombination rate of electrons and holes and more efficient electron separation on the surface sites, so the photocatalytic degradation performance was improved.

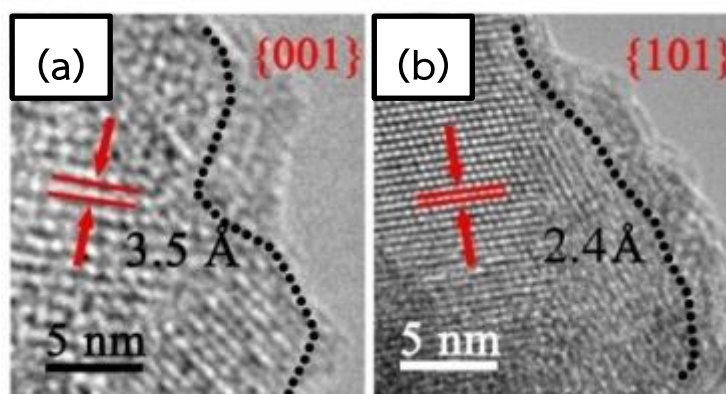


Figure 3.3 HRTEM images of black TiO₂ taken from (a) the {001} and (b) {101} crystal faces [40]

CHAPTER 4

EXPERIMENTAL

This chapter explains various preparations of black titanium dioxide, according to factorial experimental design. The photocatalytic experiments and physical and electrochemical characterization of catalysts are also described in this chapter.

4.1 Materials

The chemical used in the preparation of the catalyst and the catalytic experiments are listed in Table 4.1.

Table 4.1 Chemicals used in the study

Chemicals	Formulas	Suppliers
Titanium tetraisopropoxide ;TTIP, 97%	$Ti[OCH(CH_3)_2]_4$	Sigma-Aldrich Inc.
Nitric acid, 70%	HNO_3	Sigma-Aldrich Inc.
Sodium borohydride, 99%	$NaBH_4$	Sigma-Aldrich Inc.
Ethanol, 99.5%	C_2H_6O	Sigma-Aldrich Inc.
Methyl Orange	$C_{14}H_{14}N_3NaO_3S$	Ajax Finechem Pty Ltd.

4.2 Preparation of black titanium dioxide catalysts

The preparation of black titanium dioxide catalyst proceeded in two steps. The first step was to prepare titanium dioxide via a sol-gel method, and the second step was to convert titanium dioxide in the first step to black titanium dioxide. The 2x2x3 factorial experimental design was employed. The three factors were calcination temperature (factor A), calcination time (factor B), and the molar ratio of reducing agent to catalyst (factor C). Factor A and B were varied at two levels, while factor C was varied at three levels (as seen in Table 4.2). Twelve factorial points were

run with two replicates, resulting in 24 batches of photocatalysts in total (as seen in Table 4.3). The photocatalytic experiments were run under both UV and visible light irradiations and the conversion of methyl orange was the response used in the statistical analysis.

Table 4.2 Preparation parameters for the synthesis of black TiO₂, used in this study

Run	Calcination temperature (°C) (Factor A)	Calcination Time (hours) (Factor B)	Molar ratio of NaBH ₄ / TiO ₂ (Factor C)	Nomenclature
1	400	5	0:1	T400-5
2	500	5	0:1	T500-5
3	400	10	0:1	T400-10
4	500	10	0:1	T500-10
5	400	5	0.5:1	BT400-5-0.5
6	500	5	0.5:1	BT500-5-0.5
7	400	10	0.5:1	BT400-10-0.5
8	500	10	0.5:1	BT500-10-0.5
9	400	5	1:1	BT400-5-1
10	500	5	1:1	BT500-5-1
11	400	10	1:1	BT400-10-1
12	500	10	1:1	BT500-10-1

Table 4.3 List of all TiO₂ catalysts in this study

Run	Replicate I	Starting material	Run	Replicate II	Starting material
1	T400-5 (I)	TiO ₂ xerogel	13	T400-5 (II)	TiO ₂ xerogel
2	T500-5 (I)	TiO ₂ xerogel	14	T500-5 (II)	TiO ₂ xerogel
3	T400-10 (I)	TiO ₂ xerogel	15	T400-10 (II)	TiO ₂ xerogel
4	T500-10 (I)	TiO ₂ xerogel	16	T500-10 (II)	TiO ₂ xerogel
5	BT400-5-0.5 (I)	T400-5 (I)	17	BT400-5-0.5 (II)	T400-5 (II)
6	BT500-5-0.5 (I)	T500-5 (I)	18	BT500-5-0.5 (II)	T500-5 (II)
7	BT400-10-0.5 (I)	T400-10 (I)	19	BT400-10-0.5 (II)	T400-10 (II)
8	BT500-10-0.5 (I)	T500-10 (I)	20	BT500-10-0.5 (II)	T500-10 (II)
9	BT400-5-1 (I)	T400-5 (I)	21	BT400-5-1 (II)	T400-5 (II)
10	BT500-5-1 (I)	T500-5 (I)	22	BT500-5-1 (II)	T500-5 (II)
11	BT400-10-1 (I)	T400-10 (I)	23	BT400-10-1 (II)	T400-10 (II)
12	BT500-10-1 (I)	T500-10 (I)	24	BT500-10-1 (II)	T500-10 (II)

4.2.1 Preparation of titanium dioxide via sol-gel method

Titanium dioxide was synthesized via a sol-gel method by mixing titanium tetraisopropoxide (TTIP) in deionized water (DI) containing 70% nitric acid as the volume ratio of TTIP: DI water: HNO₃ was 1:12:0.087. After adding TTIP, a white precipitate formed instantaneously. The mixture was stirred for 3 days until clear sol was obtained. Then the clear sol was dialyzed in cellulose membrane with a molecular weight cutoff of 3500. The distilled water used in dialysis was changed daily until a pH of sol reached 3.3-3.5. Finally, the sol was dried and the xerogel was calcined at 400 or 500 °C for 5 hours or 10 hours in an air atmosphere. The products were denoted as T400-5, T500-5, T400-10, and T500-10, respectively.

4.2.2 Preparation of black titanium dioxide by the chemical reduction method

Typically, 3.0 g of TiO₂ nanoparticles powder (from 4.2.1) and NaBH₄ (0, 0.71, and 1.42 g corresponding to the molar ratios NaBH₄ to TiO₂ of 0:1, 0.5:1, and

1:1, respectively) were mixed and ground thoroughly for at least 30 minutes. Then the mixtures were charged in a porcelain boat, placed in a tubular furnace, and heated to 400 or 500 °C with a heating rate of 10 °C min⁻¹ for 5 hours or 10 hours under an N₂ atmosphere. After cooling down to room temperature, the resulting black powder was washed with deionized water and ethanol to remove the unreacted NaBH₄ and dried at 70 °C in drying oven. The products were listed in Table 4.3.

4.3 Photocatalytic experiments

The photocatalytic activity of the catalyst was studied for the photocatalytic degradation of methyl orange under both UV and visible light irradiations at ambient temperature. Initially, 0.40 g of catalyst was dispersed in 400 mL of an aqueous solution of 10 ppm methyl orange inside an annular photocatalytic reactor within a closed wooden box (see Figure 4.1). Then the mixture was stirred in the absence of light for one hour to achieve adsorption equilibrium. After that, the mixture was exposed to either UV irradiation using 75W Philips UV-C lamps or visible light irradiation using 18W Philips TL-D standard colors lamps. During 180 minutes of irradiation, 5 mL of the solution was extracted every 15 minutes in order to measure the concentration of methyl orange using UV-visible spectrophotometer at $\lambda_{\text{max}} = 464$ nm. The removal percentage (η) was calculated as follows :

$$\eta(\%) = \frac{C_0 - C_t}{C_0} \times 100\% \quad (4.1)$$

Where η is the removal percentage (%) of reaction, C_0 and C_t are the concentrations of methyl orange at initial and different irradiation time, respectively.

The apparent rate constant (k , min⁻¹) of the catalysts are calculated from a slope of a pseudo first-order plot (see Equation 4.2)

$$\ln \left(\frac{C_t}{C_0} \right) = -kt \quad (4.2)$$

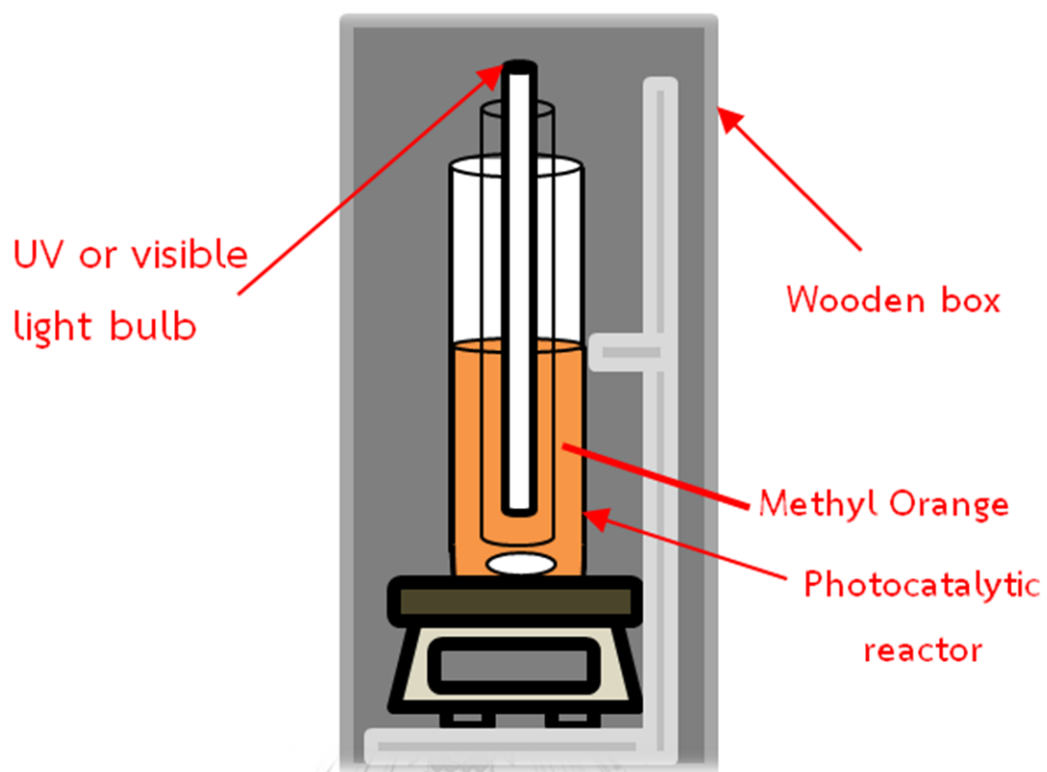


Figure 4.1 The photocatalytic reactor set for the experiments

4.4 Physical and electrochemical characterization

4.4.1 X-ray diffraction (XRD)

X-ray diffractometry (XRD) analysis was performed using a SIEMENS D5000. X-ray diffractometer with a $\text{CuK}\alpha$ radiation source ($\lambda=1.5418 \text{ \AA}$) at a scan rate of 0.50 min^{-1} in the 2θ range between 20 to 80° . The XRD spectra were used to determine crystalline phase and crystallite size of the catalysts.

4.4.2 Nitrogen physisorption

N_2 physisorption technique was performed using Micromeritics ASAP 2020 surface area analyzer to measure the BET specific surface area, pore volume, and pore size distribution. Approximately 0.05 g of catalyst was placed inside the tube to perform N_2 adsorption measurement at 77 K . The sample was degassed at $200 \text{ }^\circ\text{C}$ for one hour.

4.4.3 Photoluminescence spectroscopy (PL)

Photoluminescence (PL) measurement was carried out to study the recombination of electrons and holes on a Horiba Fluoromax Spectrofluorometer at Center of Nanoscience and Nanotechnology, Faculty of Sciences, Mahidol University using a Xenon lamp as the excitation source at room temperature. Photoluminescence measurement was scanned in the range of $350\text{-}600 \text{ nm}$ using an excitation wavelength of 325 nm .

4.4.4 X-ray photoelectron spectroscopy (XPS)

X-ray photoelectron spectroscopy (XPS) was executed on a Kratos Amicus/ESCA 3400 with $\text{AlK}\alpha$ X-ray source with a resolution of 0.1 eV . All binding energies were calibrated for the correction of charging shift with the $\text{C } 1\text{S}$ line which was taken as an internal standard at photoemission peak of 285.0 eV . Photoemission peak area was determined after smoothing and background subtraction using a linear routine. XPS spectra were scanned to determine the element present on the surface of each sample. An element in the sample will give rise to a characteristic set of

peaks at particular energies and the intensity of the peaks is related to the atomic concentration of the element in the sample.

4.4.5 UV-visible reflectance spectroscopy (UV-Vis)

The concentration of methyl orange was measured by Perkin Elmer Lambda 650 spectrophotometer at a wavelength of 464 nm. To study the light absorption characteristics, absorption spectra of the photocatalysts were also obtained by Perkin Elmer Lambda 650 spectrophotometer in the wavelength range of 200-800 nm with a step size of 1 nm. The band gap of the samples were determined by calculating E_g and $(\alpha\text{eV})^2$ (see Equation 4.3 and 4.4), then plot E_g (x-axis) against $(\alpha\text{eV})^2$ (y-axis), and the extrapolation of the linear part until its intersection with E_g axis.

$$E_g = \frac{1240}{\lambda} \quad (4.3)$$

$$\text{and } (\alpha\text{eV})^2 = \left(\ln \left(\frac{10^{(2-A)}}{100} \right) \times E_g \right)^2 \quad (4.4)$$

Where E_g is bandgap energy (eV) of the samples

λ is the wavelength of spectrum (200-800 nm)

A = Absorbance

α = The absorption coefficient in cm^{-1}

1 eV = 1.60×10^{-19} J

4.4.6 Fourier transform infrared spectroscopy (FTIR)

Fourier transform infrared spectroscopy (FTIR) was performed to determine functional groups present in the catalysts by using Thermo Scientific Nicolet 6700 FT-IR spectrometer with an ATR-FTIR spectrometer at a number of the scan was 300 in the wavelength of $400\text{-}4000 \text{ cm}^{-1}$. The absorbance spectrum shows various absorbance peaks, which represent different functional groups.

4.5 Statistical analysis

Minitab Statistical Software (Minitab Release 16) was employed to analyze the data obtained from the experiments. A 2x2x3 factorial experimental design was used to examine the relationship between three factors. The program determined the significance of the main effects and their interactions using analysis of variance. The program also assessed the validity of the statistical model using residual analysis.



CHAPTER 5

RESULTS AND DISCUSSION

This chapter presents the results and discussion, which are classified into three parts. The first part discusses the characterization of all photocatalysts by several techniques including XRD, N₂ physisorption, XPS, PL, UV-vis, and FTIR. The second part discusses about the photocatalytic activity measurement for the degradation of methyl orange. The final part discusses about statistical analysis including three main effects and their interactions, the analysis of variance (ANOVA), and the analysis of residuals.

5.1 Characterization of the catalysts

5.1.1 Phase structure analysis (XRD)

The phase structure of all photocatalysts were determined by X-ray diffractometry (XRD) analysis. All the catalysts that were calcined at different conditions as represented in Table 5.1. Their XRD patterns can be classified into four groups of catalysts which were calcined at four different calcination temperature and time (400 °C 5 hours, 400 °C 10 hours , 500 °C 5 hours, and 500 °C 10 hours) including four white TiO₂ catalysts (a, d, g, and j) and eight black TiO₂ catalysts that were obtained from the reduction process of white TiO₂ by using different molar ratio of reducing agent (NaBH₄) to TiO₂ catalyst (0.5:1 and 1:1) as showed in Figure 5.1 and Figure 5.2.

For white TiO₂ catalysts that were prepared by sol-gel method as the starting materials for the synthesis of black TiO₂, their diffraction peaks at 2θ values of 25.3°, 37.9°, 48.1°, 53.8°, 62.9°, 69.0°, and 75.3° corresponded to anatase phase while diffraction peaks at 27.4°, 36.1°, and 41.3° were assigned to rutile phase. A small peak associated with the brookite phase were detected at 30.8°. These

diffraction peaks was clearly observed in white TiO_2 due to their high crystallinity [41-42].

The phase composition of white TiO_2 catalysts and their crystallite sizes are shown in Table 5.2. Debye-Scherrer equation was used to calculate the crystallite size (see Appendix B). The phase composition of TiO_2 was calculated according to Appendix C when the calcination temperature was increased from 400 to 500 °C, the anatase phase was transformed to rutile phase and the crystallite size of anatase phase grew larger due to the agglomeration and the growth of crystals during calcination process [43]. In addition, the anatase phase was decreased when the calcination time increased to 10 hours at calcination temperature of 400 °C because of the increase in the crystallite size and the agglomeration of nanoparticle. [35]. The TiO_2 catalysts that were calcined at 500 °C for 5 hours and 10 hours had similar phase composition and crystallite size because they consisted of more rutile phase, which is the most stable polymorph [44]. The amount of rutile phase slightly decreased when the calcination time increased from 5 to 10 hours.

From Figures 5.1 and 5.2, XRD patterns of black TiO_2 , which obtained from the chemical reduction of white TiO_2 (a, d, g, and j), had the different characteristic diffraction peaks when compared with white TiO_2 . During the reduction process to synthesize black TiO_2 (b, c, e, f, h, i, k, and l), the crystalline lattice deformation occurred and oxygen vacancies were created [37]. As a result, the intensity of main diffraction peak gradually decreased with increasing calcination temperature, calcination time, and molar ratio of reducing agent used. Also, these weakening and widening of peaks were related to the formation of a shell of amorphous TiO_2 surrounding the crystalline core after reduction process [14]. This reducing agent (NaBH_4) created the defect or oxygen vacancies as a result of its thermal decomposition and the generation of the active hydrogen to attack the crystal surface of TiO_2 [38].

Table 5.1 All white and black TiO₂ catalysts that were used in this study

Order	Calcination temperature (°C) (Factor A)	Calcination Time (hours) (Factor B)	Molar ratio of NaBH ₄ / TiO ₂ (Factor C)	Nomenclature
a	400	5	0:1	T400-5
b	400	5	0.5:1	BT400-5-0.5
c	400	5	1:1	BT400-5-1
d	400	10	0:1	T400-10
e	400	10	0.5:1	BT400-10-0.5
f	400	10	1:1	BT400-10-1
g	500	5	0:1	T500-5
h	500	5	0.5:1	BT500-5-0.5
i	500	5	1:1	BT500-5-1
j	500	10	0:1	T500-10
k	500	10	0.5:1	BT500-10-0.5
l	500	10	1:1	BT500-10-1

Table 5.2 Weight fraction of anatase, rutile and brookite and crystallite size of TiO₂ that used as starting materials for synthesis of black TiO₂

Samples	W _A	W _R	W _B	Crystallite size (nm)
a) T400-5	0.694	0.157	0.149	8.7
d) T400-10	0.617	0.218	0.165	9.1
g) T500-5	0.404	0.528	0.068	13.4
j) T500-10	0.418	0.502	0.078	13.3

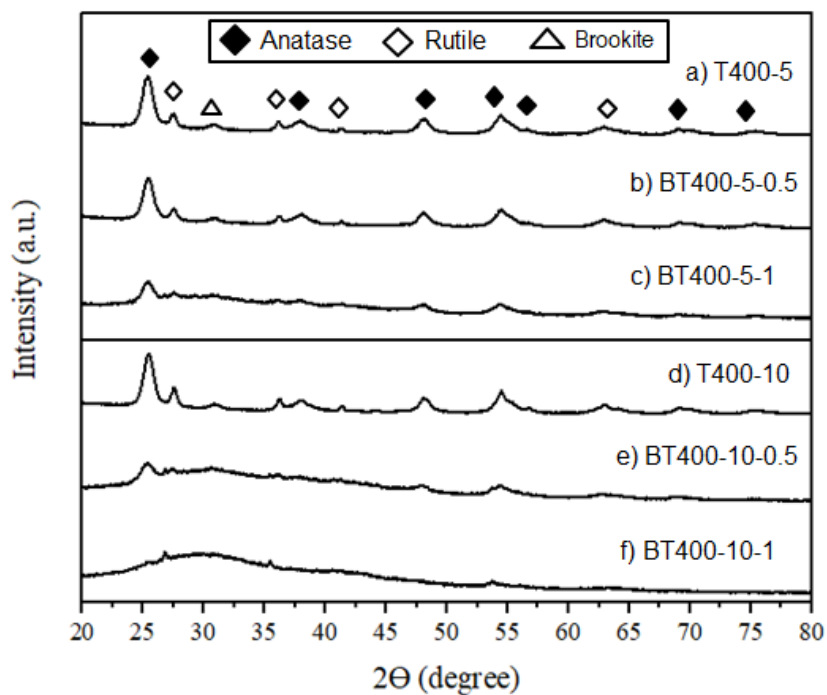


Figure 5.1 XRD patterns of TiO₂ and black TiO₂ calcined at 400 °C for different calcination time and molar ratio of reducing agent

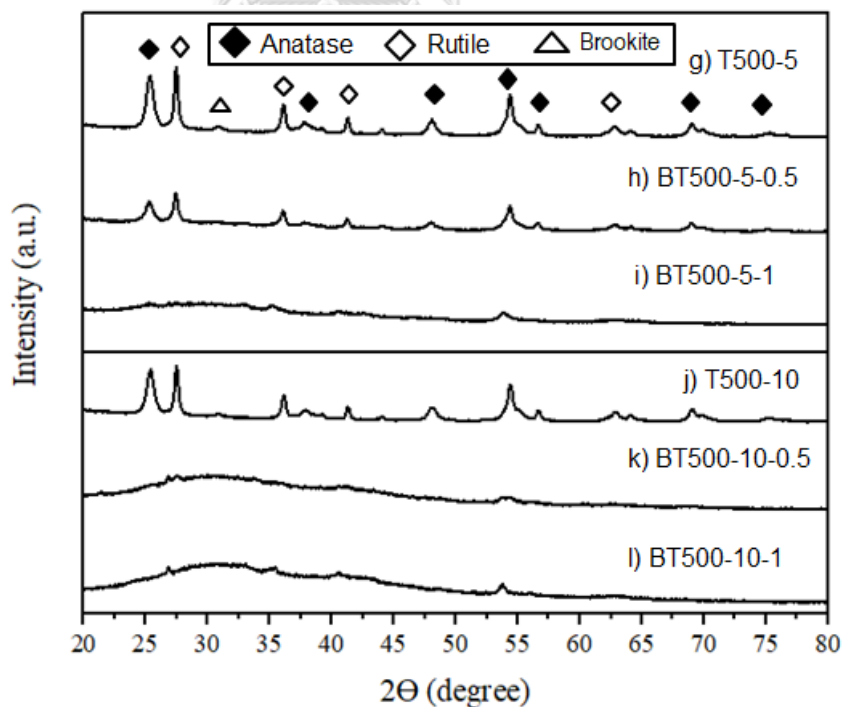


Figure 5.2 XRD patterns of TiO₂ and black TiO₂ calcined at 500 °C for different calcination time and molar ratio of reducing agent

5.1.2 Measurement of specific surface area and pore structure

BET specific surface area, average pore size, and total pore volume of various TiO₂ and black TiO₂ nanoparticles are listed in Table 5.3. They were classified according to the calcination conditions, namely, 400 °C 5 hours, 400 °C 10 hours, 500 °C 5 hours, and 500 °C 10 hours.

For white TiO₂ catalysts, the specific surface areas of catalysts that were calcined at 400 °C were larger than that at 500 °C because of the sintering that occurred in TiO₂ [31]. At the calcination temperature of 400 °C, when the calcination time was increased from 5 to 10 hours, found that the specific surface area of TiO₂ decreased as a result of the particle aggregation, followed by the crystal growth. The specific surface area and pore structure of TiO₂ that was calcined at 500 °C for 10 hours were not different from the one that was calcined for 5 hours because they contained the largest amount of rutile TiO₂, which is the most stable polymorph [45]. These results agreed with XRD data that indicated that were similar crystallite size.

The Nitrogen (N₂) adsorption-desorption isotherms and Barrett-Joyner-Halenda (BJH) pore size distributions of all catalysts with were shown in Figures 5.3-5.10. All TiO₂ catalysts possessed type IV isotherms with the hysteresis loop, suggesting the presence of mesoporous structure [46-47]. At the same conditions, both white TiO₂ and black TiO₂ catalysts exhibited similar narrow pore size distributions. The fact that black TiO₂ catalysts had similar pore size distribution as white TiO₂ indicated that all catalyst contained regular-shape holes and uniform channels [47].

For black TiO₂ catalysts, their pore structure (average pore size and total pore volume) was altered after the reduction process. However, the pore size distributions did not have positive skew [48]. So the second calcination during the reduction process did not directly affect with the surface area and pore structure of black TiO₂ catalysts. This point would be explained later. The specific surface areas of TiO₂ and black TiO₂ at the calcination temperature of 400 °C were 79-105 m²/g while the specific surface areas of catalysts at the calcination temperature of 500 °C were 42-64 m²/g

Table 5.3 Specific surface area, average pore size diameter, and total pore volume of TiO₂ and black TiO₂ at various conditions.

Samples		BET surface area (m ² /g)	Average pore size (nm)	Total Pore volume (cm ³ /g)
Calcination condition : 400 °C 5 h				
a)	T-400-5	104.95	9.5	0.250
b)	BT-400-5-0.5	79.20	10.4	0.206
c)	BT-400-5-1	105.36	8.5	0.224
Calcination condition : 400 °C 10 h				
d)	T-400-10	79.37	9.7	0.192
e)	BT-400-10-0.5	96.44	8.4	0.213
f)	BT-400-10-1	95.04	7.0	0.166
Calcination condition : 500 °C 5 h				
g)	T-500-5	59.59	12.3	0.183
h)	BT-500-5-0.5	55.13	11.4	0.157
i)	BT-500-5-1	58.40	10.5	0.154
Calcination condition : 500 °C 10 h				
j)	T-500-10	63.85	11.6	0.185
k)	BT-500-10-0.5	43.75	13.1	0.143
l)	BT-500-10-1	42.43	9.7	0.107

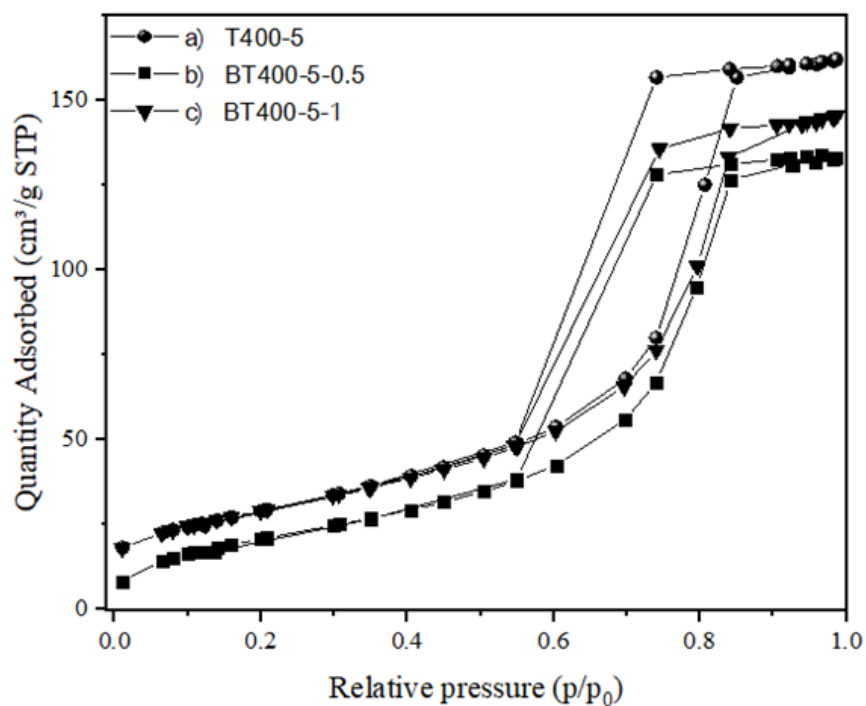


Figure 5.3 N_2 adsorption-desorption isotherm curves of (a) T400-5, (b) BT400-5-0.5 and (c) BT400-5-1

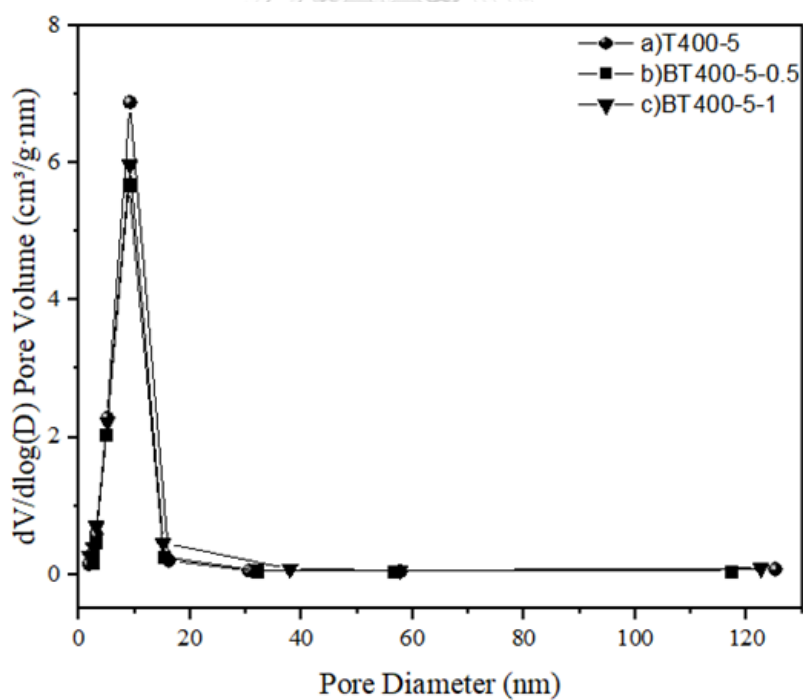


Figure 5.4 BJH pore size distribution plots of (a) T400-5, (b) BT400-5-0.5 and (c) BT400-5-1

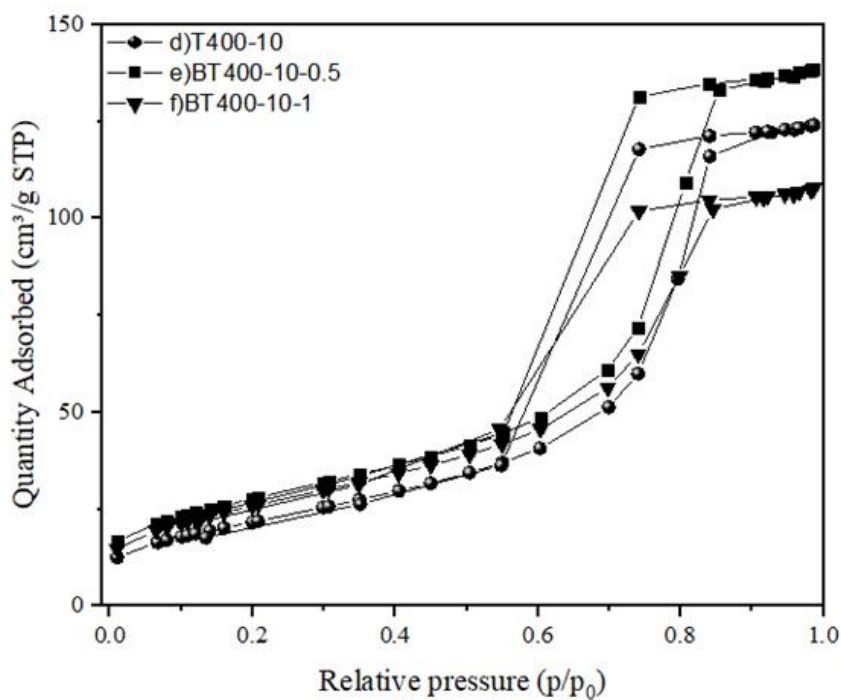


Figure 5.5 N_2 adsorption-desorption isotherm curves of (d) T400-10, (e) BT400-10-0.5 and (f) BT400-10-1

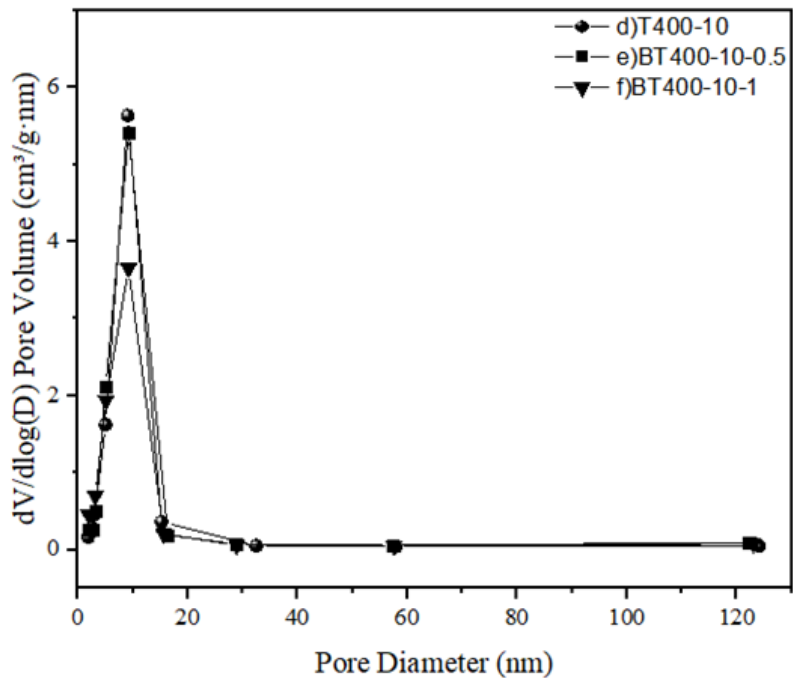


Figure 5.6 BJH pore size distribution plots of (d) T400-10, (e) BT400-10-0.5 and (f) BT400-10-1

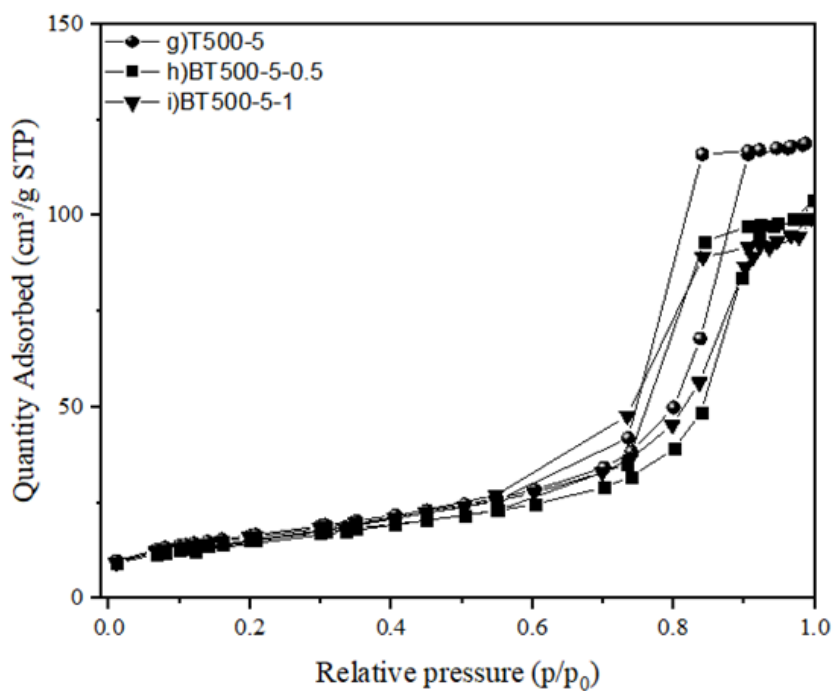


Figure 5.7 N_2 adsorption-desorption isotherm curves of (g) T500-5, (h) BT500-5-0.5 and (i) BT500-5-1

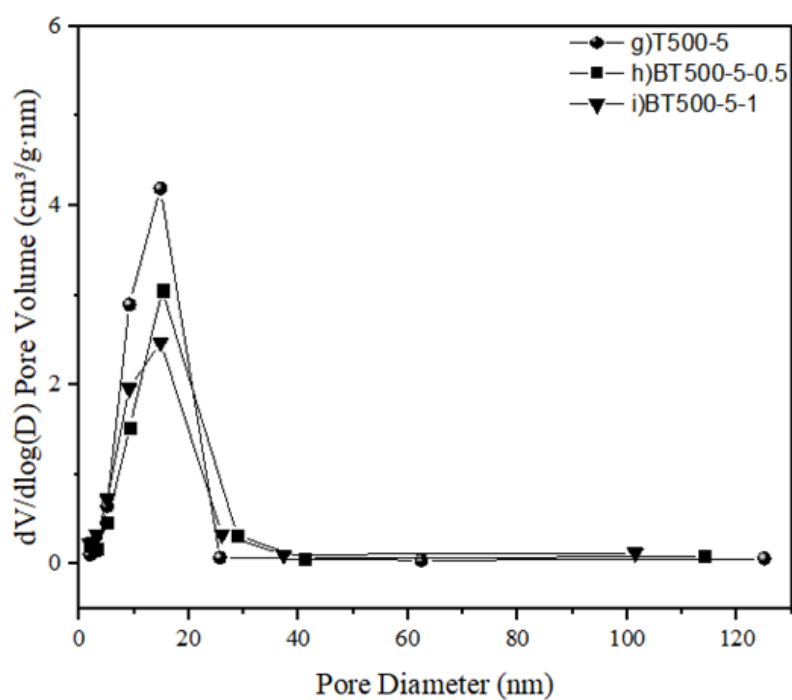


Figure 5.8 BJH pore size distribution plots of (g) T500-5, (h) BT500-5-0.5 and (i) BT500-5-1

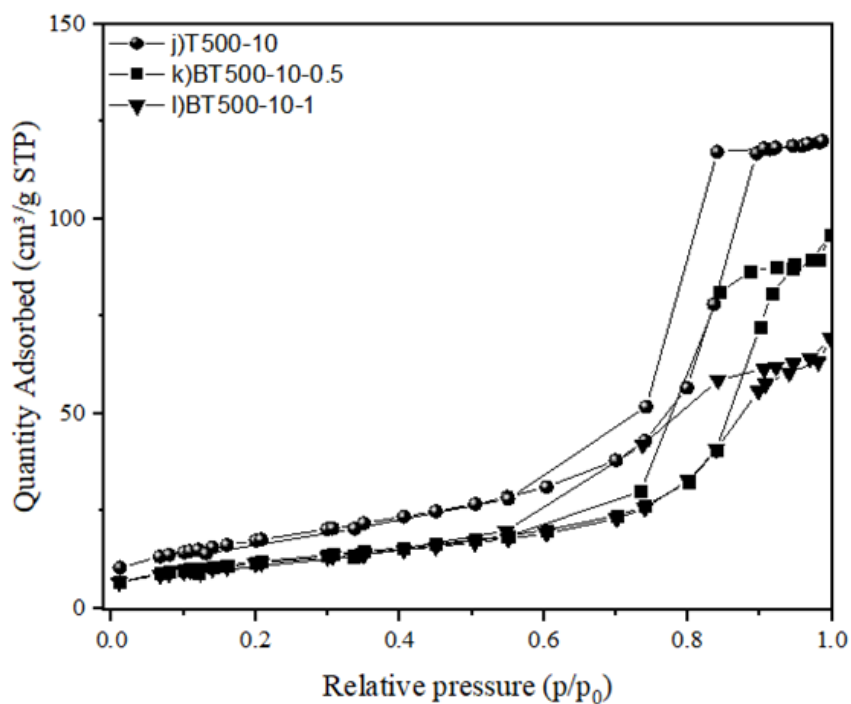


Figure 5.9 N_2 adsorption-desorption isotherm curves of (j) T500-10, (k) BT500-10-0.5 and (l) BT500-10-1

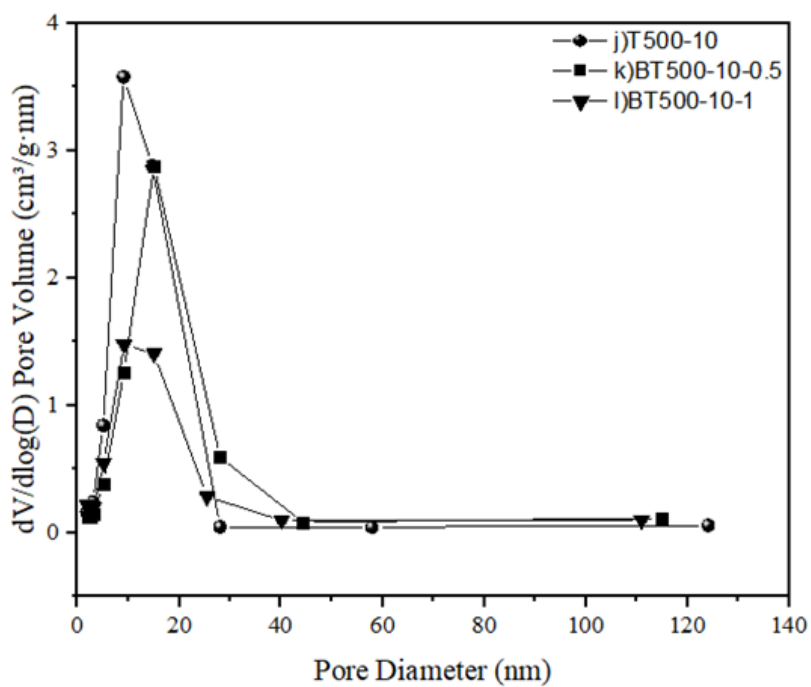


Figure 5.10 N_2 adsorption-desorption isotherm curves of (j) T500-10, (k) BT500-10-0.5 and (l) BT500-10-1

The interactions between three factors that used in the synthesis black TiO_2 had an important effect with the specific surface area and pore structure. This phenomenon was discussed below.

Firstly, sodium borohydride (NaBH_4), the reducing agent, interacted with the surface of TiO_2 at the calcination temperature of 400 or 500°C in N_2 atmosphere since these values of calcination temperature were the appropriate range because the thermal decomposition of NaBH_4 can occur in the range of temperature of 400 to 595 °C [27]. Also, its melting point was 400 °C which was the temperature that released the hydrogen from compound and at higher temperature of 500 °C was its boiling point under vacuum or inert atmosphere [49-51]. That is to say, both values of temperature were the decomposition temperature of NaBH_4 which had the key role to create the oxygen vacancy site or defect on the surface of the catalyst. Also, it can create the shell of amorphous phase during NaBH_4 reduction process to obtain crystalline core/amorphous shell structure due to the gradually weaken and widen the XRD peaks of black TiO_2 [14,37] as shown in Figure 5.1 and 5.2. This phenomenon can give the different values of specific surface areas and pore structure of black TiO_2 catalysts at different calcination temperature.

Secondly, the decomposition of NaBH_4 at higher calcination temperature (500 °C) tended to be more active to release active hydrogen and attacked the crystal surface structure of TiO_2 . This can induce the growth of crystalline or particle size [39, 52] because it tended to have more disordered mesoporous structure which corresponded to an abovementioned amorphous shell or layer [53]. So the surface area may have been decreased because a higher amount of amorphous structure of the shell layer can induce the lattice distortion and the reduction of volume change (pore volume) [54-55].

Most importantly, the increase of calcination time for NaBH_4 reduction process influenced the specific surface area and pore structure of black TiO_2 since it can induce the disorder lattice strain on the surface of catalysts. The trends of specific surface area were clearly different at different condition. For the calcination time of 5 hours, the specific surface areas of black TiO_2 catalysts that used molar ratio of 1:1 were not different from white TiO_2 , which was calcined at the same

calcination temperature (400 or 500 °C) while the specific surface areas of black TiO₂ catalysts that used molar ratio of 0.5:1 decreased because the lower amount of reducing agent to half time may cause the pore collapse and the elimination of internal hydroxyl group during the reduction process [39]. However, they had clearly different trends in both of calcination temperature for the calcination time of 10 hours. In the case of black TiO₂ catalysts that were calcined at 400 °C for 10 hours had larger specific surface areas from white TiO₂ because they had long reduction time to generate disorder surface and surface oxygen vacancies at the treatment for initial release of hydrogen (400 °C) [39,49]; on the contrary, black TiO₂ catalysts that were calcined at 500 °C for 10 hours had decreased specific surface areas from white TiO₂ because they had occurred at higher temperature and long reduction time, may have been affected by providing more active hydrogen to attack the crystalline lattice and inducing more disorder lattice strain on the surface of catalysts [38,39]. So the higher amount of amorphous structure of the shell layer can be generated and it may be opposite effect on the surface of black TiO₂ since the thickness of shell layer may be increased along with the decrease of pore size or volume [56]. This can be explained that the presence of an excessive amorphous shell or layer from the reduction process can block or fill up gaps between the crystalline cores as well as partially clogged the pore entrance. Therefore, the decrease of specific surface area after the reduction process can occur since it prevented N₂ molecule from entering the pore [46, 57].

5.1.3 X-ray photoelectron spectra (XPS) analysis

X-ray photoelectron spectroscopy (XPS) was used to determine the presence of Ti^{3+} defects and oxygen vacancies on the surface of all catalysts (a)-(l). The results are shown in Figure 5.11 – 5.18 along with the curve fitting of the characteristic peaks of titanium and oxygen. Tables 5.4 – 5.11 presents the peak area ratio of $\text{Ti}^{3+} / \text{Ti}^{4+}$ and the percentage of peak area of oxygen in the lattice and oxygen vacancies for all catalysts. To make these data easier to understand, they were classified into four conditions including 400 °C 5 hours, 400 °C 10 hours, 500 °C 5 hours, and 500 °C 10 hours.

From XPS spectra of white TiO_2 catalysts (a, d, g, and j), the ratios of peak area of $\text{Ti}^{3+} / \text{Ti}^{4+}$ were in the range of 0.06 – 0.11 and the percentage of peak area of oxygen vacancies around 17.0 – 22.5. The example of such calculation was shown in Appendix E. The T400-5 catalysts (a) possessed the largest values of $\text{Ti}^{3+} / \text{Ti}^{4+}$ and percentage of oxygen vacancies among all white TiO_2 . Also, it was the mixed phase TiO_2 that consisted of the most active phase as the anatase phase (See Figure 5.1(a)) [44]. So it may have more reaction site and an increase of the number of active sites. Moreover, it can reduce the electron-hole recombination which caused a change in the chemical rate that can act as the surface charge carrier transfer rate [31,51].

From XPS spectra of black TiO_2 catalysts (b, c, e, f, h, i, k, and l) that were synthesized by NaBH_4 reduction process from white TiO_2 by varying calcination temperature and time, found that their characteristic peaks of titanium and oxygen were consistent in the same way with white TiO_2 as showed in Figure 5.11 – 5.18 and Table 5.4 – 5.11. The characteristic peaks around 458.4 – 458.9 eV and 464.1-464.6 eV corresponded to $\text{Ti}^{4+} 2p_{3/2}$ and $2p_{1/2}$ of Ti^{4+} -O bonds, respectively, whereas the peaks at 456.1 – 456.9 eV and 459.8 – 461.1 eV were assigned to the formation of Ti^{3+} defects. The O 1s spectra including two oxygen peaks that were the lattice oxygen (O_L) or the bond of oxygen to titanium (Ti-O) around 529.6 – 530.6 eV and oxygen vacancies (O_V) or a hydroxyl group (O-H) around 531.8 - 532.5 eV. The formation of oxygen vacancies leads to the creation of Ti^{3+} on the surface of catalysts. From data analysis as shown in Table 5.4 – 5.11 indicated that more amount of $\text{Ti}^{3+} / \text{Ti}^{4+}$ related to more surface of oxygen vacancies [38,39,51].

The decomposition of NaBH_4 generated the active hydrogen that reacted with the lattice oxygen (O_L) in white TiO_2 . Consequently, the amount of lattice oxygen decreased and the number of oxygen vacancies and the amount of Ti^{3+} defects on the surface of catalyst grew larger. At the same calcination temperature and time, the addition of reducing agent facilitated an increase in the amount of both values because the larger amount of reducing agent, the more active hydrogen to generate greater defect concentration [58]. Moreover, the decomposition of NaBH_4 at higher calcination temperature ($500\text{ }^\circ\text{C}$) supplied more energy for the active hydrogen to attack crystal surface of TiO_2 . Then the electron that previously contained in the oxygen vacancies state were driven away and transported to Ti^{4+} . The higher calcination temperature also promoted an entropy-driven process or diffusion of the bulk Ti^{3+} defects toward the subsurface Ti^{3+} [51,52]. Lastly, the interactions between the increasing calcination or reduction time and the calcination temperature or the amount of reducing agent for the synthesis of black TiO_2 catalysts can promote the introduction of more disorder lattice strain and surface oxygen vacancies. For this reason, using the most calcination time with a large amount of reducing agent can deform the crystalline lattice in a good way if the calcination temperature were more than the initial release of hydrogen from NaBH_4 ($>400\text{ }^\circ\text{C}$) [39].

From data analysis as in Table 5.10, found that black TiO_2 (l); BT500-10-1 possessed the largest ratio of peak area $\text{Ti}^{3+} / \text{Ti}^{4+}$ and the most oxygen vacancies as 0.26 and 54.92%, respectively. Both of these defects had beneficial effect on photocatalysis because Ti^{3+} and oxygen vacancies served as electron traps to separate electrons and holes [59].

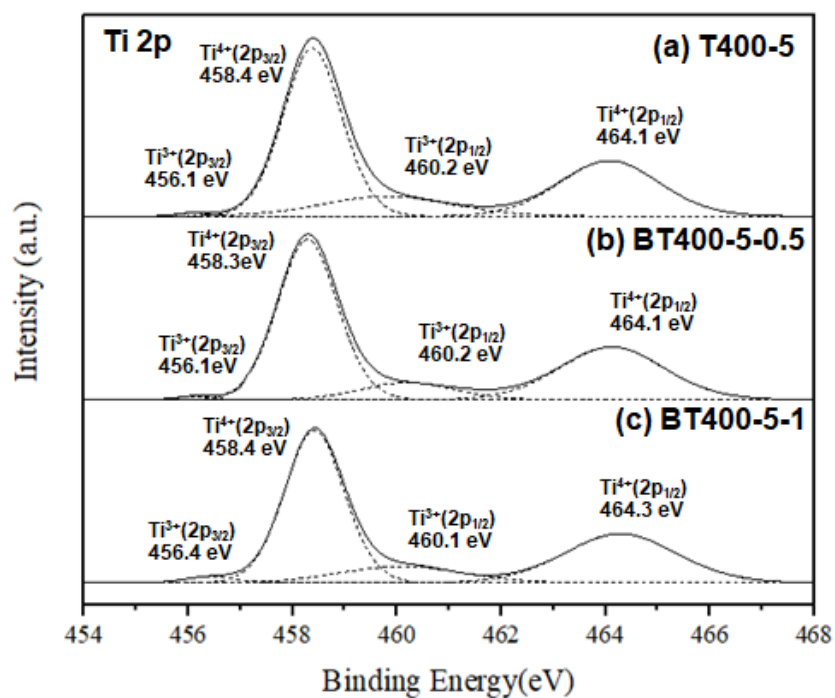


Figure 5.11 XPS spectra; Ti 2p of (a) T400-5, (b) BT400-5-0.5 and (c) BT400-5-1

Table 5.4 The peak area ratios of titanium for TiO_2 calcined at 400 °C 5 h for various amount of reducing agent from XPS results.

Samples	Binding energy (eV)	Peak	Peak Area	%Peak Area	Ratio of peak area $\text{Ti}^{3+} / \text{Ti}^{4+}$
T400-5	464.1	$\text{Ti}^{4+} (2p_{1/2})$	3170.95	89.98	0.111
	458.4	$\text{Ti}^{4+} (2p_{3/2})$	5473.87		
	460.2	$\text{Ti}^{3+} (2p_{1/2})$	931.96	10.02	
	456.1	$\text{Ti}^{3+} (2p_{3/2})$	30.67		
BT400-5-0.5	464.1	$\text{Ti}^{4+} (2p_{1/2})$	3076.87	88.61	0.129
	458.3	$\text{Ti}^{4+} (2p_{3/2})$	5342.78		
	460.2	$\text{Ti}^{3+} (2p_{1/2})$	1017.51	11.39	
	456.1	$\text{Ti}^{3+} (2p_{3/2})$	64.78		
BT400-5-1	464.3	$\text{Ti}^{4+} (2p_{1/2})$	3097.13	86.06	0.162
	458.4	$\text{Ti}^{4+} (2p_{3/2})$	5083.51		
	460.1	$\text{Ti}^{3+} (2p_{1/2})$	1146.00	13.94	
	456.4	$\text{Ti}^{3+} (2p_{3/2})$	178.56		

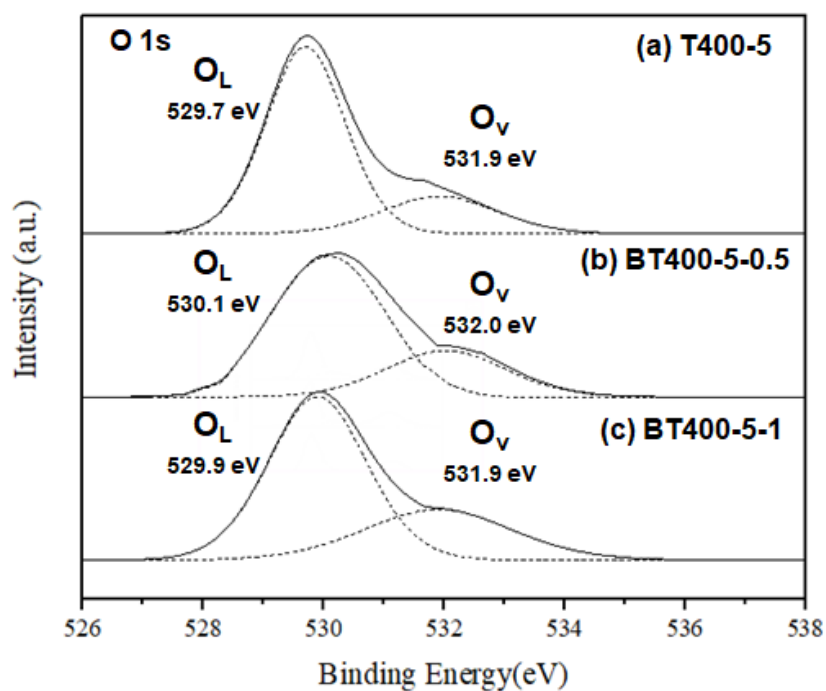


Figure 5.12 XPS spectra; O 1s of (a) T400-5, (b) BT400-5-0.5 and (c) BT400-5-1

Table 5.5 The percentage of peak area of oxygen for TiO₂ calcined at 400 °C 5 h for various amount of reducing agent from XPS results.

Samples	Binding energy (eV)	Peak	Peak Area	%Peak Area
T400-5	531.9	Oxygen vacancies (O _V)	2335.13	22.54
	529.7	Lattice Oxygen (O _L)	8024.30	77.46
BT400-5-0.5	532.0	Oxygen vacancies (O _V)	3012.93	26.58
	530.1	Lattice Oxygen (O _L)	8323.18	73.42
BT400-5-1	531.9	Oxygen vacancies (O _V)	4054.93	31.81
	529.9	Lattice Oxygen (O _L)	8691.85	68.19

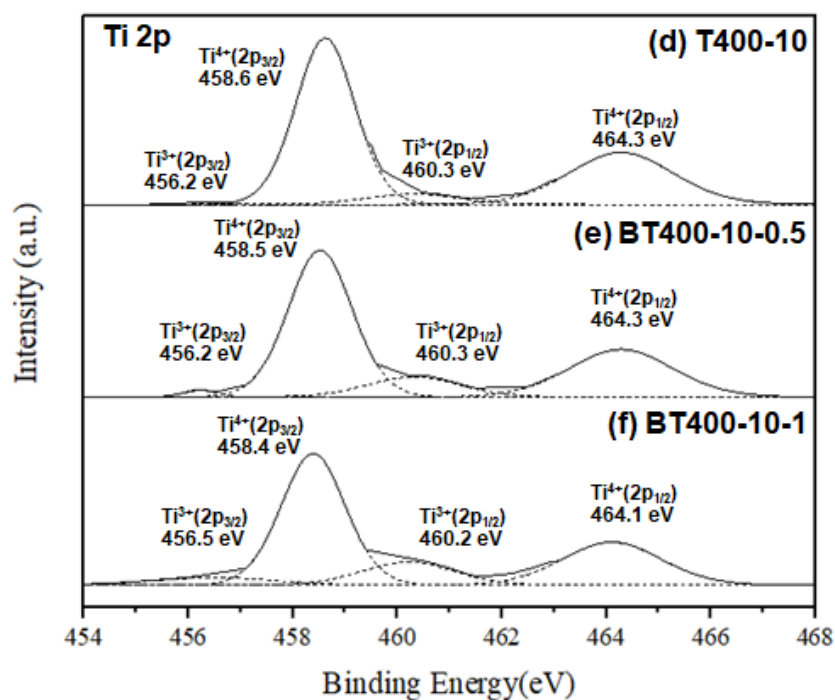


Figure 5.13 XPS spectra; Ti 2p of (d) T400-10, (e) BT400-10-0.5 and (f) BT400-10-1

Table 5.6 The peak area ratios of titanium for TiO₂ calcined at 400 °C 10 h for various amount of reducing agent from XPS results.

Samples	Binding energy (eV)	Peak	Peak Area	%Peak Area	Ratio of peak area Ti ³⁺ / Ti ⁴⁺
T400-10	464.3	Ti ⁴⁺ (2p _{1/2})	3017.18	93.69	0.067
	458.6	Ti ⁴⁺ (2p _{3/2})	5474.08		
	460.3	Ti ³⁺ (2p _{1/2})	533.02	6.31	
	456.2	Ti ³⁺ (2p _{3/2})	38.87		
BT400-10-0.5	464.3	Ti ⁴⁺ (2p _{1/2})	2733.90	87.37	0.145
	458.5	Ti ⁴⁺ (2p _{3/2})	5216.33		
	460.3	Ti ³⁺ (2p _{1/2})	1028.72	12.63	
	456.2	Ti ³⁺ (2p _{3/2})	120.10		
BT400-10-1	464.1	Ti ⁴⁺ (2p _{1/2})	2386.90	80.48	0.243
	458.4	Ti ⁴⁺ (2p _{3/2})	4711.49		
	460.2	Ti ³⁺ (2p _{1/2})	1199.28	19.52	
	456.5	Ti ³⁺ (2p _{3/2})	522.83		

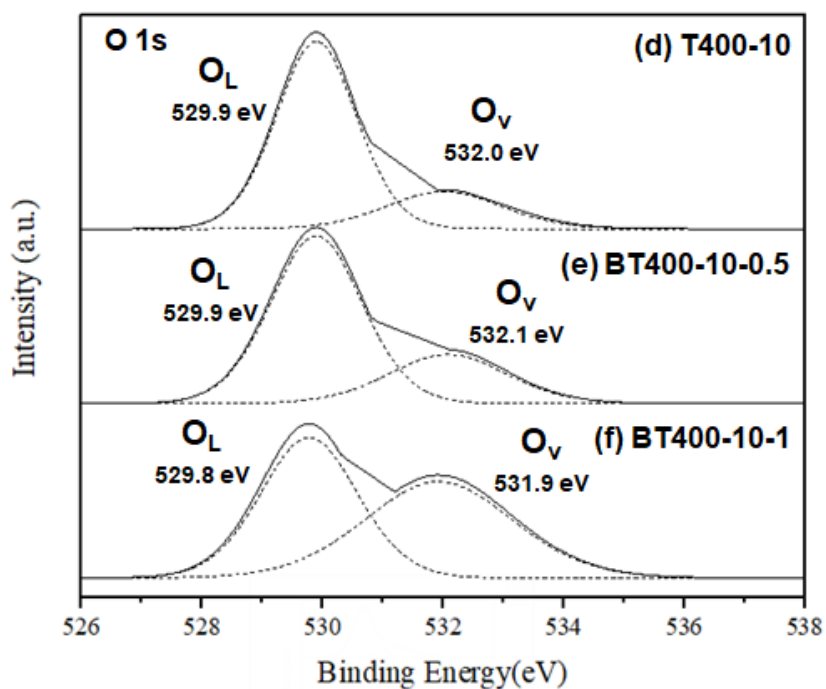


Figure 5.14 XPS spectra; O 1s of (d) T400-10, (e) BT400-10-0.5 and (f) BT400-10-1

Table 5.7 The percentage of peak area of oxygen for TiO_2 calcined at 400 °C 10 h for various amount of reducing agent from XPS results.

Samples	Binding energy (eV)	Peak	Peak Area	%Peak Area
T400-10	532.0	Oxygen vacancies (O_V)	1808.54	18.07
	529.9	Lattice Oxygen (O_L)	8198.10	81.93
BT400-10-0.5	532.1	Oxygen vacancies (O_V)	3134.90	28.56
	529.9	Lattice Oxygen (O_L)	7840.49	71.44
BT400-10-1	531.9	Oxygen vacancies (O_V)	7761.54	51.20
	529.8	Lattice Oxygen (O_L)	7399.06	48.80

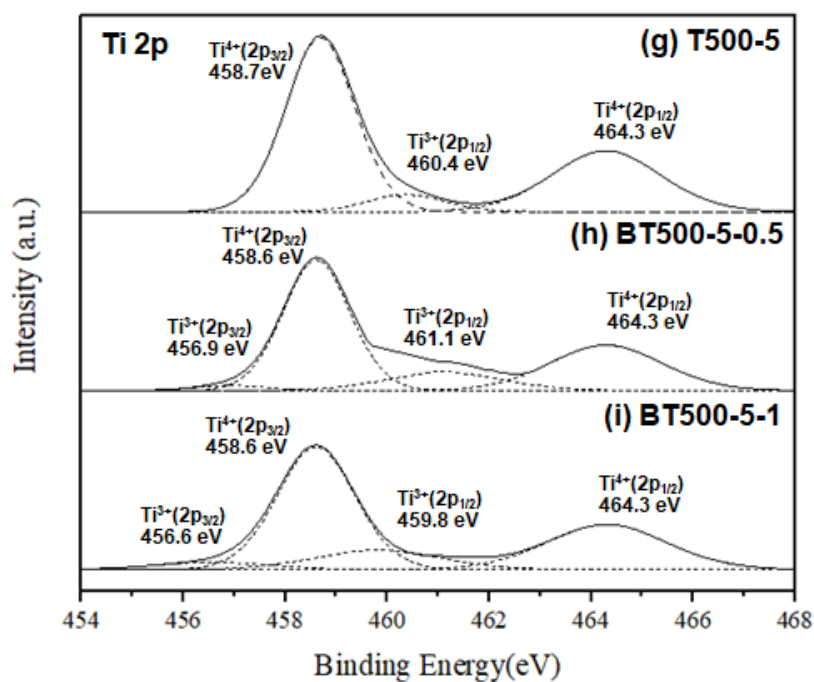


Figure 5.15 XPS spectra; Ti 2p of (g) T500-5, (h) BT500-5-0.5 and (i) BT500-5-1

Table 5.8 The peak area ratios of titanium for TiO_2 calcined at 500 °C 5 h for various amount of reducing agent from XPS results.

Samples	Binding energy (eV)	Peak	Peak Area	%Peak Area	Ratio of peak area $\text{Ti}^{3+} / \text{Ti}^{4+}$
T500-5	464.3	$\text{Ti}^{4+} (2p_{1/2})$	3921.29	93.27	0.072
	458.7	$\text{Ti}^{4+} (2p_{3/2})$	7045.26		
	460.4	$\text{Ti}^{3+} (2p_{1/2})$	791.18		
BT500-5-0.5	464.3	$\text{Ti}^{4+} (2p_{1/2})$	3018.01	83.21	0.202
	458.6	$\text{Ti}^{4+} (2p_{3/2})$	5142.16		
	461.1	$\text{Ti}^{3+} (2p_{1/2})$	1266.82	16.79	
	456.9	$\text{Ti}^{3+} (2p_{3/2})$	379.94		
BT500-5-1	464.3	$\text{Ti}^{4+} (2p_{1/2})$	3194.56	81.77	0.223
	458.6	$\text{Ti}^{4+} (2p_{3/2})$	5624.08		
	459.8	$\text{Ti}^{3+} (2p_{1/2})$	1448.10	18.23	
	456.6	$\text{Ti}^{3+} (2p_{3/2})$	517.62		

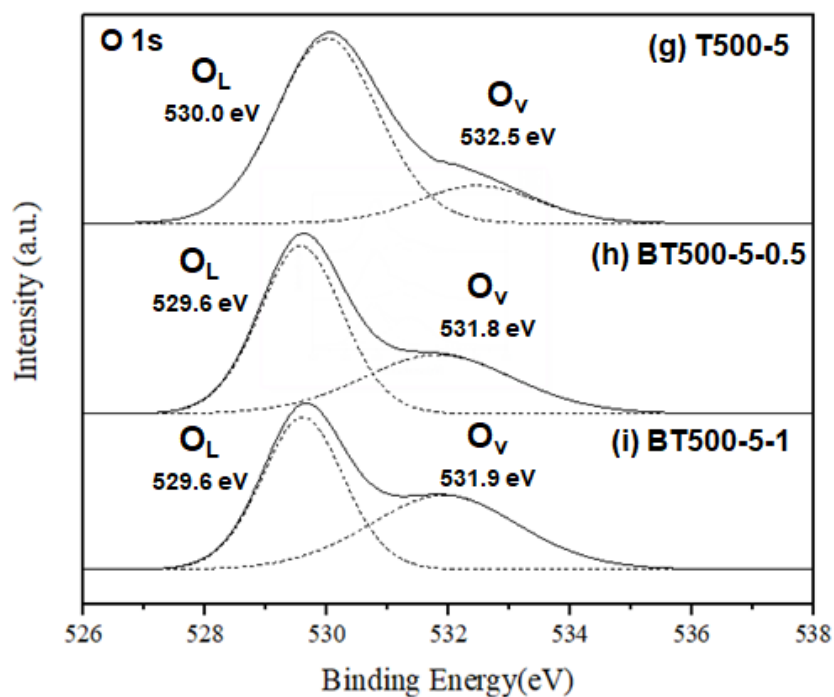


Figure 5.16 XPS spectra; O 1s of (g) T500-5, (h) BT500-5-0.5 and (i) BT500-5-1

Table 5.9 The percentage of peak area of oxygen for TiO₂ calcined at 500 °C 5 h for various amount of reducing agent from XPS results.

Samples	Binding energy (eV)	Peak	Peak Area	%Peak Area
T500-5	532.5	Oxygen vacancies (O _V)	2702.50	19.10
	530.0	Lattice Oxygen (O _L)	11447.50	80.90
BT500-5-0.5	531.8	Oxygen vacancies (O _V)	5406.33	39.01
	529.6	Lattice Oxygen (O _L)	8455.06	60.99
BT500-5-1	531.9	Oxygen vacancies (O _V)	6690.98	47.03
	529.6	Lattice Oxygen (O _L)	7537.25	52.97

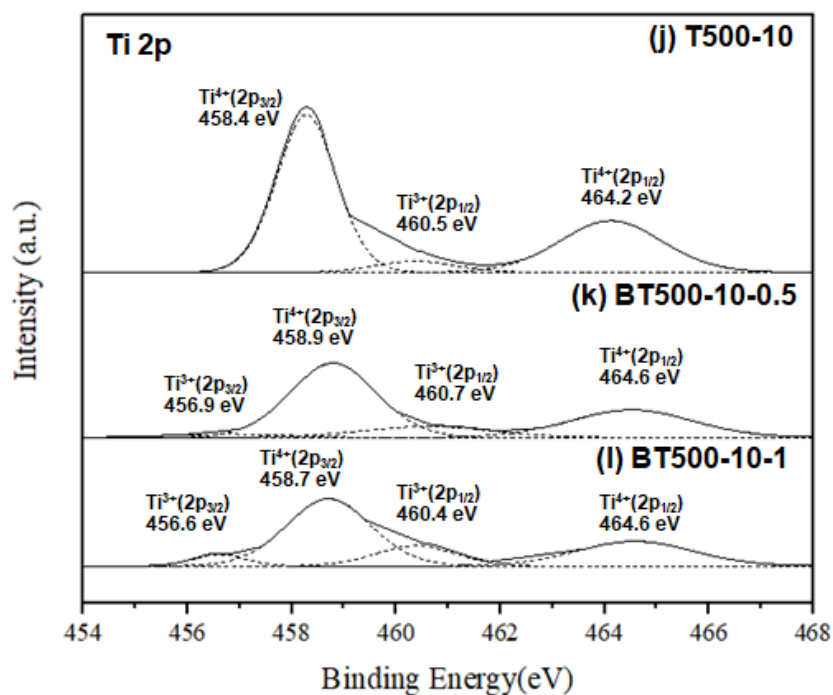


Figure 5.17 XPS spectra; Ti 2p of (j) T500-10, (k) BT500-10-0.5 and (l) BT500-10-1

Table 5.10 The peak area ratios of titanium for TiO₂ calcined at 500 °C 10 h for various amount of reducing agent from XPS results.

Samples	Binding energy (eV)	Peak	Peak Area	%Peak Area	Ratio of peak area Ti ³⁺ / Ti ⁴⁺
T500-10	464.2	Ti ⁴⁺ (2p _{1/2})	3505.72	94.26	0.061
	458.4	Ti ⁴⁺ (2p _{3/2})	6247.30		
	460.5	Ti ³⁺ (2p _{1/2})	593.39		
BT500-10-0.5	464.6	Ti ⁴⁺ (2p _{1/2})	2257.86	84.13	0.189
	458.9	Ti ⁴⁺ (2p _{3/2})	4289.20		
	460.7	Ti ³⁺ (2p _{1/2})	955.74		
	456.9	Ti ³⁺ (2p _{3/2})	279.02		
BT500-10-1	464.6	Ti ⁴⁺ (2p _{1/2})	1943.17	79.34	0.260
	458.7	Ti ⁴⁺ (2p _{3/2})	3792.85		
	460.4	Ti ³⁺ (2p _{1/2})	1091.83		
	456.6	Ti ³⁺ (2p _{3/2})	401.77		

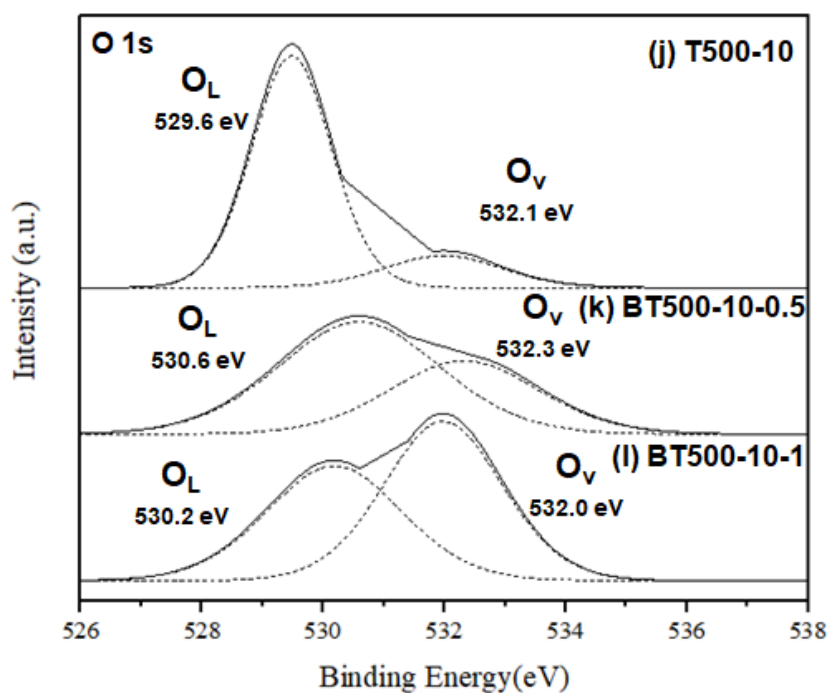


Figure 5.18 XPS spectra; O 1s of (j) T500-10, (k) BT500-10-0.5 and (l) BT500-10-1

Table 5.11 The percentage of peak area of oxygen for TiO₂ calcined at 500 °C 10 h for various amount of reducing agent from XPS results.

Samples	Binding energy (eV)	Peak	Peak Area	%Peak Area
T500-10	532.1	Oxygen vacancies (O _V)	1905.26	16.98
	529.6	Lattice Oxygen (O _L)	9312.92	83.02
BT500-10-0.5	532.3	Oxygen vacancies (O _V)	5486.61	37.60
	530.6	Lattice Oxygen (O _L)	9104.11	62.40
BT500-10-1	532.0	Oxygen vacancies (O _V)	9458.76	54.92
	530.2	Lattice Oxygen (O _L)	7764.63	45.08

5.1.4 Photoluminescence (PL) spectra analysis

The photoluminescence (PL) spectra were analyzed to determine how fast the recombination of electrons and holes were for white and black TiO₂. The results are shown in Figure 5.19 - 5.23 for four groups of TiO₂ catalyst and Figure 5.23 presents the comparison of PL spectra for all catalysts. The PL measurement was operated in the wavelength range of 350-600 nm with the excitation wavelength at 325 nm. From the PL spectra of white TiO₂ catalysts (a, d, g, and j), strong PL emission intensities were detected around 425 – 500 nm, corresponding to the fast recombination rate of photo-excited electrons and holes. The main emission peak around 467 nm was a consequence of oxygen vacancies on the surface [60]. The PL spectra of black TiO₂ catalysts exhibited similar emission peak positions as white TiO₂ but the peak intensities of black TiO₂ were lower than those of white TiO₂. Therefore, black TiO₂ was better at suppressing the recombination of electrons and holes. The PL emission peaks of black TiO₂ that was synthesized with a higher amount of reducing agent were found to be weaker because more defects or hydroxyl (OH) species that was formed act as electron traps and O₂ binding sites [59]. Consequently, they enhanced the photocatalytic activity because electron separation on the surface terminal sites was more efficient [40]. These PL spectra results were consistent with previous XPS results and it could be explained in terms of the effects of all three factors in the same way.

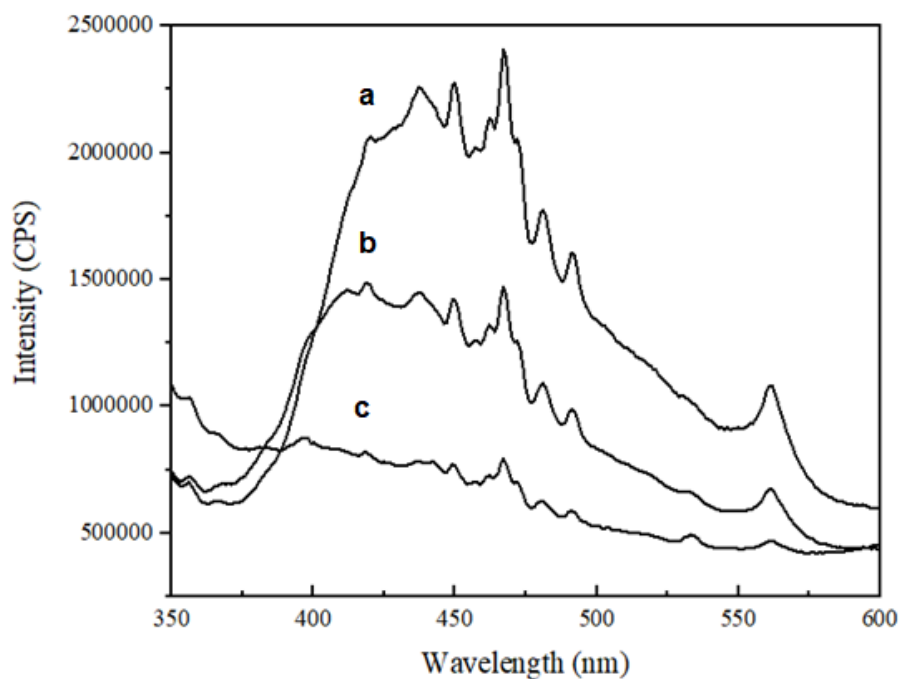


Figure 5.19 Photoluminescence spectra of (a) T400-5, (b) BT400-5-0.5 and (c) BT400-5-1 with the excitation wavelength at 325 nm

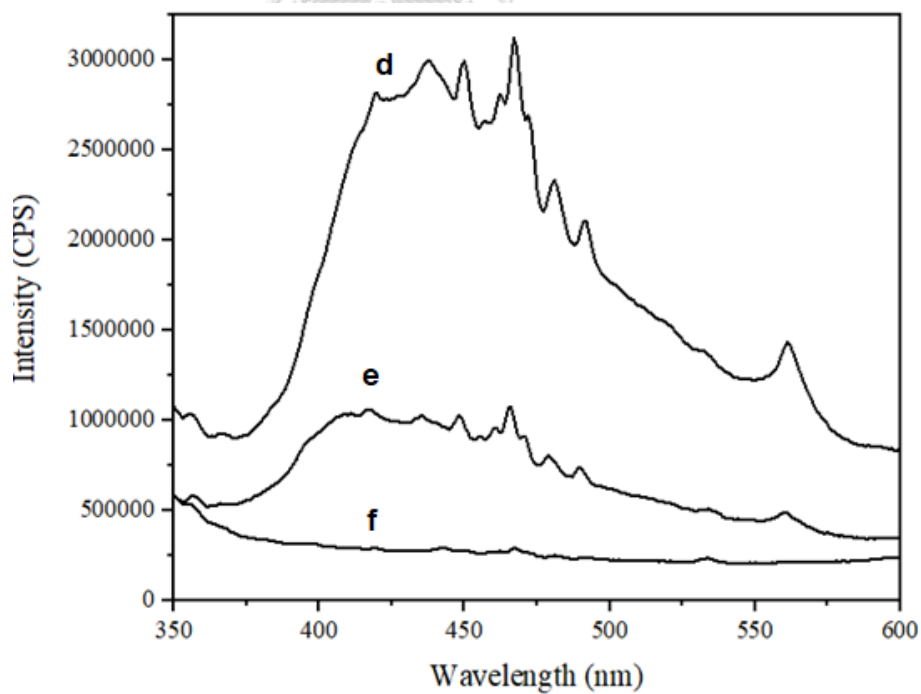


Figure 5.20 Photoluminescence spectra of (d) T400-10, (e) BT400-10-0.5 and (f) BT400-10-1 with the excitation wavelength at 325 nm

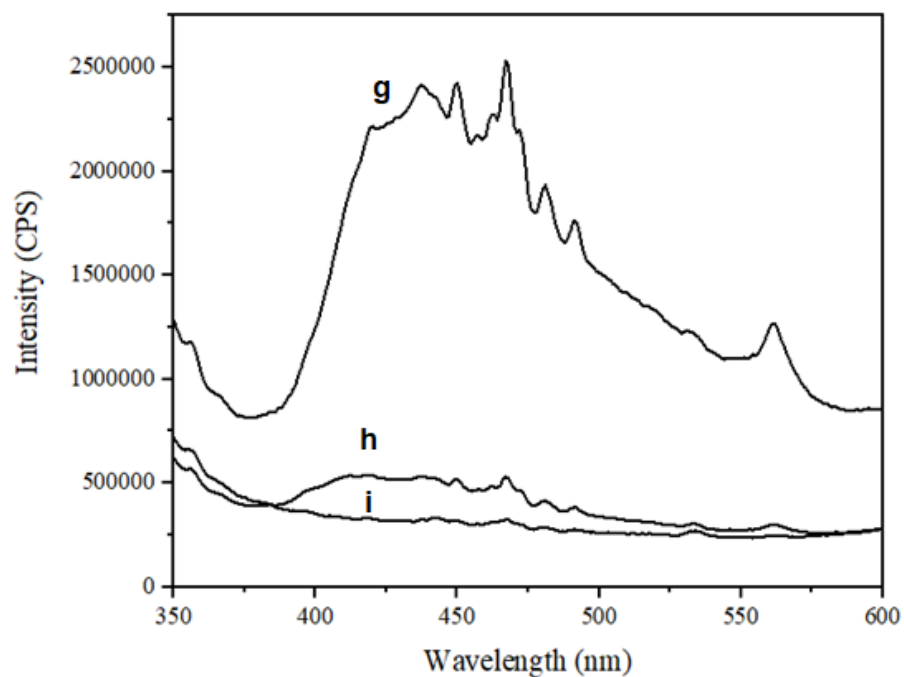


Figure 5.21 Photoluminescence spectra of (g) T500-5, (h) BT500-5-0.5 and (i) BT500-5-1 with the excitation wavelength at 325 nm

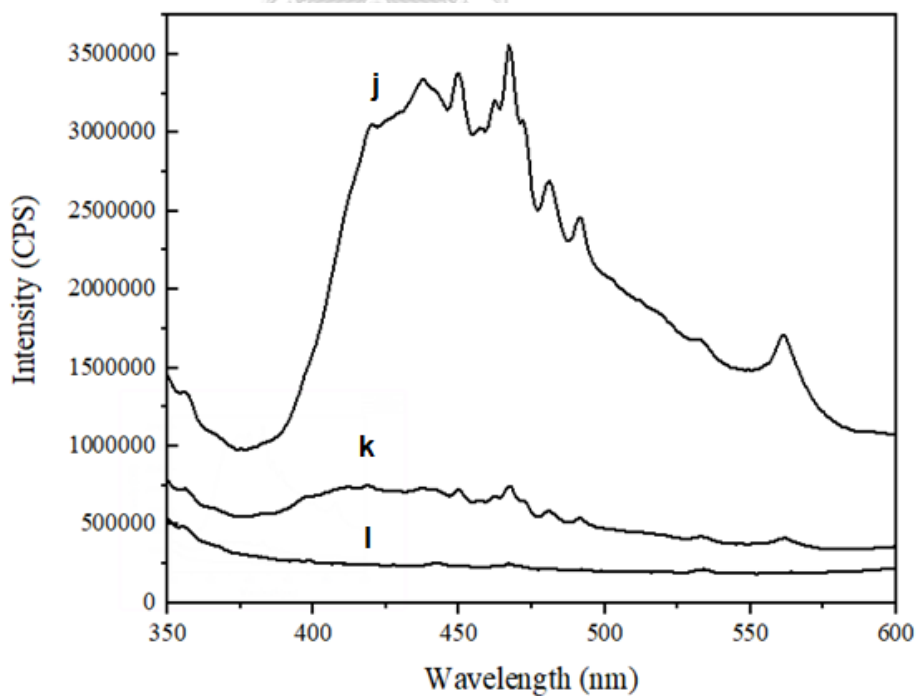


Figure 5.22 Photoluminescence spectra of (j) T500-10, (k) BT500-10-0.5 and (l) BT500-10-1 with the excitation wavelength at 325 nm

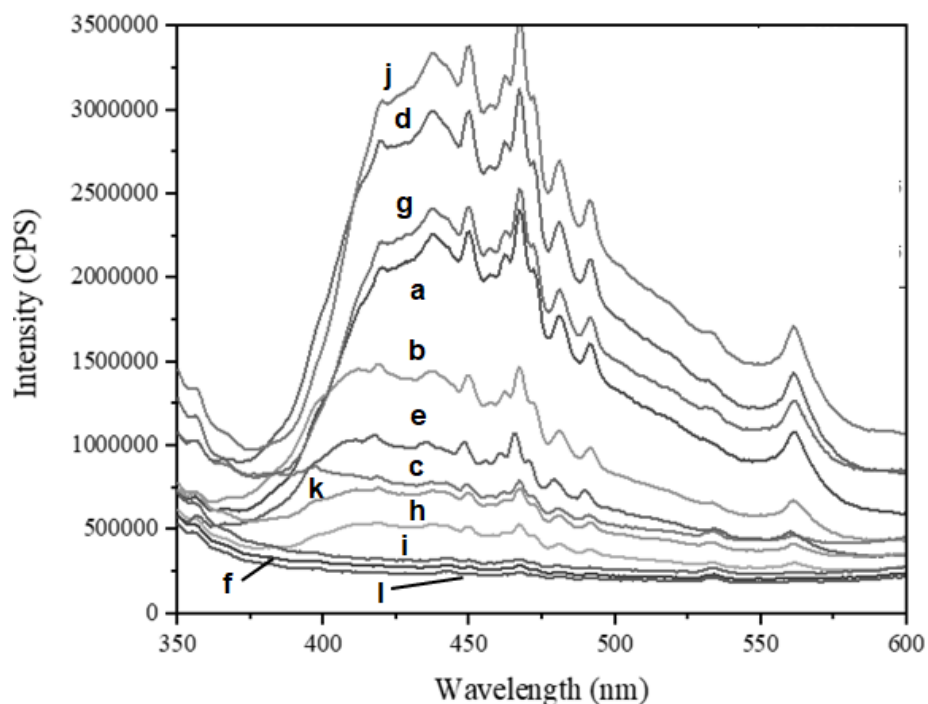


Figure 5.23 Photoluminescence spectra of all catalysts; (a)-(l) with the excitation wavelength at 325 nm

5.1.5 UV-visible reflectance spectra (UV-Vis) analysis

The UV-visible reflectance (UV-vis) spectra in the range of 200 to 800 nm were obtained to determine the optical absorption properties of all photocatalysts. From Figure 5.24, the white TiO_2 catalysts (a, d, g, and j) had no absorption in the visible region (>420 nm) but great absorption in UV region. When white TiO_2 catalysts were converted to black TiO_2 by NaBH_4 reduction process, the absorption in the visible region significantly improved. Since they had high enough defect concentration to create a new band of electronic state that leads to absorb more light in visible region [38,51].

The band gap energy of TiO_2 was determined from a Tauc plot of photon energy versus the Kubelka-Munk function (see Appendix F). The plots were presented in Figures 5.25 – 5.28 and the band gap energy of all catalysts was listed in Table 5.12. The band gap energy of black TiO_2 ranged from 1.70 to 2.98 eV and was narrower than that of white TiO_2 catalysts (ca. 3.03 - 3.10 eV). During the NaBH_4 reduction process, oxygen vacancies or the defect states (reducing Ti^{4+} to Ti^{3+}) was

created, leading to a new energy level between conduction band (CB) and valence band (VB). The creation of additional electronic states below the conduction band (CB) edge at energy level position around 0.75 to 1.18 eV enabled the light absorption in the visible region [14, 59, 61]. This indicated that the optical properties of black TiO₂ catalysts were improved due to the strong absorption and the narrow band gap energy.

As a consequence, the photo-excitation of electrons from the valence band edge position to the conduction band edge position was easier, resulting in the enhancement of the photocatalytic degradation efficiency [40].

Among all catalysts, the band gap energy of BT500-10-1 (1.70 eV) was the narrowest one owing to the most abundant Ti³⁺ defects and oxygen vacancies as confirmed by XPS results. When considered the overall results, the trend observed in these UV-vis reflectance spectra results was consistent with previous XPS and PL results.

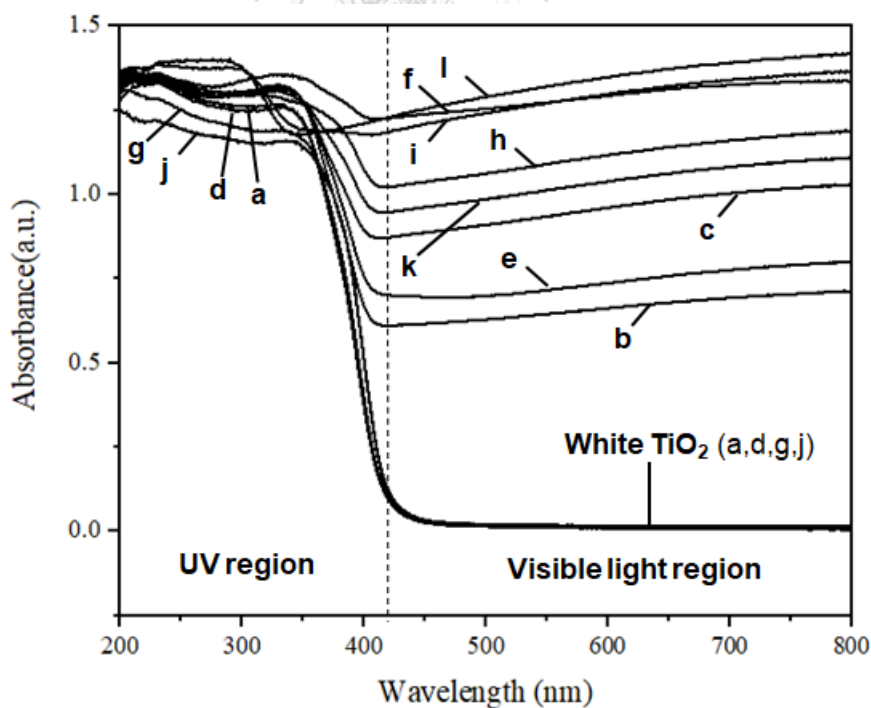


Figure 5.24 UV-Vis absorption spectra of (a) T400-5, (b) BT400-5-0.5, (c) BT400-5-1, (d) T400-10, (e) BT400-10-0.5, (f) BT400-10-1, (g) T500-5, (h) BT500-5-0.5, (i) BT500-5-1, (j) T500-10, (k) BT500-10-0.5 and (l) BT500-10-1

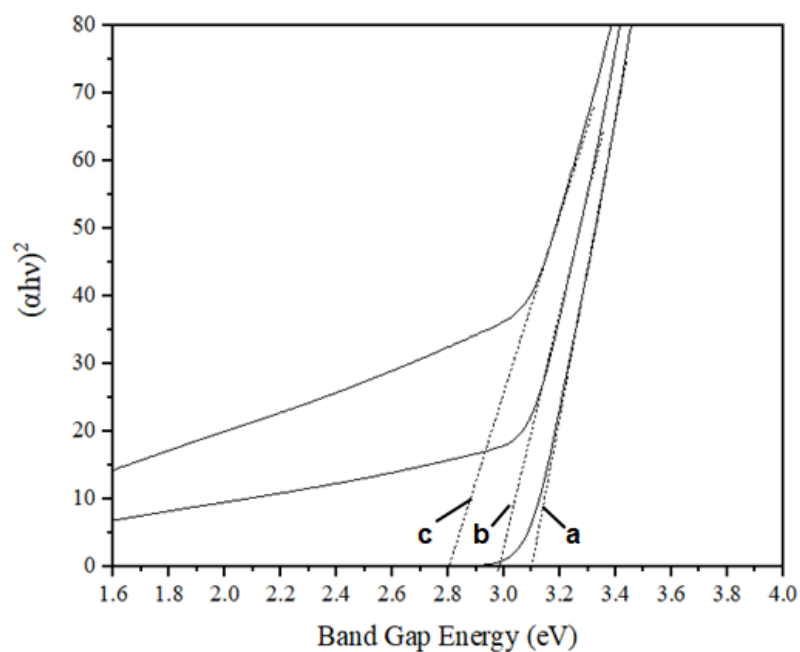


Figure 5.25 Tauc plot of the band gap energy derived from UV-Vis absorption spectra of (a) T400-5, (b) BT400-5-0.5 and (c) BT400-5-1

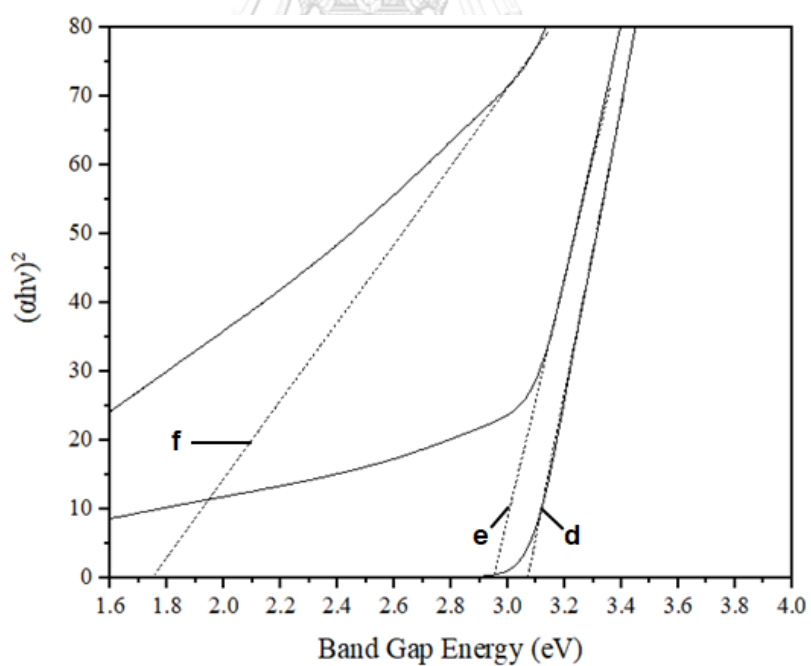


Figure 5.26 Tauc plot of the band gap energy derived from UV-Vis absorption spectra of (d) T400-10, (e) BT400-10-0.5 and (f) BT400-10-1

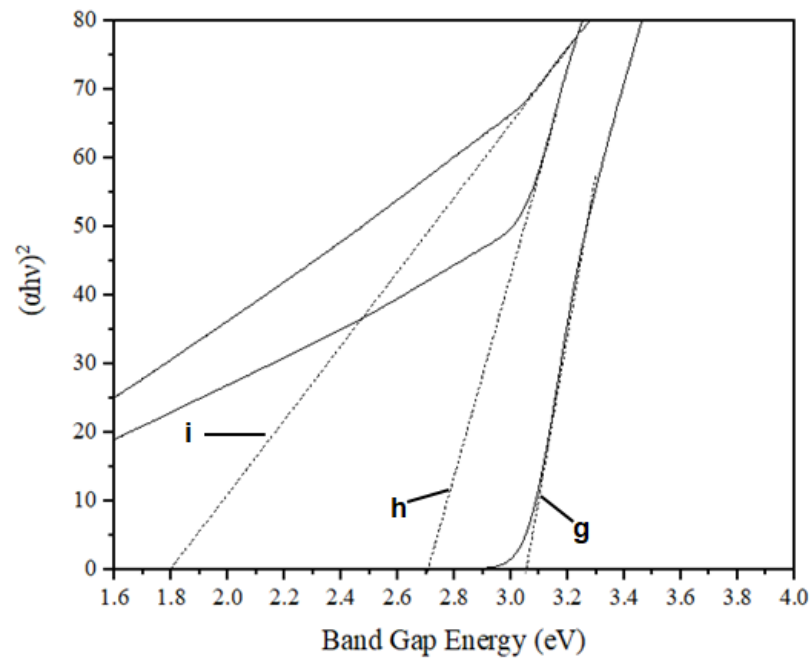


Figure 5.27 Tauc plot of the band gap energy derived from UV-Vis absorption spectra of (g) T500-5, (h) BT500-5-0.5 and (i) BT500-5-1

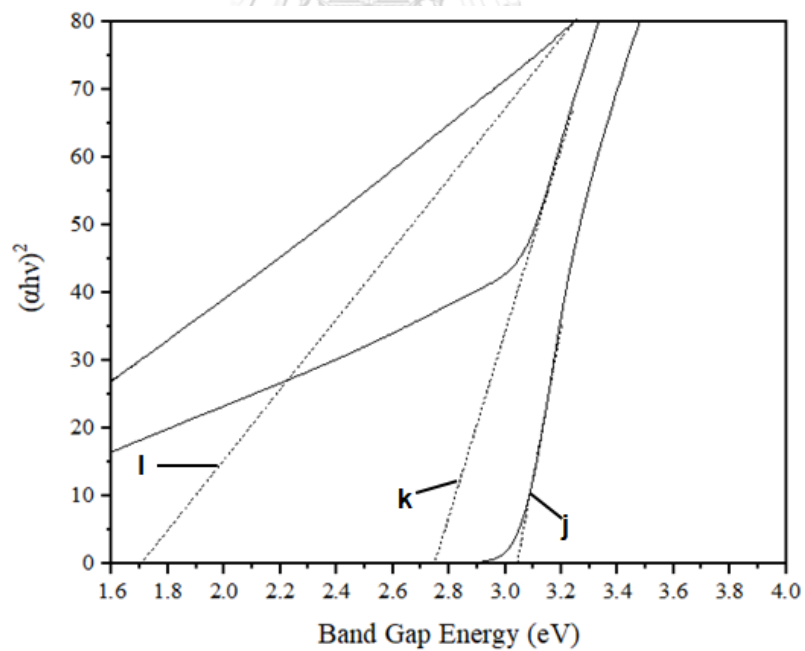


Figure 5.28 Tauc plot of the band gap energy derived from UV-Vis absorption spectra of (j) T500-10, (k) BT500-10-0.5 and (l) BT500-10-1

Table 5.12 The comparison of the band gap energy from UV-Vis absorption spectra of titanium dioxide and black titanium dioxide catalysts that were synthesized at various conditions.

Samples	Band Gap Energy (eV)
a) T400-5	3.10
b) BT400-5-0.5	2.98
c) BT400-5-1	2.80
d)T400-10	3.07
e) BT400-10-0.5	2.95
f) BT400-10-1	1.75
g)T500-5	3.05
h) BT500-5-0.5	2.70
i) BT500-5-1	1.80
j)T500-10	3.03
k) BT500-10-0.5	2.75
l) BT500-10-1	1.70

5.1.6 Fourier transform infrared spectroscopy (FTIR) analysis

The FTIR spectra of white TiO₂ and black TiO₂ were obtained by FTIR machine in transmittance mode in the range of wavenumber from 4000 to 500 cm⁻¹. All catalysts were classified into four conditions including 400 °C 5 hours, 400 °C 10 hours, 500 °C 5 hours, and 500 °C 10 hours. The spectra are shown in Figures 5.29 – 5.32. Every spectrum exhibited the broad peak around 611.9 – 629.1 cm⁻¹, which was assigned to the Ti-O-Ti stretching mode or Ti-O bonds in TiO₂ lattice [62-63]. The peaks around 2360.9 – 2361.9 cm⁻¹ corresponded to the residual alkoxide group that originated from titanium tetraisopropoxide (TTIP) precursor for white TiO₂. The alkoxide was removed at a calcination temperature between 400 °C and 500 °C. These peaks could be associated with chemical interaction of active hydrogen and Ti-O bonds in black TiO₂ [63].

The peaks at the wavenumber around 3201.2 -3413.7 cm⁻¹ and 1607.6 – 1648.2 cm⁻¹ were attributed to the O-H stretching and bending in TiO₂, respectively. The peak intensities of black TiO₂ at 3201.2 – 3413.7 cm⁻¹ grew smaller gradually as NaBH₄ reduction duration increased. This suggested that continuous reduction process eliminated more oxygen atoms when active hydrogen formed Ti-H bond at the surface to a lattice of TiO₂, bringing about the formation of the surface disorders. While the peak intensities at 1607.6 – 1648.2 cm⁻¹ of both white TiO₂ to black TiO₂ were similar, suggesting that the internal hydroxyl groups were still well preserved [63-65].

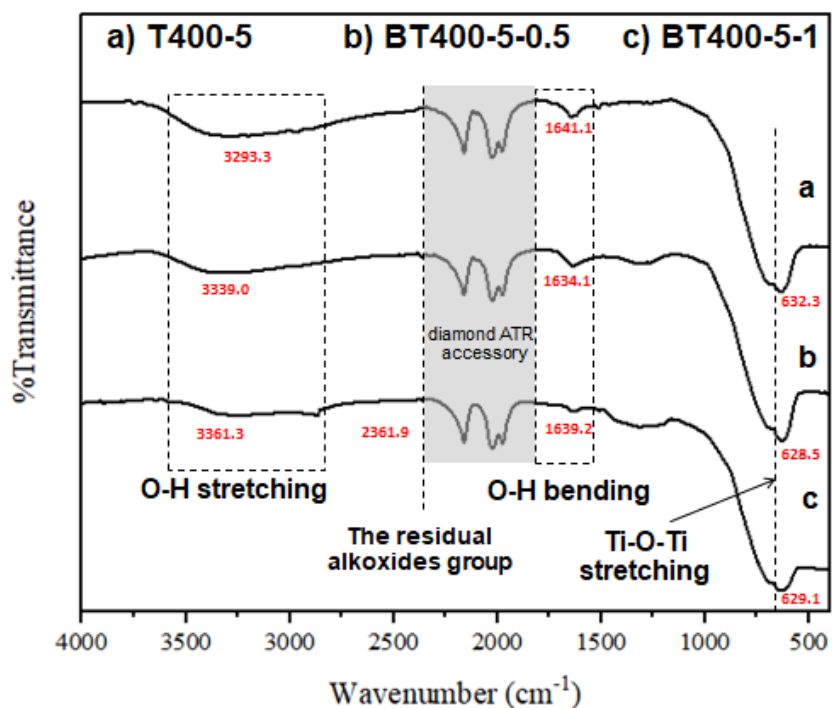


Figure 5.29 FTIR spectra of (a) T400-5, (b) BT400-5-0.5 and (c) BT400-5-1 with the wavenumber from 4000 to 500 cm^{-1}

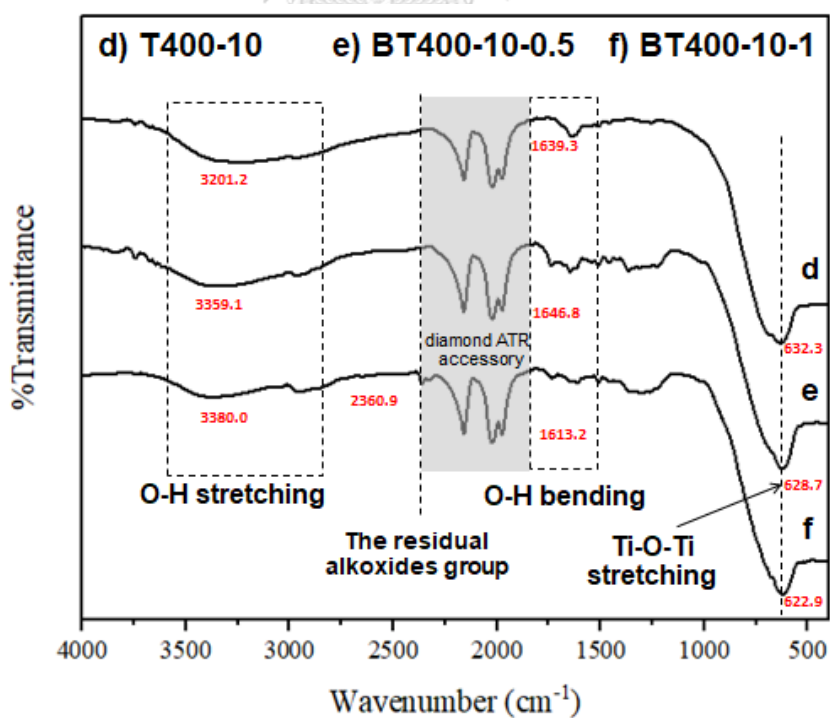


Figure 5.30 FTIR spectra of (d) T400-10, (e) BT400-10-0.5 and (f) BT400-10-1 with the wavenumber from 4000 to 500 cm^{-1}

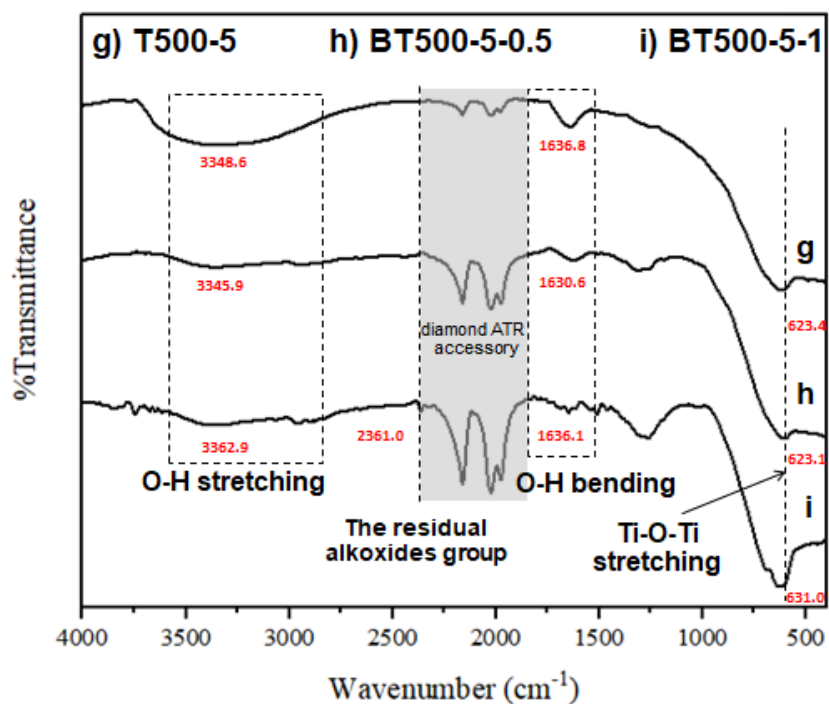


Figure 5.31 FTIR spectra of (g) T500-5, (h) BT500-5-0.5 and (i) BT500-5-1 with the wavenumber from 4000 to 500 cm^{-1}

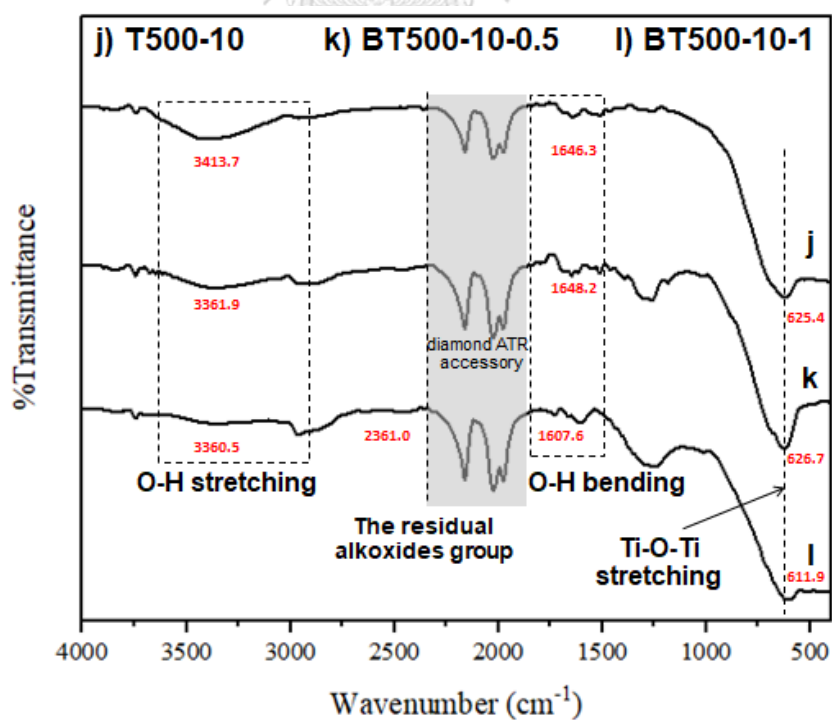


Figure 5.32 FTIR spectra of (j) T500-10, (k) BT500-10-0.5 and (l) BT500-10-1 with the wavenumber from 4000 to 500 cm^{-1}

5.2 Photocatalytic activity

The photocatalytic degradation of methyl orange was chosen as a model reaction to measure the photocatalytic activities of white TiO₂ and black TiO₂ under UV and visible light irradiations. An aqueous solution of methyl orange was stirred in the dark for one hour to acquire the adsorption equilibrium of the dye. After that, the mixture was exposed to either UV or visible light irradiations for 180 minutes. The concentration of methyl orange was determined using UV-visible spectrophotometer at $\lambda_{\max} = 464 \text{ nm}$.

There are many factors that can affect the photocatalytic activity such as the initial concentration or pH of the solution, the catalyst amount or dosage, temperature, the adsorption nature, and the nature of photocatalyst [17,20]. In our experiments, the photocatalytic degradation of methyl orange was conducted at a room temperature. The initial concentration of methyl orange solution was 10 ppm and the pH of the solution was approximately 4.4 (diluted with distilled water). And the catalyst dosage was 1.0 g/l. The values of the initial concentrations and the catalyst dosage were chosen from survey of literatures [66-67].

The experimental results in this part comprised the photocatalytic degradation of methyl orange under UV light and visible light irradiations, which included or excluded the adsorption, along with their kinetic curves.

The photocatalytic degradation of methyl orange with adsorption began monitoring the reduction of methyl orange when the catalyst was charged to the reactor. From the previous studies, the adsorption time needed to reach adsorption equilibrium for white TiO₂ and black TiO₂ were 60 and 30 minutes, respectively [37, 40, 47, 53, 68-69]. The studies were conducted in the dark to ensure the adsorption-desorption equilibrium between the dye and the surface of the photocatalyst. So, the adsorption time of 60 minutes was chosen for all our experiments.

5.2.1 The photocatalytic degradation of methyl orange under UV light irradiation

5.2.1.1 The photocatalytic degradation of methyl orange that included adsorption

Figures 5.33-5.36 showed the reduction in methyl orange concentration from the photocatalytic degradation of methyl orange and adsorption under UV irradiation. The removal of methyl orange over TiO_2 catalysts that were calcined at $400\text{ }^\circ\text{C}$ are presented in Table 5.13.

From Figure 5.33, the conversion from photolysis of methyl orange under UV irradiation was 4.69% (see Table 5.13). Methyl orange was difficult to undergo photolysis since it possessed one or more azo groups ($-\text{N}=\text{N}-$), resulting in strong resistance to degradation [28]. Black TiO_2 exhibited higher photocatalytic activity than white TiO_2 did. Furthermore, when the amount of reducing agent used was increased, the photocatalytic activity was more enhanced.

The order of increasing photocatalytic activities of the catalysts that were calcined at $400\text{ }^\circ\text{C}$ under UV irradiation was T400-10, T400-5, BT400-5-0.5, BT400-10-0.5, BT400-5-1, and BT400-10-1, respectively. These results had the same order with increasing amount of $\text{Ti}^{3+} / \text{Ti}^{4+}$ peak area ratio and oxygen vacancies (see Tables 5.4-5.7) and decreasing photoluminescence signals (see Figure 5.23). This indicated that these catalysts had more electron traps to separate the electron-hole pairs during photocatalytic process. Also, they had great absorption in UV region (see Figure 5.24) and exhibited high photocatalytic activities under UV light since their band gap energies were less than the photon energy of UV light source.

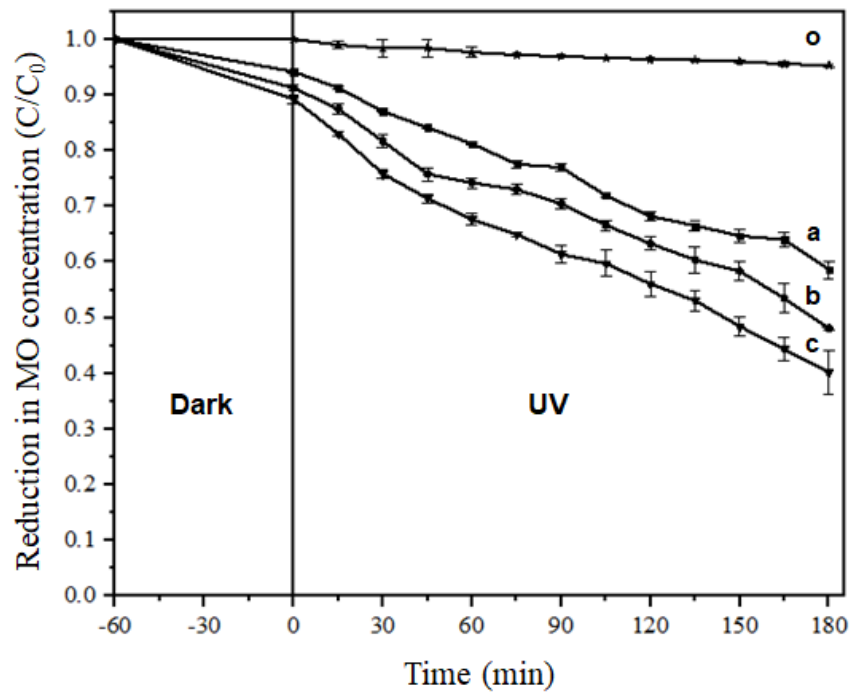


Figure 5.33 Photocatalytic degradation of methyl orange that included adsorption results under UV irradiation over (o) No catalyst, (a) T400-5, (b) BT400-5-0.5, and (c) BT400-5-1

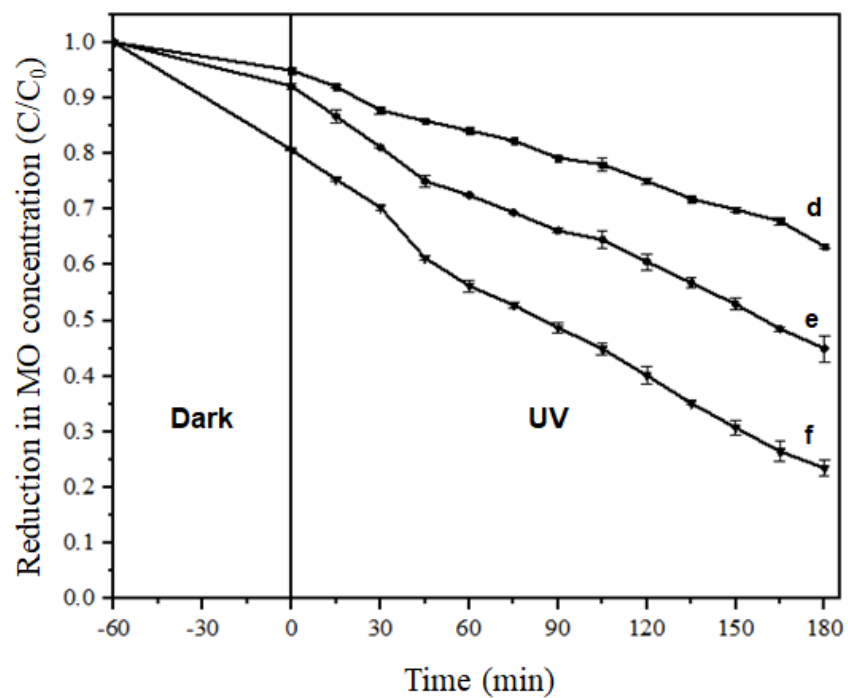


Figure 5.34 Photocatalytic degradation of methyl orange that included adsorption results under UV irradiation over (d) T400-10, (e) BT400-10-0.5, and (f) BT400-10-1

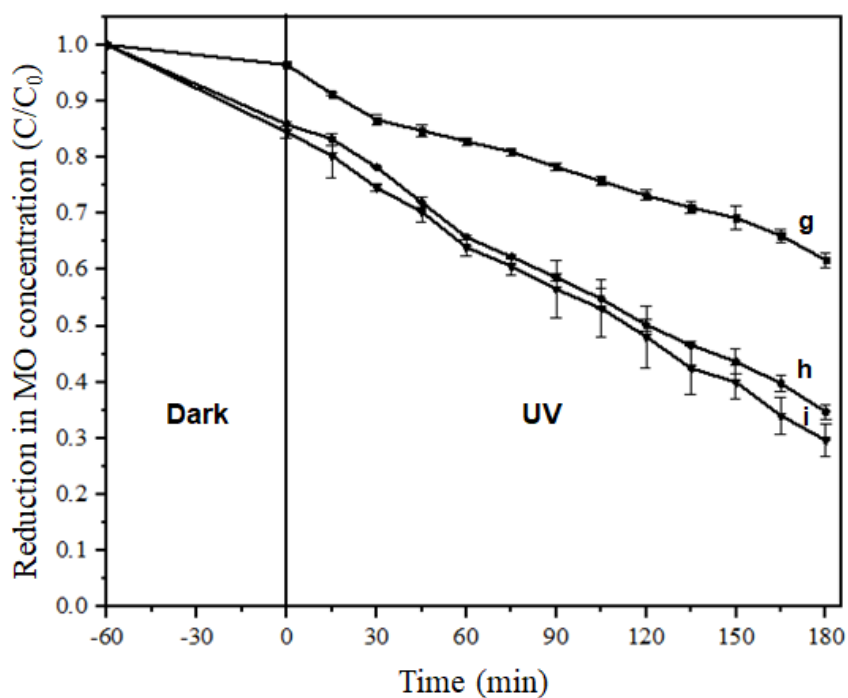


Figure 5.35 Photocatalytic degradation of methyl orange that included adsorption results under UV irradiation over (g) T500-5, (h) BT500-5-0.5 and (i) BT500-5-1

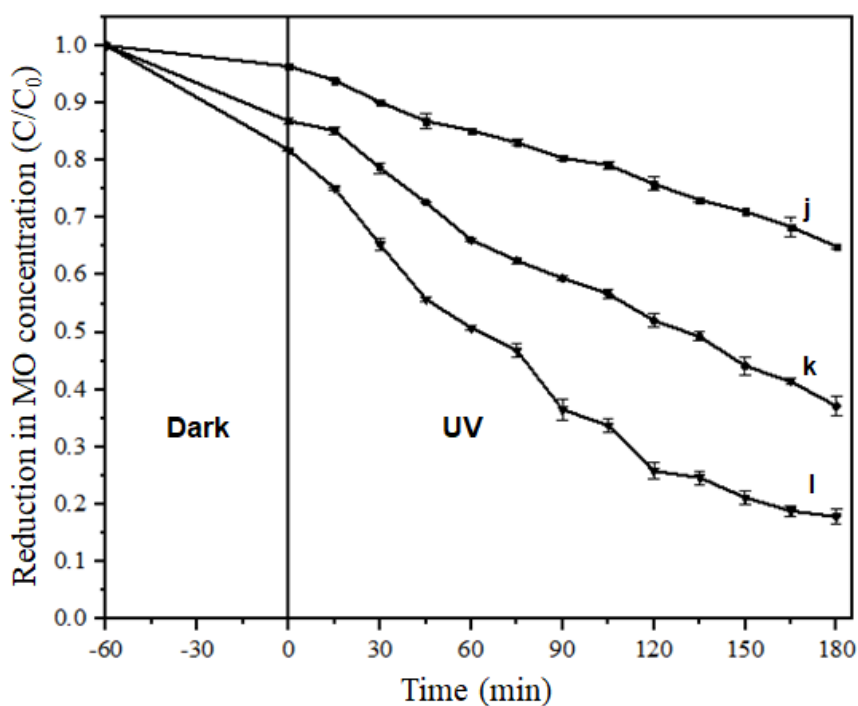


Figure 5.36 Photocatalytic degradation of methyl orange that included adsorption results under UV irradiation over (j) T500-10, (k) BT500-10-0.5 and (l) BT500-10-1

Table 5.13 The removal of methyl orange from photocatalytic degradation and adsorption under UV light irradiation over white TiO₂ and black TiO₂, which were calcined at 400 °C.

Samples	Removal after 4 h (%)
o) No catalyst	4.69
a) T400-5	41.39
b) BT400-5-0.5	51.89
c) BT400-5-1	59.79
d) T400-10	36.70
e) BT400-10-0.5	55.01
f) BT400-10-1	76.50

Figures 5.35- 5.36 presented the removal of methyl orange from photocatalytic degradation and adsorption under UV irradiation over white and black TiO₂ catalysts that were calcined at 500 °C. From Table 5.13-5.14, when the amount of reducing agent on white TiO₂ used to synthesize black TiO₂ increased, the photocatalytic activity became greater than white TiO₂ that was calcined at the same conditions. Also, almost all black TiO₂ catalysts that were calcined at 500 °C exhibited greater photocatalytic activities than that of black TiO₂ that were calcined at 400 °C because they contained greater amount surface defects or oxygen vacancies, which acted as the charge carrier traps as well as adsorption sites. These were confirmed by X-ray photoelectron spectra (XPS) results (see in Table 5.4 – 5.11).

Since the photocatalytic performance depended on the efficient electron separation of charge carriers on the surface of titanium dioxide, a slower recombination rate of electron-hole pairs led to higher photocatalytic activity [40]. Because of this, the catalyst with high photocatalytic activity exhibited smaller photoluminescence (PL) signal (see Figures 5.19 – 5.23). These results also agreed with the results from the measurement of X-ray photoelectron (XPS), and UV-vis spectroscopy. The order of increasing photocatalytic activities of the catalysts that calcined at 500 °C under UV irradiation was T500-10, T500-5, BT500-10-0.5, BT500-5-0.5, BT500-5-1, and BT500-10-1, respectively. These were same as the order of

increasing amount of Ti^{3+} / Ti^{4+} peak area ratio and oxygen vacancies (in Table 5.8-5.11). Also, the band gap energies of almost all black TiO_2 catalysts that were calcined at 500 °C were less than that of black TiO_2 that were calcined at 400 °C, resulting in higher photocatalytic activities under UV irradiation since the photon energy of UV light source was more than their band gap energies which can easily excite electrons to higher energy levels [19].

In the absence of light irradiation, the reduction in methyl orange concentration over black TiO_2 was greater than that over white TiO_2 because black TiO_2 possessed a larger amount of surface defect, which acted as the adsorption sites and also adsorbed the organic dye molecule efficiently [38].

Among all the catalysts, BT500-10-1 exhibited the largest photocatalytic activity at 82.17% under UV light irradiation (see Table 5.14) because it was synthesized by using the highest calcination temperature, time, and molar ratio of reducing agent, thereby creating the largest amount of surface defect. Consequently, the defects promoted the charge transfer to the surface of the catalyst and facilitated the efficient separation of electrons and holes during the photocatalytic process [38,40].

Table 5.14 The removal of methyl orange from photocatalytic degradation and adsorption under UV light irradiation over white TiO_2 and black TiO_2 , which were calcined at 500 °C.

Samples	Removal after 4 h (%)
g) T500-5	38.29
h) BT500-5-0.5	65.26
i) BT500-5-1	70.37
j) T500-10	35.03
k) BT500-10-0.5	62.85
l) BT500-10-1	82.17

5.2.1.2 The photocatalytic degradation of methyl orange, excluding the adsorption and the corresponding kinetics curves

Figure 5.37-5.44 showed the results of photocatalytic conversion from the photocatalytic degradation of methyl orange under UV irradiation, excluding the adsorption and the kinetics curves that associated with these data.

The conversions of methyl orange degradation over all TiO₂ catalysts under UV irradiation were listed in Tables 5.15 – 5.16. The curves followed the same trends as those of photocatalysis and adsorption (see Tables 5.13 – 5.14). The apparent first-order reaction rate constants (k , min⁻¹) of the catalysts were calculated from a slope of a pseudo first-order plot by using equation 4.2; $\ln(C_t/C_0) = -kt$.

BT500-10-1 catalyst had the highest reaction rate constant (k) of methyl orange degradation under UV irradiation at 8.75×10^{-3} min⁻¹. This catalyst exhibited the best photocatalytic activity due to the largest amount of surface defects present in the catalyst.

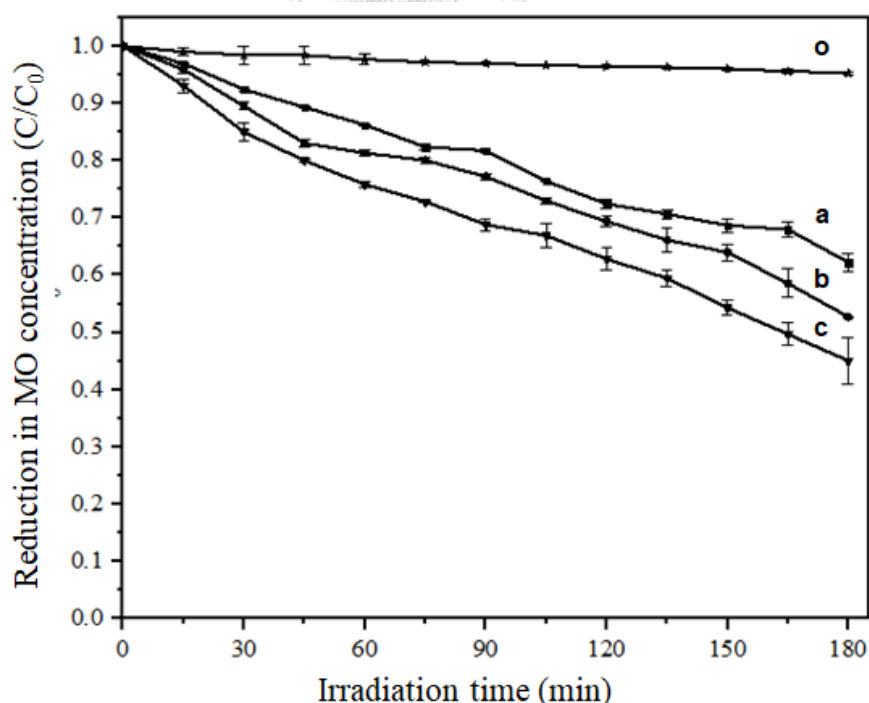


Figure 5.37 Photocatalytic degradation of methyl orange results under UV irradiation over (o) No catalyst, (a) T400-5, (b) BT400-5-0.5 and (c) BT400-5-1

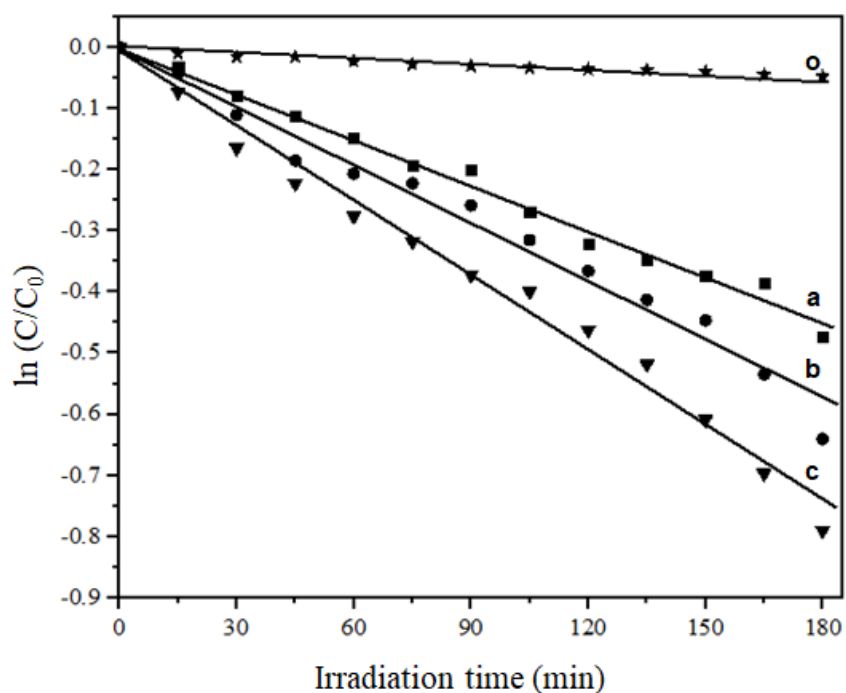


Figure 5.38 Pseudo first-order plots for the photocatalytic degradation of methyl orange under UV irradiation over (o) No catalyst, (a) T400-5, (b) BT400-5-0.5, and (c) BT400-5-1

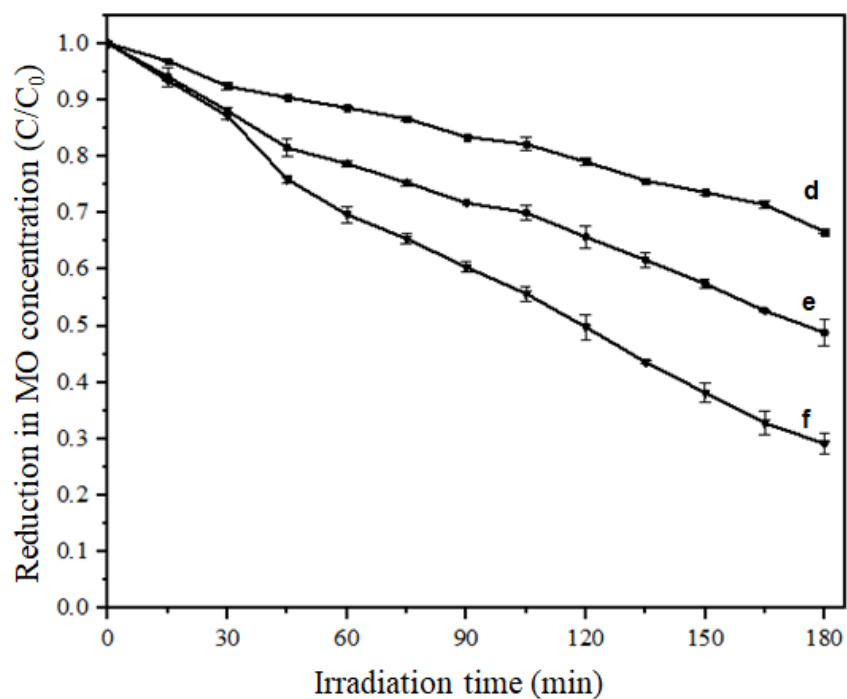


Figure 5.39 Photocatalytic degradation of methyl orange results under UV irradiation over (d) T400-10, (e) BT400-10-0.5, and (f) BT400-10-1

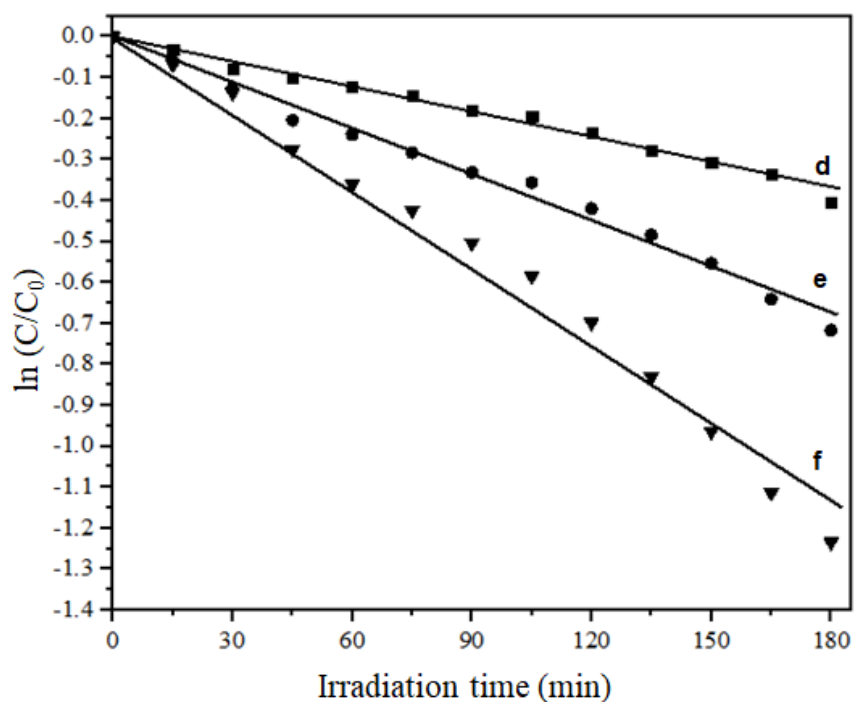


Figure 5.40 Pseudo first-order plots for the photocatalytic degradation of methyl orange under UV irradiation over (d) T400-10, (e) BT400-10-0.5, and (f) BT400-10-1

Table 5.15 The methyl orange conversion, pseudo-first order rate constant, and coefficient of determination (R^2) for photocatalytic degradation under UV light irradiation over white TiO_2 and black TiO_2 , which were calcined at 400 °C.

Samples	Conversion after 3 h (%) under UV	From Pseudo first-order plots	
		k (min^{-1})	R^2
o) No catalyst	4.69	2.90×10^{-4}	0.9031
a) T400-5	37.77	2.51×10^{-3}	0.9905
b) BT400-5-0.5	47.28	3.20×10^{-3}	0.9772
c) BT400-5-1	54.95	4.14×10^{-3}	0.9846
d) T400-10	33.34	2.07×10^{-3}	0.9872
e) BT400-10-0.5	51.18	3.76×10^{-3}	0.9880
f) BT400-10-1	70.86	6.32×10^{-3}	0.9813

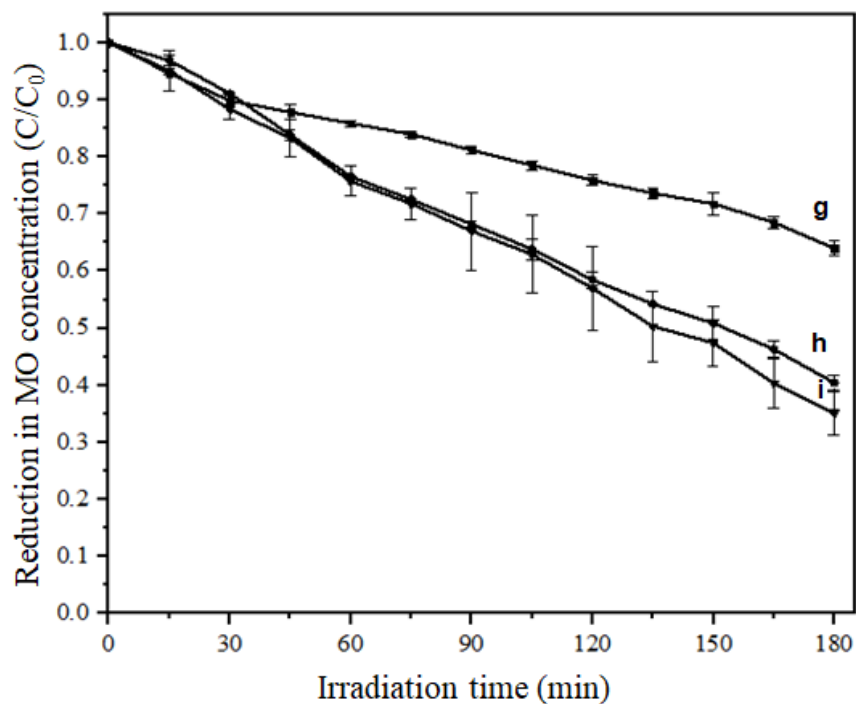


Figure 5.41 Photocatalytic degradation of methyl orange results under UV irradiation over (g) T500-5, (h) BT500-5-0.5, and (i) BT500-5-1

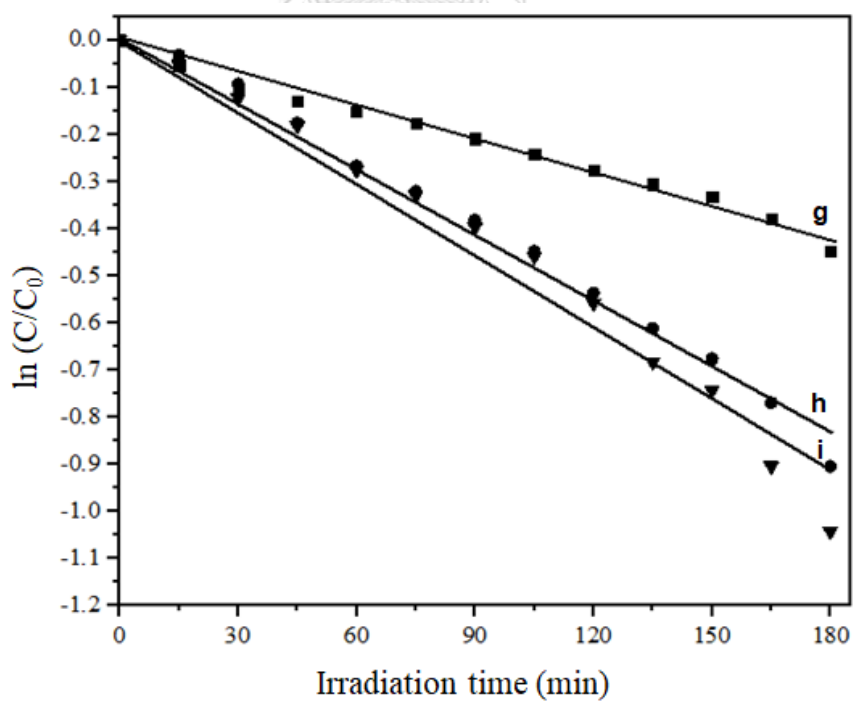


Figure 5.42 Pseudo first-order plots for the photocatalytic degradation of methyl orange under UV irradiation over (g) T500-5, (h) BT500-5-0.5, and (i) BT500-5-1

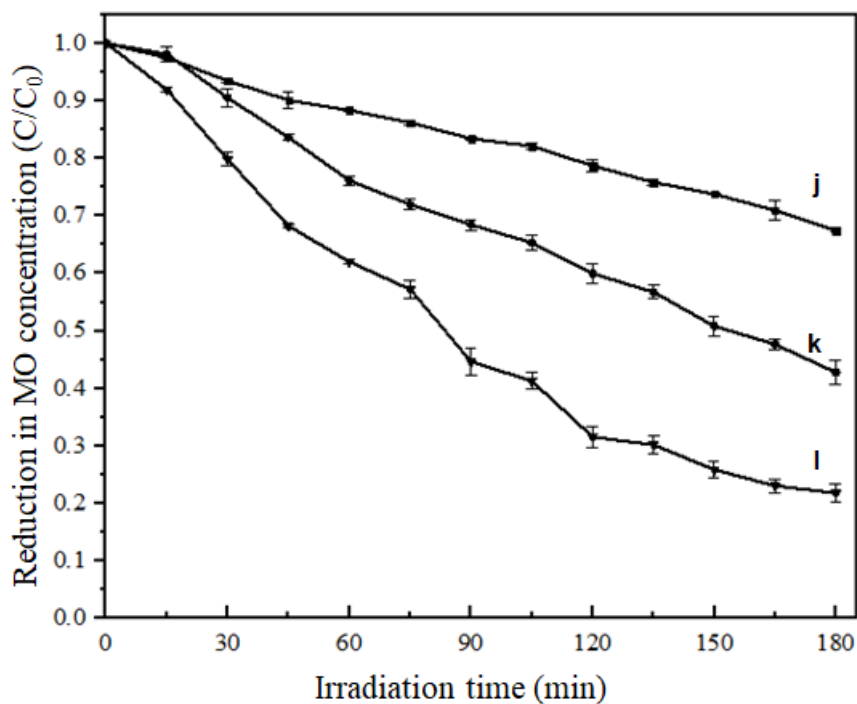


Figure 5.43 Photocatalytic degradation of methyl orange results under UV irradiation over (j) T500-10, (k) BT500-10-0.5, and (l) BT500-10-1

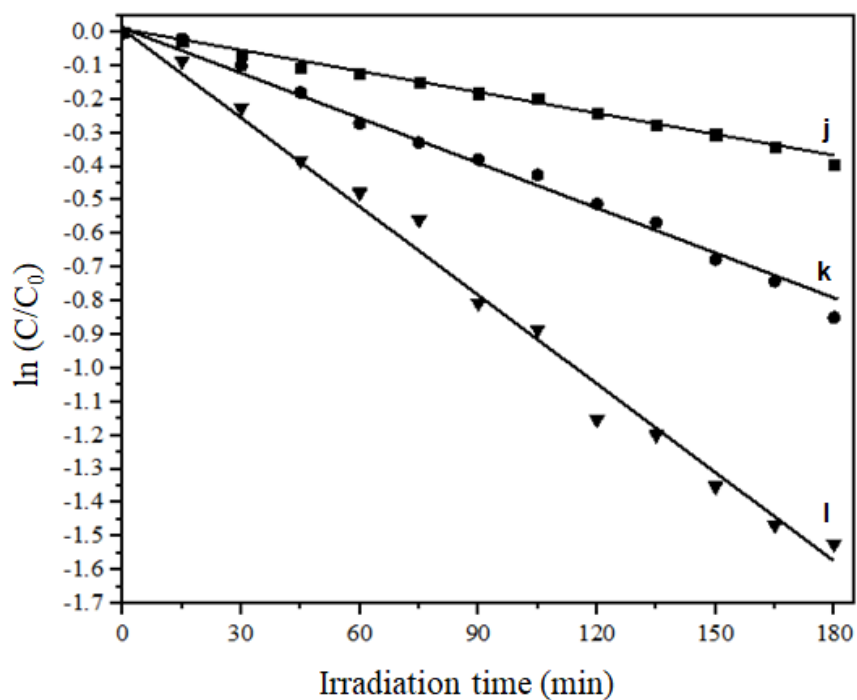


Figure 5.44 Pseudo first-order plots for the photocatalytic degradation of methyl orange under UV irradiation over (j) T500-10, (k) BT500-10-0.5, and (l) BT500-10-1

Table 5.16 The methyl orange conversion, pseudo-first order rate constant, and coefficient of determination (R^2) for photocatalytic degradation under UV light irradiation over whiteTiO₂ and black TiO₂, which were calcined at 500 °C.

Samples	Conversion after 3 h (%) under UV	From Pseudo first-order plots	
		k (min ⁻¹)	R ²
g) T500-5	36.03	2.35×10^{-3}	0.9822
h) BT500-5-0.5	59.56	4.59×10^{-3}	0.9863
i) BT500-5-1	64.89	5.10×10^{-3}	0.9692
j) T500-10	32.59	2.06×10^{-3}	0.9930
k) BT500-10-0.5	57.22	4.41×10^{-3}	0.9889
l) BT500-10-1	78.19	8.75×10^{-3}	0.9903

5.2.2 The photocatalytic degradation of methyl orange under visible light irradiation

5.2.2.1 The photocatalytic degradation of methyl orange that included adsorption

Figures 5.45-5.48 showed the reduction in methyl orange concentration from the photocatalytic degradation of methyl orange and adsorption under visible light irradiation over white and black TiO₂ catalysts that were calcined at 400 or 500 °C. The removal of methyl orange over TiO₂ catalysts that were calcined at 400 °C and 500 °C are presented in Table 5.17-5.18.

From Figure 5.45, the conversion of photolysis of methyl orange under visible light irradiation was 2.58% (see Table 5.16), which was slightly different from under UV irradiation (see Table 5.13). This can imply that methyl orange dye has strong resistance to degradation [28]. From Table 5.17-5.18, when the amount of reducing agent on white TiO₂ used to synthesize black TiO₂ increased, the photocatalytic activity became greater than white TiO₂ that was calcined at the same conditions.

The order of increasing in photocatalytic activities of the catalysts that were calcined at 400 °C or 500 °C under visible light irradiation followed the same trends as the photocatalytic activities under UV irradiation. These results also agreed with the results from the measurement of X-ray photoelectron (XPS), photoluminescence (PL) and UV-vis spectroscopy. This indicated that the photocatalytic activities under visible light irradiation were more enhanced although they were less than that under UV irradiation since the photon energy of visible light was less than that of UV light. The narrow band gap energies of all black TiO₂ had beneficial effect on photocatalysis under visible light irradiation because their values approximated to the photon energy of visible light source, resulting in the photo-excitation of electrons can easily occur to higher energy levels during the photocatalytic process.

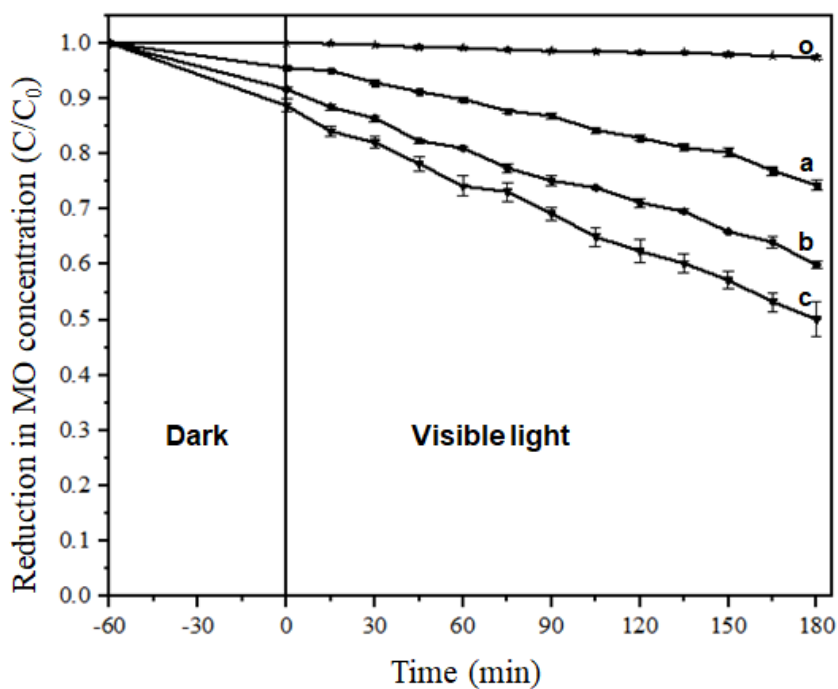


Figure 5.45 Photocatalytic degradation of methyl orange that included adsorption results under visible light irradiation over (o) No catalyst, (a) T400-5, (b) BT400-5-0.5, and (c) BT400-5-1

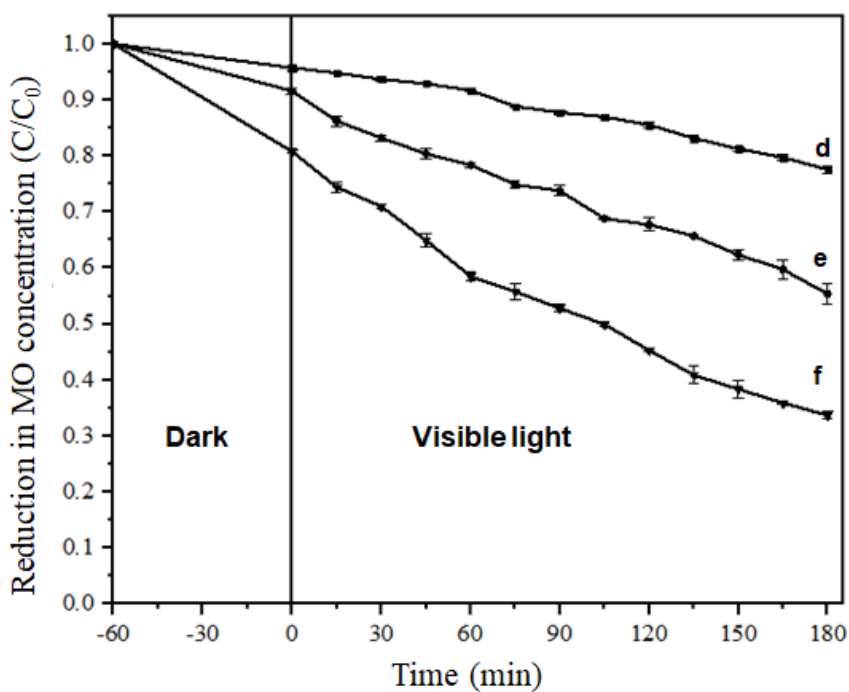


Figure 5.46 Photocatalytic degradation of methyl orange that included adsorption results under visible light irradiation over (d) T400-10, (e) BT400-10-0.5, and (f) BT400-10-1

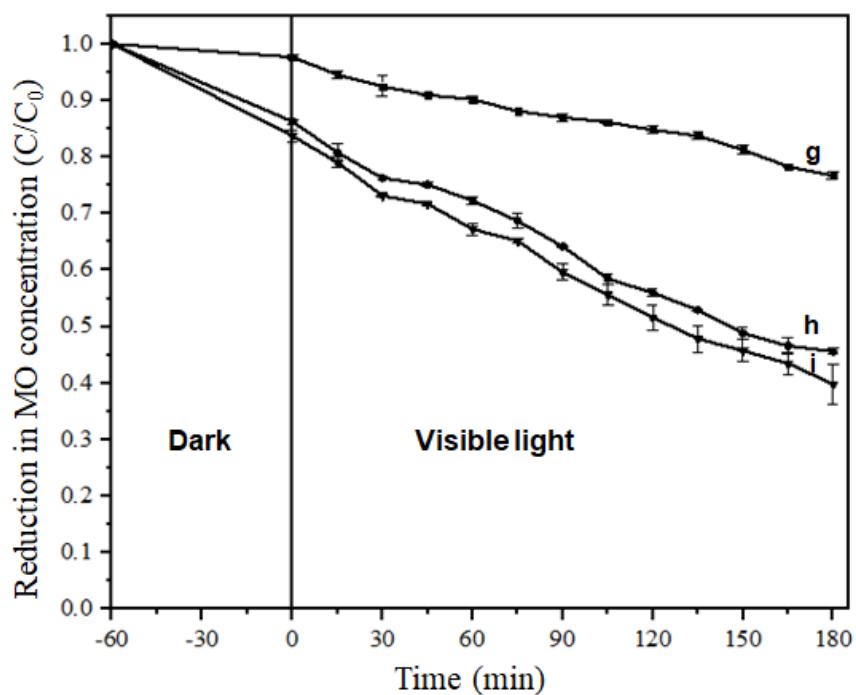


Figure 5.47 Photocatalytic degradation of methyl orange that included adsorption results under visible light irradiation over (g) T500-5, (h) BT500-5-0.5, and (i) BT500-5-1

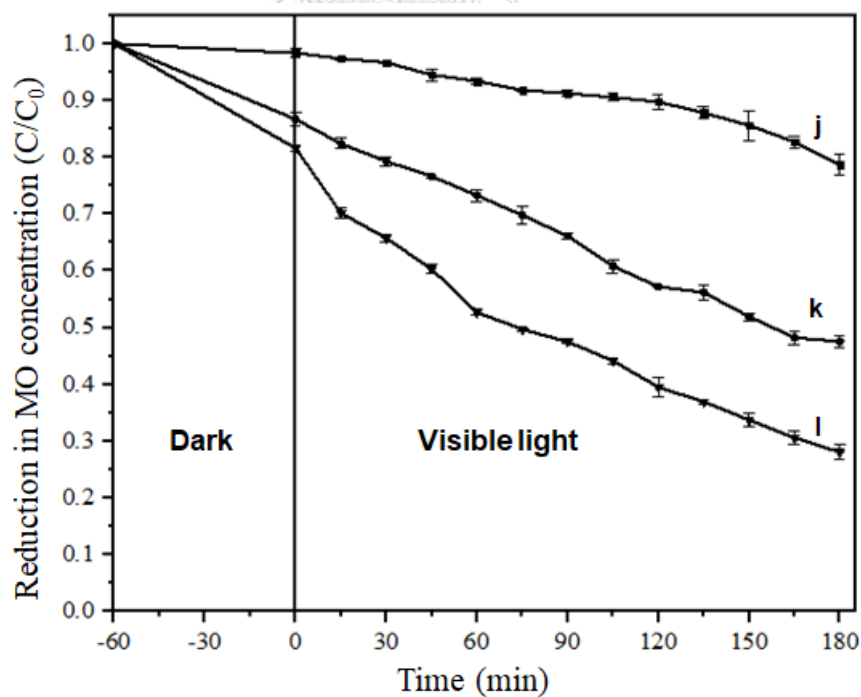


Figure 5.48 Photocatalytic degradation of methyl orange that included adsorption results under visible light irradiation over (j) T500-10, (k) BT500-10-0.5, and (l) BT500-10-1

Table 5.17 The removal of methyl orange from photocatalytic degradation and adsorption under visible light irradiation over white TiO₂ and black TiO₂ calcined at 400 °C

Samples	Removal after 4 h (%)
o) No catalyst	2.58
a) T400-5	25.72
b) BT400-5-0.5	40.14
c) BT400-5-1	49.89
d) T400-10	22.44
e) BT400-10-0.5	44.65
f) BT400-10-1	66.32

Among all the catalysts, BT500-10-1 exhibited the largest photocatalytic activity at 71.92% under visible light irradiation (see Table 5.18) which corresponded to the lowest photoluminescence signal (see Figure 5.23) and the maximum redshift in the UV-Vis absorption spectra (see Figure 5.24) due to the effect of the surface defect from NaBH₄ reduction process using the highest calcination temperature, time, and molar ratio of reducing agent.

Table 5.18 The removal of methyl orange from photocatalytic degradation and adsorption under visible light irradiation over white TiO₂ and black TiO₂ calcined at 500 °C

Samples	Removal after 4 h (%)
g) T500-5	23.38
h) BT500-5-0.5	54.40
i) BT500-5-1	60.20
j) T500-10	21.30
k) BT500-10-0.5	52.47
l) BT500-10-1	71.92

5.2.2.2 The photocatalytic degradation of methyl orange, excluding the adsorption and the corresponding kinetics curves

Figure 5.49-5.56 showed the results of photocatalytic conversion from the photocatalytic degradation of methyl orange under visible irradiation, excluding the adsorption and the kinetics curves that associated with these data.

The conversions of methyl orange degradation over all TiO₂ catalysts under visible irradiation were listed in Tables 5.19 – 5.20. The curve followed the same trends as those of photocatalysis and adsorption (see in Table 5.17 – 5.18). The apparent first-order reaction rate constants (k , min⁻¹) of the catalysts were calculated from a slope of a pseudo first-order plot by using equation 4.2; $\ln(C_t/C_0) = -kt$.

BT500-10-1 catalyst had the highest reaction rate constant (k) of methyl orange degradation under visible irradiation at 6.01×10^{-3} min⁻¹. This catalyst exhibited the best photocatalytic activity in both UV and visible light irradiation because it had the highest oxygen vacancies concentration which could induce a vacancy band of the electronic state below the conduction band edge, so the photo-excitation of electrons can easily occur and improved the photocatalytic degradation efficiency under visible light irradiation [51].

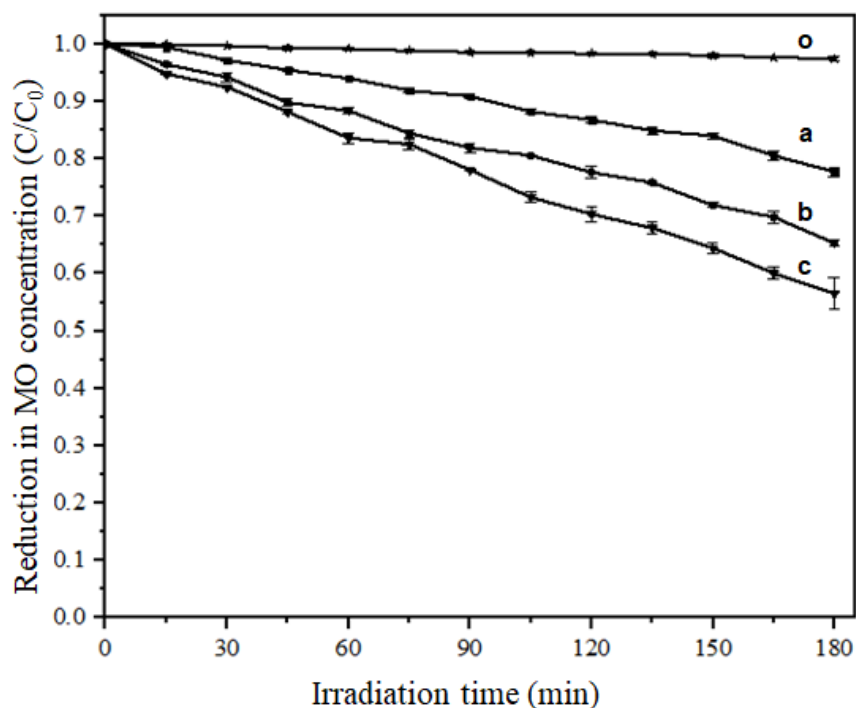


Figure 5.49 Photocatalytic degradation of methyl orange results under visible light irradiation over (o) No catalyst, (a) T400-5, (b) BT400-5-0.5, and (c) BT400-5-1

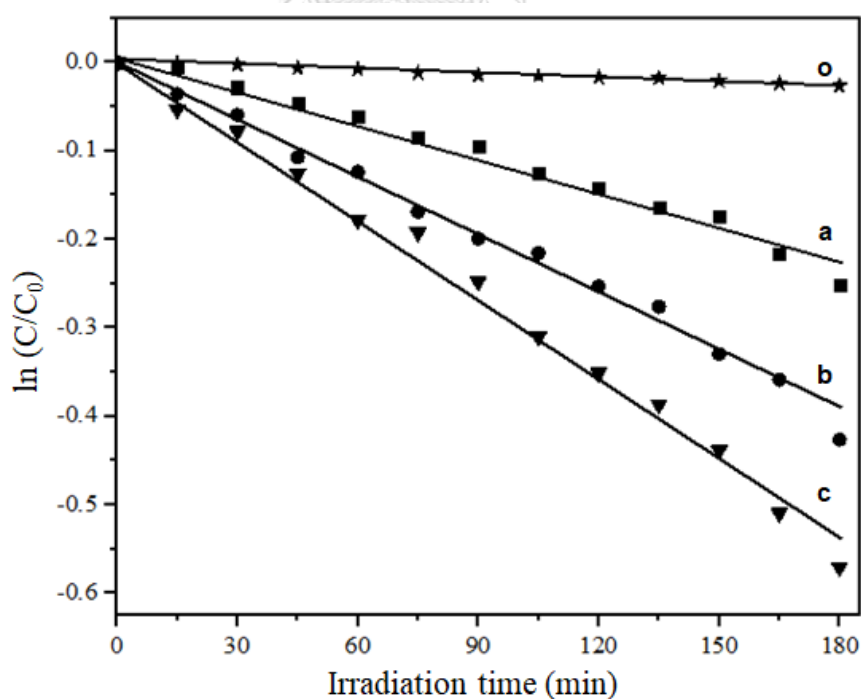


Figure 5.50 Pseudo first-order plots for the photocatalytic degradation of methyl orange under visible light irradiation over (o) No catalyst, (a) T400-5, (b) BT400-5-0.5, and (c) BT400-5-1

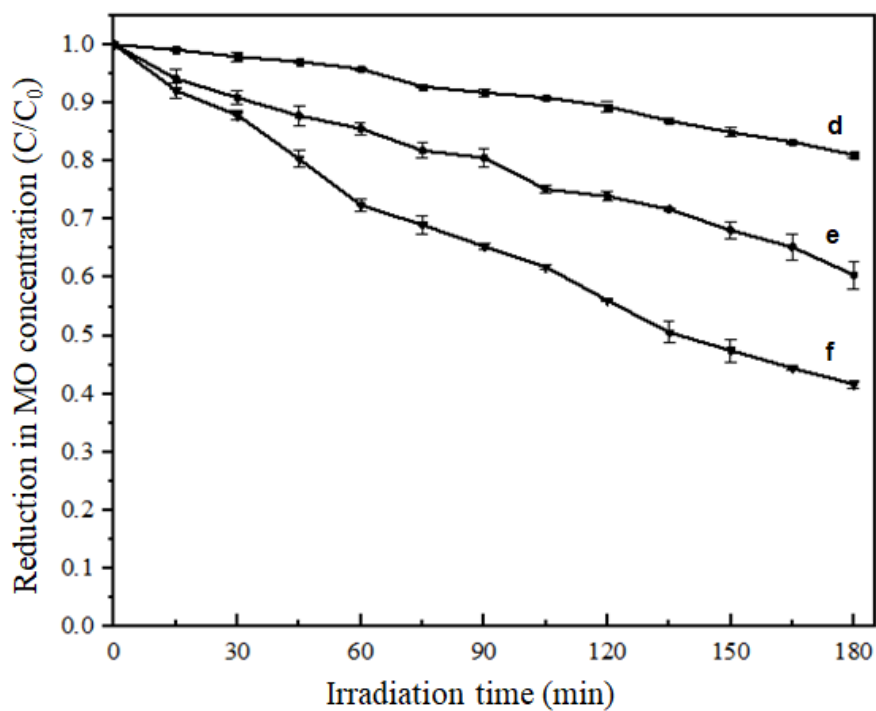


Figure 5.51 Photocatalytic degradation of methyl orange results under visible light irradiation over (d) T400-10 , (e) BT400-10-0.5, and (f) BT400-10-1

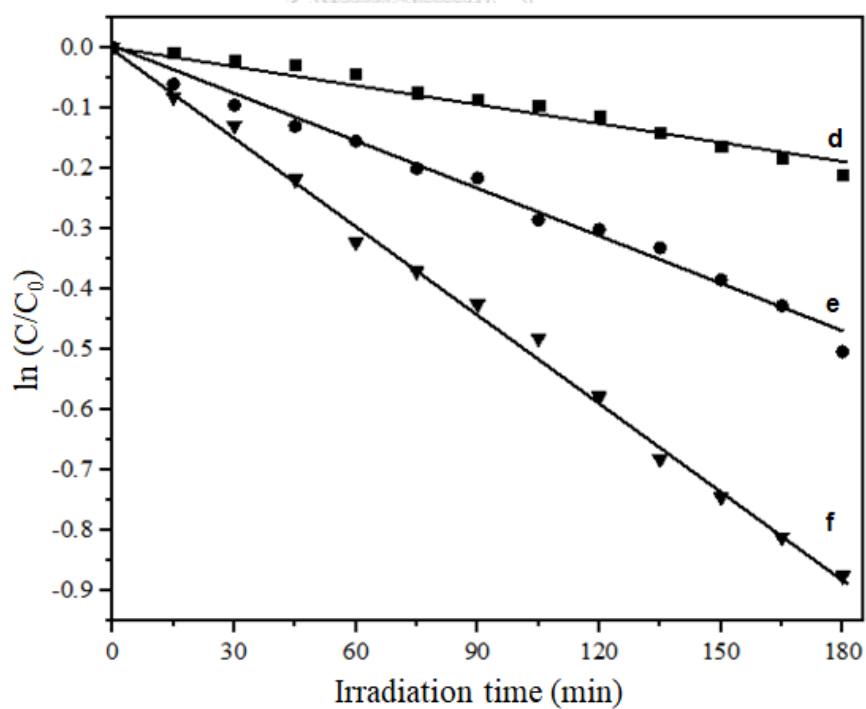


Figure 5.52 Pseudo first-order plots for the photocatalytic degradation of methyl orange under visible light irradiation over (d) T400-10, (e) BT400-10-0.5, and (f) BT400-10-1

Table 5.19 The methyl orange conversion, pseudo-first order rate constant, and coefficient of determination (R^2) for photocatalytic degradation under visible light irradiation over whiteTiO₂ and black TiO₂, which were calcined at 400 °C.

Samples	Conversion after 3 h (%) under visible light	From Pseudo first-order plots	
		k (min ⁻¹)	R ²
o) No catalyst	2.58	1.40×10^{-4}	0.9847
a) T400-5	22.26	1.24×10^{-3}	0.9736
b) BT400-5-0.5	34.72	2.19×10^{-3}	0.9906
c) BT400-5-1	43.52	2.98×10^{-3}	0.9910
d) T400-10	18.97	1.05×10^{-3}	0.9662
e) BT400-10-0.5	39.56	2.62×10^{-3}	0.9882
f) BT400-10-1	58.32	4.89×10^{-3}	0.9967

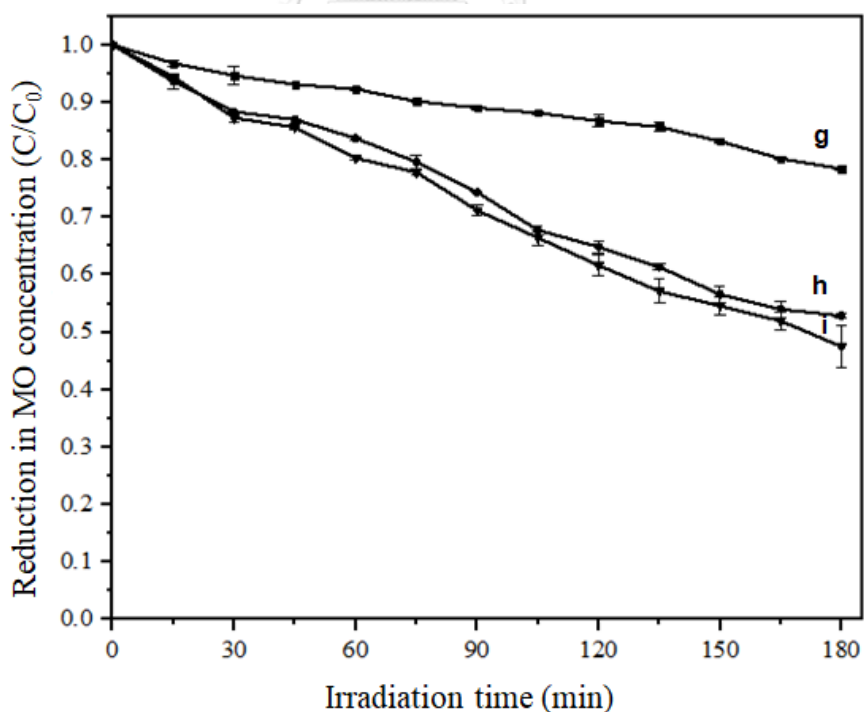


Figure 5.53 Photocatalytic degradation of methyl orange results under visible light irradiation over (g) T500-5, (h) BT500-5-0.5, and (i) BT500-5-1

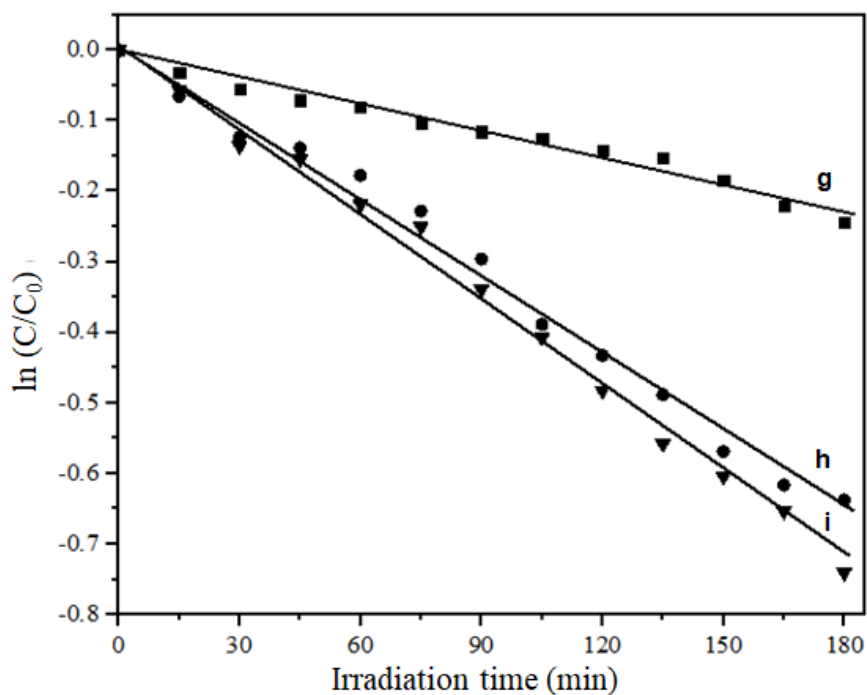


Figure 5.54 Pseudo first-order plots for the photocatalytic degradation of methyl orange under visible light irradiation over (g) T500-5, (h) BT500-5-0.5, and (i) BT500-5-1

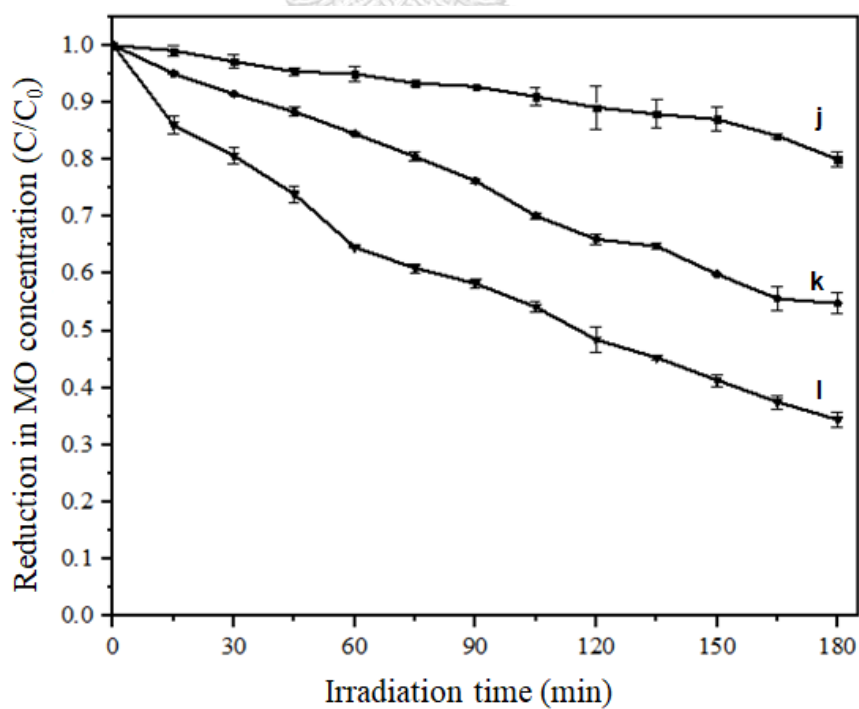


Figure 5.55 Photocatalytic degradation of methyl orange results under visible light irradiation over (j) T500-10, (k) BT500-10-0.5, and (l) BT500-10-1

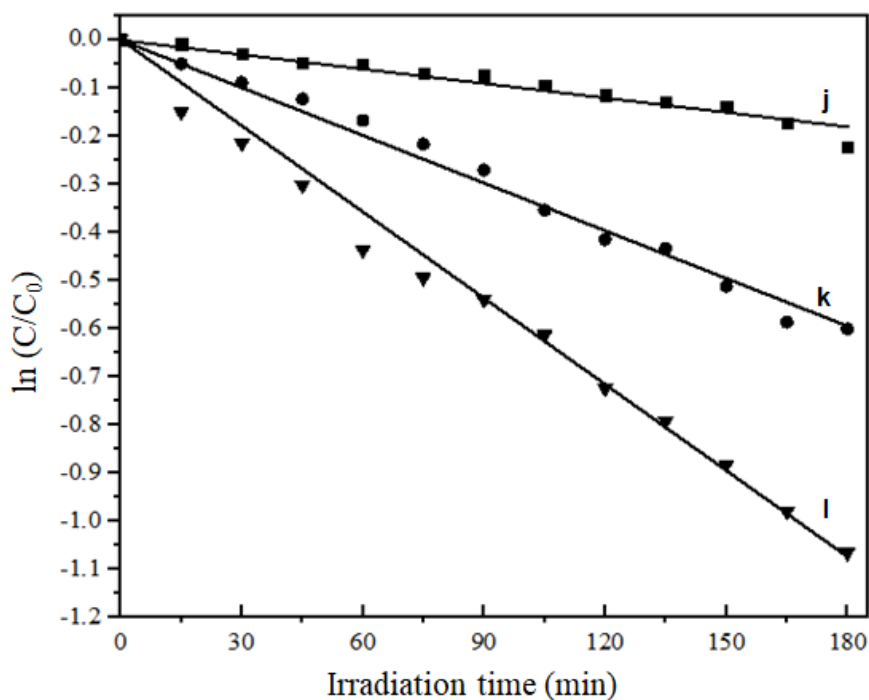


Figure 5.56 Pseudo first-order plots for the photocatalytic degradation of methyl orange under visible light irradiation over (j) T500-10, (k) BT500-10-0.5, and (l) BT500-10-1

Table 5.20 The methyl orange conversion, pseudo-first order rate constant, and coefficient of determination (R^2) for photocatalytic degradation under visible light irradiation over whiteTiO₂ and black TiO₂, which were calcined at 500 °C

Samples	Conversion after 3 h (%) under visible light	From Pseudo first-order plots	
		k (min ⁻¹)	R ²
g) T500-5	21.57	1.28 × 10 ⁻³	0.9742
h) BT500-5-0.5	47.16	3.60 × 10 ⁻³	0.9885
i) BT500-5-1	52.48	3.98 × 10 ⁻³	0.9926
j) T500-10	19.97	1.02 × 10 ⁻³	0.9506
k) BT500-10-0.5	45.17	3.33 × 10 ⁻³	0.9885
l) BT500-10-1	65.57	6.01 × 10 ⁻³	0.9885

5.3 Statistical Analysis

In this part, a 2x2x3 factorial experimental design was adopted to investigate the effects of catalyst preparation parameters on the conversion of methyl orange in the photocatalytic degradation under UV and visible light irradiations. The three factors examined were calcination temperature (factor A), calcination time (factor B), and the molar ratio of NaBH₄ to TiO₂ used during reduction process (factor C) Minitab Statistical Software (Minitab Release 16) was used to analyze the results. The program determined the significance of the main effects and their interactions using analysis of variance and assessed the validity of the statistical model using residual analysis.

In this study, a 2 x 2 x 3 factorial design with two replicates required 24 runs. The photocatalytic experiments were performed under UV and visible light irradiations so a total of 48 experiments were carried out.

5.3.1 The effects of catalyst preparation parameters on the removal of methyl orange in the photocatalytic degradation under UV light irradiation

In this study, a total of 24 photocatalytic degradation experiments under UV light irradiation were carried out. The results of the removal of methyl orange from photocatalytic degradation that included (I) and excluded (E) the adsorption by using all catalysts were shown in Table 5.21

Table 5.21 The removal of methyl orange from photocatalytic degradation under UV light irradiation over all TiO₂ catalysts from the 2 x 2 x 3 factorial design study.

Experimental Order (Observation Order)	Run	Parameters for catalyst preparation			Catalysts	% Removal of MO (3 h under UV)	
		A	B	C		(I)	(E)
1	1	400	5	0	T400-5 (I)	40.25	36.69
2	9	400	5	1	BT400-5-1 (I)	56.96	52.07
3	10	500	5	1	BT500-5-1 (I)	68.35	62.20
4	2	500	5	0	T500-5 (I)	37.35	35.11
5	13	400	5	0	T400-5 (II)	42.53	38.86
6	14	500	5	0	T500-5 (II)	39.23	36.94
7	21	400	5	1	BT400-5-1 (II)	62.61	57.84
8	22	500	5	1	BT500-5-1 (II)	72.39	67.58
9	5	400	5	0.5	BT400-5-0.5(I)	51.74	47.35
10	6	500	5	0.5	BT500-5-0.5 (I)	64.37	58.64
11	17	400	5	0.5	BT400-5-0.5 (II)	52.04	47.21
12	18	500	5	0.5	BT500-5-0.5 (II)	66.15	60.49
13	3	400	10	0	T400-10 (I)	36.53	33.17
14	4	500	10	0	T500-10 (I)	34.75	32.39
15	15	400	10	0	T400-10 (II)	36.86	33.50
16	16	500	10	0	T500-10 (II)	35.30	32.79
17	12	500	10	1	BT500-10-1 (I)	83.08	79.04
18	11	400	10	1	BT400-10-1 (I)	75.54	69.64
19	7	400	10	0.5	BT400-10-0.5 (I)	53.34	49.56
20	8	500	10	0.5	BT500-10-0.5 (I)	61.72	55.76
21	23	400	10	1	BT400-10-1 (II)	77.45	72.08
22	24	500	10	1	BT500-10-1 (II)	81.25	77.04
23	19	400	10	0.5	BT400-10-0.5 (II)	56.68	52.79
24	20	500	10	0.5	BT500-10-0.5 (II)	63.98	58.68

5.3.1.1 Analysis of variance (ANOVA)

Analysis of variance was employed to assess the significance of the main effects and their interactions. The result of the experimental data analysis by Minitab was displayed in Table 5.22-5.24

Table 5.22 The analysis of variance (ANOVA) of the removal of methyl orange from photocatalytic degradation and adsorption under UV light irradiation

Source	Degree of freedom	Adjusted Sum of Square	Adjusted Mean of Square	F-Value	P-Value	Status
Model	11	5629.76	511.80	146.39	0.000	Significant
Linear	4	5048.21	1262.05	360.99	0.000	Significant
A	1	178.16	178.16	50.96	0.000	Significant
B	1	75.30	75.30	21.54	0.001	Significant
C	2	4794.75	2397.37	685.72	0.000	Significant
2-Way Interactions	5	566.71	113.34	32.42	0.000	Significant
A*B	1	13.55	13.55	3.87	0.073	Not significant
A*C	2	190.26	95.13	27.21	0.000	Significant
B*C	2	362.90	181.45	51.90	0.000	Significant
3-Way Interactions	2	14.85	7.42	2.12	0.162	Not significant
A*B*C	2	14.85	7.42	2.12	0.162	Not significant
Error	12	41.95	3.50			
Total	23	5671.72				

Table 5.23 The analysis of variance (ANOVA) of the removal of methyl orange from photocatalytic degradation, excluding the adsorption under UV light irradiation

Source	Degree of freedom	Adjusted Sum of Square	Adjusted Mean of Square	F-Value	P-Value	Status
Model	11	4997.55	454.32	105.94	0.000	Significant
Linear	4	4468.97	1117.24	260.53	0.000	Significant
A	1	180.95	180.95	42.20	0.000	Significant
B	1	86.11	86.11	20.08	0.001	Significant
C	2	4201.91	2100.96	489.93	0.000	Significant
2-Way Interactions	5	515.45	103.09	24.04	0.000	Significant
A*B	1	10.64	10.64	2.48	0.141	Not significant
A*C	2	136.62	68.31	15.93	0.000	Significant
B*C	2	368.20	184.10	42.93	0.000	Significant
3-Way Interactions	2	13.13	6.56	1.53	0.256	Not significant
A*B*C	2	13.13	6.56	1.53	0.256	Not significant
Error	12	51.46	4.29			
Total	23	5049.01				

Table 5.24 The model summary from the analysis of variance (ANOVA) of the removal of methyl orange from photocatalytic degradation under UV light irradiation.

Including adsorption under UV light irradiation	
R-squared	99.26%
Adjusted R-squared	98.58%
Predicted R-squared	97.04%
Standard Deviation	1.86979
Regression equation	See Appendix H.1 (Table H.3)
Excluding adsorption under UV light irradiation	
R-squared	98.98%
Adjusted R-squared	98.05%
Predicted R-squared	95.92%
Standard Deviation	2.07082
Regression equation	See Appendix H.2 (Table H.4)

In Table 5.22-5.23 the statistical F-test was performed on the main effects and their interactions for the removal of methyl orange under UV light irradiation from photocatalytic degradation that included (I) and excluded (E) the adsorption at the significance level of $\alpha = 0.05$ as follows.

Hypotheses testing of the main factors

H_0 : Main effect does not influence the removal of methyl orange under UV light irradiation from photocatalytic degradation.

H_1 : Main effect influences the removal of methyl orange under UV light irradiation from photocatalytic degradation.

When considering the P-value of the main effect in Table 5.22-5.23, the main effects A, B, and C had P-value less than the significance level $\alpha = 0.05$ [6]. Therefore, calcination temperature, calcination time, and molar ratio of reducing agent had significant effects on the removal of methyl orange under UV light irradiation from photocatalytic degradation.

Hypotheses testing of the interaction of each factor

H₀: Interaction effect does not influence the removal of methyl orange under UV light irradiation from photocatalytic degradation.

H₁: Interaction effect influences the removal of methyl orange under UV light irradiation from photocatalytic degradation.

When considering the P-value of the interaction effect in Table 5.22-5.23, the following conclusions were drawn.

1) Interaction Effects **A*C** and **B*C** had a P-value less than the significance level $\alpha = 0.05$. Therefore, the interaction between calcination temperature and molar ratio reducing agent and the interaction between calcination time and molar ratio of reducing agent significantly affected the removal of methyl orange under UV light irradiation from photocatalytic degradation that included and excluded the adsorption.

2) Interaction Effects **A*B** and **A*B*C** had a P-value greater than the significance level $\alpha = 0.05$. Therefore, the interaction between calcination temperature and calcination time and the interaction between calcination temperature, calcination time and molar ratio of reducing agent did not significantly affect the removal of methyl orange under UV light irradiation from photocatalytic degradation that included and excluded the adsorption.

In addition, the effect of the main factors and their interactions on the removal of methyl orange under UV light irradiation from photocatalytic degradation that included and excluded the adsorption, which was assessed by the Pareto Chart

in Figure I.1 (a)-(b) (see Appendix I.1) which exhibited the absolute value of the effects. If the bar associated with any factor exceeded the value of the reference line (represented by a dashed line), such factor had a significant effect and was included in the model. From Figure I.1 (a)-(b) the insignificant factors were $A*B$ and $A*B*C$. This agreed with the result of analysis of variance (ANOVA) in Table 5.22-5.23.

5.3.1.2 Analysis of residuals

The data from the analysis of residuals as shown in Table 5.25-5.26, were assessed to check the validity of the error term from the results of the removal of methyl orange from photocatalytic degradation under UV light irradiation that included and excluded the adsorption.

1) Assessing the normality of data

The normal probability plots of residuals were shown as Figure I.2 (a) and Figure I.3 (a) (see Appendix I.2-I.3). This indicated that the data were arranged in a straight line manner and concluded that they had a normal distribution.

2) Assessing the independence of data

The plots of residuals versus the order of the data that were shown as Figure I.2 (b) and Figure I.3 (b) (see Appendix I.2-I.3). This indicated that the distribution of the residuals had no exact direction and concluded that the independence of the observation orders were acceptable.

3) Assessing the stability of variance of data

The plots of residuals versus fitted values that were shown as Figure I.2(c) and Figure I.3(c) (see Appendix I.2-I.3). This indicated that the distribution of residuals had no exact direction and concluded that the variance of this experimental data was relatively constant.

The plots of residuals versus the values of each level of factors A, B, and C were shown as Figures I.2 (d, e, and f) and Figures I.3 (d, e, and f) (see Appendix I.2-I.3). This indicated that the variance of this experimental data was relatively constant, especially residuals versus factor A.

Table 5.25 Fits and diagnostics for all observations of the removal from photocatalytic degradation and adsorption under UV light irradiation

Observation order	% Removal of MO after 4 h (3 h under UV)	Fitted values	Residuals
1	40.25	41.39	-1.14
2	56.96	59.78	-2.82
3	68.35	70.37	-2.02
4	37.35	38.29	-0.94
5	42.53	41.39	1.14
6	39.23	38.29	0.94
7	62.61	59.78	2.83
8	72.39	70.37	2.02
9	51.74	51.89	-0.15
10	64.37	65.26	-0.89
11	52.04	51.89	0.15
12	66.15	65.26	0.89
13	36.53	36.70	-0.17
14	34.75	35.03	-0.28
15	36.86	36.70	0.16
16	35.30	35.03	0.27
17	83.08	82.16	0.92
18	75.54	76.50	-0.96
19	53.34	55.01	-1.67
20	61.72	62.85	-1.13
21	77.45	76.50	0.95
22	81.25	82.16	-0.91
23	56.68	55.01	1.67
24	63.98	62.85	1.13

Table 5.26 Fits and diagnostics for all observations of the removal from photocatalytic degradation, excluding the adsorption under UV light irradiation

Observation order	% Removal of MO after 3 h under UV	Fitted values	Residuals
1	36.69	37.78	-1.09
2	52.07	54.96	-2.89
3	62.20	64.89	-2.69
4	35.11	36.03	-0.92
5	38.86	37.78	1.08
6	36.94	36.03	0.91
7	57.84	54.96	2.88
8	67.58	64.89	2.69
9	47.35	47.28	0.07
10	58.64	59.56	-0.92
11	47.21	47.28	-0.07
12	60.49	59.56	0.93
13	33.17	33.34	-0.17
14	32.39	32.59	-0.20
15	33.50	33.34	0.16
16	32.79	32.59	0.20
17	79.04	78.04	1.00
18	69.64	70.86	-1.22
19	49.56	51.17	-1.61
20	55.76	57.22	-1.46
21	72.08	70.86	1.22
22	77.04	78.04	-1.00
23	52.79	51.17	1.62
24	58.68	57.22	1.46

5.3.2 The effects of catalyst preparation parameters on the removal of methyl orange in the photocatalytic degradation under visible light irradiation

In this study, a total of 24 photocatalytic degradation experiments under visible light irradiation were carried out. The results of the removal of methyl orange from photocatalytic degradation that included (I) or excluded (E) the adsorption by using all catalysts were shown in Table 5.27

Table 5.27 The removal of methyl orange from photocatalytic degradation under visible light irradiation over all TiO₂ catalysts from the 2 x 2 x 3 factorial design study.

Experimental Order (Observation Order)	Run	Parameters for catalyst preparation			Catalysts	% Removal of MO (3 h under visible)	
		A	B	C		(I)	(E)
1	1	400	5	0.0	T400-5 (I)	25.09	21.69
2	2	500	5	0.0	T500-5(I)	23.73	21.75
3	9	400	5	1.0	BT400-5-1 (I)	47.67	41.54
4	10	500	5	1.0	BT500-5-1 (I)	57.64	49.84
5	13	400	5	0.0	T400-5 (II)	26.34	22.83
6	14	500	5	0.0	T500-5 (II)	23.03	21.38
7	21	400	5	1.0	BT400-5-1 (II)	52.12	45.49
8	22	500	5	1.0	BT500-5-1 (II)	62.75	55.13
9	5	400	5	0.5	BT400-5-0.5 (I)	39.66	34.33
10	17	400	5	0.5	BT400-5-0.5(II)	40.62	35.12
11	6	500	5	0.5	BT500-5-0.5 (I)	54.04	46.91
12	3	400	10	0.0	T400-10 (I)	21.95	18.69
13	18	500	5	0.5	BT500-5-0.5 (II)	54.76	47.40
14	15	400	10	0.0	T400-10 (II)	22.93	19.26
15	4	500	10	0.0	T500-10 (I)	20.02	19.07

Table 5.27 The removal of methyl orange from photocatalytic degradation under visible light irradiation over all TiO₂ catalysts from the 2 x 2 x 3 factorial design study (continue).

Experimental Order (Observation Order)	Run	Parameters for catalyst preparation			Catalysts	% Removal of MO (3 h under visible)	
		A	B	C		(I)	(E)
16	16	500	10	0.0	T500-10 (II)	22.58	20.88
17	12	500	10	1.0	BT500-10-1 (I)	72.79	66.48
18	11	400	10	1.0	BT400-10-1 (I)	65.88	57.82
19	7	400	10	0.5	BT400-10-0.5 (I)	43.35	37.88
20	8	500	10	0.5	BT500-10-0.5 (I)	51.75	43.86
21	19	400	10	0.5	BT400-10-0.5 (II)	45.94	41.24
22	20	500	10	0.5	BT500-10-0.5 (II)	53.19	46.48
23	23	400	10	1.0	BT400-10-1 (II)	66.77	58.81
24	24	500	10	1.0	BT500-10-1 (II)	71.04	64.66

5.3.2.1 Analysis of variance (ANOVA)

Analysis of variance was employed to assess the significance of the main effects and their interactions. The result of the experimental data analysis by Minitab was displayed in Table 5.28-5.30

Table 5.28 The analysis of variance (ANOVA) of the removal from photocatalytic degradation and adsorption under visible light irradiation

Source	Degree of freedom	Adjusted Sum of Square	Adjusted Mean of Square	F-Value	P-Value	Status
Model	11	7015.22	637.75	220.05	0.000	Significant
Linear	4	6498.34	1624.58	560.54	0.000	Significant
A	1	198.38	198.38	68.45	0.000	Significant
B	1	107.27	107.27	37.01	0.000	Significant
C	2	6192.69	3096.35	1068.36	0.000	Significant
2-Way Interactions	5	500.87	100.17	34.56	0.000	Significant
A*B	1	16.50	16.50	5.69	0.034	Significant
A*C	2	177.78	88.89	30.67	0.000	Significant
B*C	2	306.59	153.30	52.89	0.000	Significant
3-Way Interactions	2	16.01	8.01	2.76	0.103	Not significant
A*B*C	2	16.01	8.01	2.76	0.103	Not significant
Error	12	34.78	2.90			
Total	23	7050.00				

Table 5.29 The analysis of variance (ANOVA) of the removal from photocatalytic degradation, excluding the adsorption under visible light irradiation

Source	Degree of freedom	Adjusted Sum of Square	Adjusted Mean of Square	F-Value	P-Value	Status
Model	11	5502.90	500.26	166.91	0.000	Significant
Linear	4	5088.25	1272.06	424.41	0.000	Significant
A	1	199.18	199.18	66.45	0.000	Significant
B	1	111.46	111.46	37.19	0.000	Significant
C	2	4777.61	2388.81	796.99	0.000	Significant
2-Way Interactions	5	396.28	79.26	26.44	0.000	Significant
A*B	1	7.80	7.80	2.60	0.133	Not significant
A*C	2	95.21	47.61	15.88	0.000	Significant
B*C	2	293.27	146.64	48.92	0.000	Significant
3-Way Interactions	2	18.37	9.18	3.06	0.084	Not significant
A*B*C	2	18.37	9.18	3.06	0.084	Not significant
Error	12	35.97	3.00			
Total	23	5538.87				

Table 5.30 The model summary from the analysis of variance (ANOVA) of the removal of methyl orange from photocatalytic degradation under visible light irradiation.

Including adsorption under visible light irradiation	
R-squared	99.51%
Adjusted R-squared	99.05%
Predicted R-squared	98.03%
Standard Deviation	1.70242
Regression equation	See Appendix H.3 (Table H.5)
Excluding adsorption under visible light irradiation	
R-squared	99.35%
Adjusted R-squared	98.76%
Predicted R-squared	97.40%
Standard Deviation	1.73127
Regression equation	See Appendix H.4 (Table H.6)

In Table 5.28-5.29 the statistical F-test was performed on the main effects and their interactions for the removal of methyl orange under visible light irradiation from photocatalytic degradation that included (I) or excluded (E) the at the significance level of $\alpha = 0.05$ as follows.

Hypotheses testing of the main factors

H_0 : Main effect does not influence the removal of methyl orange under visible light irradiation from photocatalytic degradation.

H_1 : Main effect influences the removal of methyl orange under visible light irradiation from photocatalytic degradation.

When considering the P-value of the main effect in Table 5.28-5.29, the main effects A, B, and C had P-value less than the significance level $\alpha = 0.05$ [6]. Therefore, calcination temperature, calcination time, and molar ratio of reducing agent had significant effects on the removal of methyl orange under visible light irradiation from photocatalytic degradation.

Hypotheses testing of the interaction of each factor

H₀: Interaction effect does not influence the removal of methyl orange under visible light irradiation from photocatalytic degradation.

H₁: Interaction effect influences the removal of methyl orange under visible light irradiation from photocatalytic degradation.

When considering the P-value of the interaction effect in Table 5.28-5.29, the following conclusions were drawn.

1) From Table 5.28, Interaction Effects **A*B**, **A*C** and **B*C** had a P-value less than the significance level $\alpha = 0.05$. Therefore, the interaction between calcination temperature and calcination time, the interaction between calcination temperature and molar ratio reducing agent and the interaction between calcination time and molar ratio of reducing agent significantly affected the removal of methyl orange under visible light irradiation from photocatalytic degradation that included adsorption.

2) From Table 5.28, Interaction Effects **A*B*C** had a P-value greater than the significance level $\alpha = 0.05$. Therefore, the interaction between calcination temperature, calcination time and molar ratio of reducing agent did not significantly affect the removal of methyl orange under visible light irradiation from photocatalytic degradation that included that included adsorption.

3) From Table 5.29, Interaction Effects **A*C** and **B*C** had a P-value less than the significance level $\alpha = 0.05$. Therefore, the interaction between calcination temperature and molar ratio reducing agent and the interaction between calcination

time and molar ratio of reducing agent significantly affected the removal of methyl orange under visible light irradiation from photocatalytic degradation, excluding the adsorption.

4) From Table 5.29, Interaction Effects **A*B** and **A*B*C** had a P-value greater than the significance level $\alpha = 0.05$. Therefore, the interaction between calcination temperature and calcination time and the interaction between calcination temperature, calcination time and molar ratio of reducing agent did not significantly affect the removal of methyl orange under visible light irradiation from photocatalytic degradation, excluding the adsorption.

In addition, the effect of the main factors and their interactions on the removal of methyl orange under visible light irradiation from photocatalytic degradation that included and excluded the adsorption, which was assessed by the Pareto Chart in Figure I.1 (c)-(d) (see Appendix I.1) which exhibited the absolute value of the effects. If the bar associated with any factor exceeded the value of the reference line (represented by a dashed line), such factor had a significant effect and was included in the model. From Figure I.1 (c)-(d) the insignificant factors were **A*B*C**. This agreed with the result of analysis of variance (ANOVA) in Table 5.28-5.29.

5.3.2.2 Analysis of residuals

The data from the analysis of residuals as shown in Table 5.31-5.32, were assessed to check the validity of the error term from the results of the removal of methyl orange from photocatalytic degradation under visible light irradiation that included and excluded the adsorption.

1) Assessing the normality of data

The normal probability plots of residuals were shown as Figure I.4 (a) and Figure I.5 (a) (see Appendix I.4-I.5). This indicated that the data were arranged in a straight line manner and concluded that they had a normal distribution.

2) Assessing the independence of data

The plots of residuals versus the order of the data that were shown as Figure 1.4 (b) and Figure 1.5 (b) (see Appendix 1.4-1.5). This indicated that the distribution of the residuals had no exact direction and concluded that the independence of the observation orders was acceptable.

3) Assessing the stability of variance of data

The plots of residuals versus fitted values that were shown as Figure 1.4(c) and Figure 1.5(c) (see Appendix 1.4-1.5). This indicated that the distribution of residuals had no exact direction and concluded that the variance of this experimental data was relatively constant.

The plots of residuals versus the values of each level of factors A, B, and C were shown Figures 1.4 (d, e, and f) and Figures 1.5 (d, e, and f) (see Appendix 1.4-1.5). This indicated that the variance of this experimental data was relatively constant, especially residuals versus factor A.

Table 5.31 Fits and diagnostics for all observations of the removal from photocatalytic degradation and adsorption under visible light irradiation

Observation order	% Conversion of MO after 4 h (3 h in visible)	Fitted values	Residuals
1	25.09	25.72	-0.63
2	23.73	23.38	0.35
3	47.67	49.89	-2.22
4	57.64	60.19	-2.55
5	26.34	25.72	0.62
6	23.03	23.38	-0.35
7	52.12	49.89	2.23
8	62.75	60.19	2.56
9	39.66	40.14	-0.48
10	40.62	40.14	0.48
11	54.04	54.40	-0.36
12	21.95	22.44	-0.49
13	54.76	54.40	0.36
14	22.93	22.44	0.49
15	20.02	21.30	-1.28
16	22.58	21.30	1.28
17	72.79	71.91	0.88
18	65.88	66.32	-0.44
19	43.35	44.64	-1.29
20	51.75	52.47	-0.72
21	45.94	44.64	1.30
22	53.19	52.47	0.72
23	66.77	66.32	0.45
24	71.04	71.91	-0.87

Table 5.32 Fits and diagnostics for all observations of the removal from photocatalytic degradation, excluding adsorption under visible light irradiation

Observation order	% Removal of MO after 3 h under visible	Fitted values	Residuals
1	21.69	22.26	-0.57
2	21.75	21.57	0.18
3	41.54	43.51	-1.97
4	49.84	52.48	-2.64
5	22.83	22.26	0.57
6	21.38	21.57	-0.19
7	45.49	43.51	1.98
8	55.13	52.48	2.65
9	34.33	34.73	-0.40
10	35.12	34.73	0.39
11	46.91	47.16	-0.25
12	18.69	18.98	-0.29
13	47.40	47.16	0.24
14	19.26	18.98	0.28
15	19.07	19.98	-0.91
16	20.88	19.98	0.90
17	66.48	65.57	0.91
18	57.82	58.31	-0.49
19	37.88	39.56	-1.68
20	43.86	45.17	-1.31
21	41.24	39.56	1.68
22	46.48	45.17	1.31
23	58.81	58.31	0.50
24	64.66	65.57	-0.91

CHAPTER 6

CONCLUSIONS

In this chapter, Section 6.1 provides the conclusions from our study. Also, the recommendations for further study are given in Section 6.2

6.1 Conclusions

Black TiO₂ catalysts were successfully prepared from white TiO₂ that was synthesized by sol-gel method. The reduction process employed NaBH₄ as a reduction agent and calcination temperature, calcination time and molar ratio of reducing agent to white TiO₂ catalysts were varied. An increase in calcination temperature, calcination time, and amount of reducing agent to be black TiO₂ brought about an increase in Ti³⁺/Ti⁴⁺ peak area ratio and the amount of oxygen vacancies. The band gap energy of the catalyst became narrower and the catalyst exhibited smaller photoluminescence signal. Therefore, black TiO₂ absorbed light in the visible light region better and led to higher photocatalytic activities in both UV and visible light irradiations. The order of increasing photocatalytic activities of the catalysts that were calcined at 400 °C and 500 °C under both UV and visible light irradiations was consistent with the results from photoluminescence spectroscopy, UV-visible reflectance spectroscopy, and X-ray photoelectron (XPS). This was attributed to the surface defect present in black TiO₂, which retarded the charge recombination rate and improved the photocatalytic degradation rate. Black TiO₂ that was calcined at 500 °C for 10 hours and molar ratio of reducing agent to white TiO₂ of 1:1 (BT-500-10-1) exhibited highest photocatalytic activity at 82.17% and 71.92% under UV and visible light irradiation, respectively. Since the photon energy of UV light source was more than that of visible light source, resulting in it had more photon energy to excite electrons to higher energy levels during the process under UV irradiation. Also, it was beneficial to improve the photocatalytic activity since the

narrow band gap energies of black TiO₂ catalysts were much less than the aforementioned photon energies.

From the analysis of variance (ANOVA) of the removal of methyl orange results under UV and visible light irradiation, the main effect of factor A, B, and C (as calcination temperature, calcination time, and molar ratio of reducing agent to catalyst, respectively) and the interactions of factors between A*C and B*C had significant effects on the removal of methyl orange from photocatalytic degradation under UV and visible light irradiation. Also, their regression models from the analysis of variance (ANOVA) were statistically significant with high coefficients of determination (R^2). This indicated that they were good for the prediction of the removal of methyl orange from photocatalytic degradation under UV and visible light irradiation.

6.2 Recommendations for future studies

1. Investigate the effect of other reaction conditions such as the light intensity, or initial pH of the solution on the photocatalytic conversion of methyl orange.
2. Design a photoreactor that achieves highly efficient photocatalytic degradation.
3. Modify the defect engineering on the surface area of black TiO₂ using various means such as adding the support with a high surface area (e.g. activated carbon or mesoporous carbon) or doping the transition metals.

REFERENCES

- [1] Sarkar, S.; Banerjee, A.; Halder, U.; Biswas, R. and Bandopadhyay, R., Degradation of Synthetic Azo Dyes of Textile Industry: a Sustainable Approach Using Microbial Enzymes. *Water Conservation Science and Engineering* **2017**, *2* (4), 121-131.
- [2] Shah, M. P., Azo Dye Removal Technologies. *Austin Journal of Biotechnology & Bioengineering* **2018**, *5* (1), 1090-1095.
- [3] Sarkheil, H.; Noormohammadi, F.; Rezaei, A. R. and Borujeni, M. K., Dye Pollution Removal from Mining and Industrial Wastewaters using Chitosan Nanoparticles. *International Conference on Agriculture, Environment and Biological Sciences* **2014**, 37-43.
- [4] Fujishima, A. and Honda, K., Electrochemical photolysis of water at a semiconductor electrode. *Nature* **1972**, *238* (5358), 37-38.
- [5] Hashimoto, K.; Irie, H. and Fujishima, A., Azo Dye Removal Technologies. *Japanese Journal of Applied Physics* **2006**, *44* (12), 8269-8285.
- [6] Saien, J. and Mesgari, Z., Photocatalytic degradation of methyl orange using hematoporphyrin/N-doped TiO₂ nanohybrids under visible light: Kinetics and energy consumption. *Applied Organometallic Chemistry* **2017**, *31* (11).
- [7] El-Sherbiny, S.; Morsy, F.; Samir, M. and Fouad, O. A., Synthesis, characterization and application of TiO₂ nanopowders as special paper coating pigment. *Applied Nanoscience* **2013**, *4* (3), 305-313.
- [8] Ansari, S. A. and Cho, M. H., Highly Visible Light Responsive, Narrow Band gap TiO₂ Nanoparticles Modified by Elemental Red Phosphorus for Photocatalysis and Photoelectrochemical Applications. *Scientific Reports* **2016**, *6*, 25405.
- [9] Xiong, J.; Di, J.; Xia, J.; Zhu, W. and Li, H., Surface Defect Engineering in 2D Nanomaterials for Photocatalysis. *Advanced Functional Materials* **2018**, *28* (39).
- [10] Chen, X.; Liu, L.; Yu, P. Y. and Mao, S. S., Increasing Solar Absorption for Photocatalysis with Black Hydrogenated Titanium Dioxide Nanocrystals. *Science* **2011**, *331*, 746-747.

- [11] Yan, X.; Li, Y. and Xia, T., Black Titanium Dioxide Nanomaterials in Photocatalysis. *International Journal of Photoenergy* **2017**, *2017*, 1-16.
- [12] Kang, Q.; Cao, J.; Zhang, Y.; Liu, L.; Xu, H. and Ye, J., Reduced TiO₂ nanotube arrays for photoelectrochemical water splitting. *Journal of Materials Chemistry A* **2013**, *1* (18), 5766-5774.
- [13] Fang, W.; Xing, M. and Zhang, J., A new approach to prepare Ti³⁺ self-doped TiO₂ via NaBH₄ reduction and hydrochloric acid treatment. *Applied Catalysis B: Environmental* **2014**, *160-161*, 240-246.
- [14] Liu, X.; Hou, B.; Wang, G.; Cui, Z.; Zhu, X. and Wang, X., Black titania/graphene oxide nanocomposite films with excellent photothermal property for solar steam generation. *Journal of Materials Research* **2018**, *33* (6), 674-684.
- [15] Zallen, R. and Moret, M. P., The optical absorption edge of brookite TiO₂. *Solid State Communications* **2006**, *137* (3), 154-157.
- [16] Wakefield, G.; Green, M.; Lipscomb, S. and Flutter, B., Modified titania nanomaterials for sunscreen applications – reducing free radical generation and DNA damage. *Materials Science and Technology* **2013**, *20* (8), 985-988.
- [17] Haider, A. J.; Jameel, Z. N. and Al-Hussaini, I. H. M., Review on: Titanium Dioxide Applications. *Energy Procedia* **2019**, *157*, 17-29.
- [18] Regonini, D.; Bowen, C. R.; Jaroenworarluck, A. and Stevens, R., A review of growth mechanism, structure and crystallinity of anodized TiO₂ nanotubes. *Materials Science and Engineering: R: Reports* **2013**, *74* (12), 377-406.
- [19] Akpan, U. G. and Hameed, B. H., Parameters affecting the photocatalytic degradation of dyes using TiO₂-based photocatalysts: a review. *Journal of Hazardous Materials* **2009**, *170* (2-3), 520-9.
- [20] Chen, Y.-F.; Lee, C.-Y.; Yeng, M.-Y. and Chiu, H.-T., The effect of calcination temperature on the crystallinity of TiO₂ nanopowders. *Journal of Crystal Growth* **2003**, *247*, 363-370.
- [21] Kang, X.; Liu, S.; Dai, Z.; He, Y.; Song, X. and Tan, Z., Titanium Dioxide: From Engineering to Applications. *Catalysts* **2019**, *9* (2).
- [22] Behnajady, M. A.; Eskandarloo, H.; Modirshahla, N. and Shokri, M., Investigation of the effect of sol-gel synthesis variables on structural and photocatalytic

- properties of TiO₂ nanoparticles. *Desalination* **2011**, 278 (1-3), 10-17.
- [23] Yahaya, M. Z.; Azam, M. A.; Teridi, M. A. M.; Singh, P. K. and Mohamad, A. A., Recent Characterisation of Sol-Gel Synthesised TiO₂ Nanoparticles. In *Recent Applications in Sol-Gel Synthesis*, 2017; pp 109-121.
- [24] Liu, Y.; Tian, L.; Tan, X.; Li, X. and Chen, X., Synthesis, properties, and applications of black titanium dioxide nanomaterials. *Science Bulletin* **2017**, 62 (6), 431-441.
- [25] Liu, Y. and Chen, X., Black Titanium Dioxide for Photocatalysis. In *Semiconductors for Photocatalysis*, 2017; pp 393-428.
- [26] Muir, S. S. Sodium Borohydride Production and Utilisation for Improved Hydrogen Storage. The University of Queensland, 2013.
- [27] Martelli, P.; Caputo, R.; Remhof, A.; Mauron, P.; Borgschulte, A. and Zuttel, A., Stability and Decomposition of NaBH₄. *Journal of Physical Chemistry C* **2010**, 114, 7173-7177.
- [28] Fu, L.; Bai, Y. N.; Lu, Y. Z.; Ding, J.; Zhou, D. and Zeng, R. J., Degradation of organic pollutants by anaerobic methane-oxidizing microorganisms using methyl orange as example. *Journal of Hazardous Materials* **2019**, 364, 264-271.
- [29] Radhakrishin, J. S. and Saraswati, N. P., Microbial decolorization of Methyl Orange by *Klebsiella* spp. DA26. *International Journal of Research in Biosciences* **2015**, 4 (3), 27-36.
- [30] Sejie, F. P. and Nadiye-Tabbiruka, M. S., Removal of Methyl Orange (MO) from Water by adsorption onto Modified Local Clay (Kaolinite). *Physical Chemistry* **2016**, 6 (2), 39-48.
- [31] López, R. C. and Cervantes, S. C., Effect of the phase composition and crystallite size of sol-gel TiO₂ nanoparticles on the acetaldehyde photodecomposition. *Superficies y Vacío* **2012**, 25 (2), 82-87.
- [32] Wang, G.; Xu, D.; Guo, W.; Wei, X.; Sheng, Z. and Li, Z., Preparation of TiO₂ nanoparticle and photocatalytic properties on the degradation of phenol. *IOP Conference Series: Earth and Environmental Science* **2017**, 59, 1-5.
- [33] Wu, H.; Ma, J.; Zhang, C. and He, H., Effect of TiO₂ calcination temperature on the photocatalytic oxidation of gaseous NH₃. *Journal of Environmental Sciences*

- 2014**, 26 (3), 673-682.
- [34] Gautam, A.; Kshirsagar, A.; Biswas, R.; Banerjee, S. and Khanna, P. K., Photodegradation of organic dyes based on anatase and rutile TiO₂ nanoparticles. *RSC Advances* **2016**, 6 (4), 2746-2759.
- [35] Assia, B.; Boudine, B. and Boudaren, C., Synthesis, structural characterization and photocatalytic activity of TiO₂ nanoparticles. *Courrier du Savoir* **2018**, 26, 495-500.
- [36] Malnieks, K.; Mezinskis, G.; Pavlovskā, I.; Bidermanis, L. and Pludons, A., Optical, photocatalytic and structural properties of TiO₂ – SiO₂ sol-gel coatings on high content SiO₂ enamel surface. *Materials Science* **2015**, 21 (1), 100-104.
- [37] Tan, H.; Zhao, Z.; Niu, M.; Mao, C.; Cao, D.; Cheng, D.; Feng, P. and Sun, Z., A facile and versatile method for preparation of colored TiO₂ with enhanced solar-driven photocatalytic activity. *Nanoscale* **2014**, 6 (17), 10216-10223.
- [38] Ariyanti, D.; Mills, L.; Dong, J.; Yao, Y. and Gao, W., NaBH₄ modified TiO₂: Defect site enhancement related to its photocatalytic activity. *Materials Chemistry and Physics* **2017**, 199, 571-576.
- [39] He, M.; Ji, J.; Liu, B. and Huang, H., Reduced TiO₂ with tunable oxygen vacancies for catalytic oxidation of formaldehyde at room temperature. *Applied Surface Science* **2019**, 473, 934-942.
- [40] Bu, X.; Yang, S.; Bu, Y.; He, P.; Yang, Y.; Wang, G.; Li, H.; Wang, P.; Wang, X.; Ding, G.; Yang, J. and Xie, X., Highly Active Black TiO₂/N-doped Graphene Quantum Dots Nanocomposites For Sunlight Driven Photocatalytic Sewage Treatment. *ChemistrySelect* **2018**, 3 (1), 201-206.
- [41] Jiang, L.; Li, Y. Z.; Yang, H. Y.; Yang, Y. P.; Liu, J.; Yan, Z. Y.; Long, X.; He, J. and Wang, J. Q., Low-Temperature Sol-Gel Synthesis of Nitrogen-Doped Anatase/Brookite Biphase Nanoparticles with High Surface Area and Visible-Light Performance. *Catalysts* **2017**, 7 (12), 376-385.
- [42] Mohamed, M. A.; Wan Salleh, W. N.; Jaafar, J. and Yusof, N., Preparation and Photocatalytic Activity of Mixed Phase Anatase/rutile TiO₂ Nanoparticles for Phenol Degradation. *Jurnal Teknologi* **2014**, 70 (2), 65-70.
- [43] Gaber, A.; Abdel-Rahim, M. A.; Abdel-Latif, A. Y. and Abdel-Salam, M. N.,

- Influence of Calcination Temperature on the Structure and Porosity of Nanocrystalline SnO₂ Synthesized by a Conventional Precipitation method. *International Journal of Electrochemical Science* **2014**, 9 (1), 81-95.
- [44] Castrejón-Sánchez, V.; López, R.; Ramón-González, M.; Enríquez-Pérez, Á.; Camacho-López, M. and Villa-Sánchez, G., Annealing Control on the Anatase/Rutile Ratio of Nanostructured Titanium Dioxide Obtained by Sol-Gel. *Crystals* **2018**, 9 (1), 22-33.
- [45] Raj, K. J. A. and Viswanathan, B., Effect of surface area, pore volume and particle size of P25 titania on the phase transformation of anatase to rutile. *Indian Journal of Chemistry* **2009**, 48, 1378-1382.
- [46] Li, Z.; Gao, B.; Chen, G. Z.; Mokaya, R.; Sotiropoulos, S. and Li Puma, G., Carbon nanotube/titanium dioxide (CNT/TiO₂) core-shell nanocomposites with tailored shell thickness, CNT content and photocatalytic/photoelectro-catalytic properties. *Applied Catalysis B: Environmental* **2011**, 110, 50-57.
- [47] Hu, M.; Cao, Y.; Li, Z.; Yang, S. and Xing, Z., Ti³⁺ self-doped mesoporous black TiO₂ /SiO₂ nanocomposite as remarkable visible light photocatalyst. *Applied Surface Science* **2017**, 426, 734-744.
- [48] Reich, S.-J.; Svidrytski, A.; Hölzel, A.; Wang, W.; Kübel, C.; Hlushkou, D. and Tallarek, U., Transport under confinement: Hindrance factors for diffusion in core-shell and fully porous particles with different mesopore space morphologies. *Microporous and Mesoporous Materials* **2019**, 282, 188-196.
- [49] Christian, M. L. and Aguey-Zinsou, K. F., Core-shell strategy leading to high reversible hydrogen storage capacity for NaBH₄. *ACS Nano* **2012**, 6 (9), 7739-7751.
- [50] Mao, J. and Gregory, D., Recent Advances in the Use of Sodium Borohydride as a Solid State Hydrogen Store. *Energies* **2015**, 8 (1), 430-453.
- [51] Pan, X.; Yang, M. Q.; Fu, X.; Zhang, N. and Xu, Y. J., Defective TiO₂ with oxygen vacancies: synthesis, properties and photocatalytic applications. *Nanoscale* **2013**, 5 (9), 3601-14.
- [52] Xin, X.; Xu, T.; Yin, J.; Wang, L. and Wang, C., Management on the location and concentration of Ti³⁺ in anatase TiO₂ for defects-induced visible-light photocatalysis. *Applied Catalysis B: Environmental* **2015**, 176-177, 354-362.

- [53] Niu, B.; Wang, X.; Wu, K.; He, X. and Zhang, R., Mesoporous Titanium Dioxide: Synthesis and Applications in Photocatalysis, Energy and Biology. *Materials (Basel)* **2018**, *11* (10), 1910-1932.
- [54] Chen, H.; Lu, Y.; Zhu, H.; Guo, Y.; Hu, R.; Khatoon, R.; Chen, L.; Zeng, Y.-J.; Jiao, L.; Leng, J. and Lu, J., Crystalline SnO₂ @ amorphous TiO₂ core-shell nanostructures for high-performance lithium ion batteries. *Electrochimica Acta* **2019**, *310*, 203-212.
- [55] Xu, Y.; Wu, S.; Wan, P.; Sun, J. and Hood, Z. D., Introducing Ti³⁺ defects based on lattice distortion for enhanced visible light photoreactivity in TiO₂ microspheres. *RSC Advances* **2017**, *7* (52), 32461-32467.
- [56] Liu, Y.; Zhang, P.; Tian, B. and Zhang, J., Enhancing the photocatalytic activity of CdS nanorods for selective oxidation of benzyl alcohol by coating amorphous TiO₂ shell layer. *Catalysis Communications* **2015**, *70*, 30-33.
- [57] Ye, M.; Zhou, H.; Zhang, T.; Zhang, Y. and Shao, Y., Preparation of SiO₂@Au@TiO₂ core-shell nanostructures and their photocatalytic activities under visible light irradiation. *Chemical Engineering Journal* **2013**, *226*, 209-216.
- [58] Ren, R.; Wen, Z.; Cui, S.; Hou, Y.; Guo, X. and Chen, J., Controllable Synthesis and Tunable Photocatalytic Properties of Ti(³⁺)-doped TiO₂. *Scientific Reports* **2015**, *5*, 10714.
- [59] Tian, J.; Hu, X.; Yang, H.; Zhou, Y.; Cui, H. and Liu, H., High yield production of reduced TiO₂ with enhanced photocatalytic activity. *Applied Surface Science* **2016**, *360*, 738-743.
- [60] Zhang, H.; Zhou, M.; Fu, Q.; Lei, B.; Lin, W.; Guo, H.; Wu, M. and Lei, Y., Observation of defect state in highly ordered titanium dioxide nanotube arrays. *Nanotechnology* **2014**, *25* (27), 275603-275612.
- [61] Song, H.; Li, C.; Lou, Z.; Ye, Z. and Zhu, L., Effective Formation of Oxygen Vacancies in Black TiO₂ Nanostructures with Efficient Solar-Driven Water Splitting. *ACS Sustainable Chemistry & Engineering* **2017**, *5* (10), 8982-8987.
- [62] Ullattil, S. G. and Periyat, P., A 'one pot' gel combustion strategy towards Ti³⁺-self-doped 'black' anatase TiO_{2-x} solar photocatalyst. *Journal of Materials Chemistry A* **2016**, *4* (16), 5854-5858.

- [63] Samsudin, E. M.; Hamid, S. B. A.; Juan, J. C.; Basirun, W. J. and Kandjani, A. E., Surface modification of mixed-phase hydrogenated TiO₂ and corresponding photocatalytic response. *Applied Surface Science* **2015**, *359*, 883-896.
- [64] Chen, X.; Liu, L.; Liu, Z.; Marcus, M. A.; Wang, W. C.; Oyler, N. A.; Grass, M. E.; Mao, B.; Glans, P. A.; Yu, P. Y.; Guo, J. and Mao, S. S., Properties of disorder-engineered black titanium dioxide nanoparticles through hydrogenation. *Scientific Reports* **2013**, *3*, 1510-1516.
- [65] Zheng, Z.; Huang, B.; Lu, J.; Wang, Z.; Qin, X.; Zhang, X.; Dai, Y. and Whangbo, M. H., Hydrogenated titania: synergy of surface modification and morphology improvement for enhanced photocatalytic activity. *Chemical communications (Cambridge, England)* **2012**, *48* (46), 5733-5735.
- [66] Hadi, H. M. and Wahab, H. S., Visible Light Photocatalytic Decolourization of Methyl Orange Using N-Doped TiO₂ Nanoparticles. *Journal of Al-Nahrain University* **2015**, *18* (3), 1-9.
- [67] Ali, A. H.; Naser, G. F. and Mohammed, S. A., Photocatalytic Degradation of Methyl Orange Dye using Different Photocatalysts under Solar Light. *International Journal of ChemTech Research* **2016**, *9*, 157-165.
- [68] Guettaï, N. and Ait Amar, H., Photocatalytic oxidation of methyl orange in presence of titanium dioxide in aqueous suspension. Part I: Parametric study. *Desalination* **2005**, *185* (1-3), 427-437.
- [69] Subha, P. P. and Jayaraj, M. K., Solar photocatalytic degradation of methyl orange dye using TiO₂ nanoparticles synthesised by sol-gel method in neutral medium. *Journal of Experimental Nanoscience* **2014**, *10* (14), 1106-1115.
- [70] Luenloi, T.; Chalermssinsuwan, B.; Sreethawong, T. and Hinchiranan, N., Photodegradation of phenol catalyzed by TiO₂ coated on acrylic sheets: Kinetics and factorial design analysis. *Desalination* **2011**, *274* (1-3), 192-199.
- [71] Factorial Experimental Design for the Optimization of β -Naphthol Photocatalytic Degradation in TiO₂ Aqueous Suspension. *Canadian Chemical Transactions* **2014**, 1-11.
- [72] Hamdi, H.; Namane, A. and Dalila Hank, A. H., Coupling of Photocatalysis and

Biological Treatment for Phenol Degradation: Application of Factorial Design Methodology. *Journal of Materials and Environmental Sciences* **2017** 8(11), 3953-3961.





APPENDICES

จุฬาลงกรณ์มหาวิทยาลัย
CHULALONGKORN UNIVERSITY

APPENDIX A

CALCULATION OF CATALYST PREPARATION

Preparation of black titanium dioxide catalyst

Reagents:

Titanium dioxide (TiO₂) powder was prepared by a sol-gel method.

Sodium borohydride 99%, NaBH₄ (Sigma-Aldrich Inc.)

Calculation for the preparation of black TiO₂ catalyst

For example, to determine the amount of the reducing agent (NaBH₄) if we use 3.0 g of TiO₂ as the initial amount of catalyst for molar ratio of NaBH₄ / TiO₂ = 1:1

$$\text{Molar ratio of NaBH}_4 / \text{TiO}_2 = \frac{\text{Mole of NaBH}_4}{\text{Mole of TiO}_2} \quad (\text{A.1})$$

$$\frac{1}{1} = \frac{\frac{\text{amount of NaBH}_4}{\text{MW of NaBH}_4}}{\frac{\text{amount of TiO}_2}{\text{MW of TiO}_2}}$$

$$\frac{1}{1} = \frac{\frac{\text{amount of NaBH}_4}{\text{g}}}{\frac{3 \text{ g}}{79.866 \frac{\text{g}}{\text{mole}}}}$$

$$\text{Amount of NaBH}_4 = 1.421 \text{ g}$$

Note: Molecular weight of TiO₂ equals 79.866 g/mole

Molecular weight of NaBH₄ equals 37.83 g/mole

APPENDIX B

CALCULATION OF THE CRYSTALLITE SIZE

Calculation of the crystallite size by Debye-Scherrer equation.

The crystallite size was calculated from FWHM (the width at half-height of XRD diffraction peak using the Debye-Scherrer equation as the following.

$$D = \frac{k\lambda}{\beta \cos\theta} \quad (\text{B.1})$$

Where D = Crystallite size, \AA

k = Crystallite shape factor = 0.90

λ = X-ray wavelength (1.5418\AA for $\text{CuK}\alpha$)

θ = Observed peak angle, degree

β = X-ray diffraction broadening, radian

The X-ray diffraction broadening (β) is the corrected width of diffraction free from all broadening due to the experimental instrument. The standard α -alumina is used to observe the instrumental broadening data. The most common correction for the X-ray diffraction broadening (β) can be obtained by using Warren's equation

From Warren's equation:

$$\beta = \sqrt{\beta_M^2 - \beta_S^2} \quad (\text{B.2})$$

Where β_M = the measured peak width in radians at half peak height.

β_S = the corresponding width of a standard material.

Example: Calculation of the crystallite size of TiO_2 that was calcined at $400 \text{ }^\circ\text{C}$ for 5 hours.

From Figure B.1, the 101 diffraction peak of TiO_2 for calculation of crystallite size. An interesting diffraction peak that was the plane at $2\theta = 25.3671^\circ$

$$\begin{aligned} \text{The half-height width of (101) diffraction peak} &= 0.9636^\circ \\ &= (2\pi \times 0.9636)/360 \\ &= 0.0168 \text{ radian} \end{aligned}$$

The corresponding half-height width of peak of α -alumina = 0.003836 radian

$$\begin{aligned} \text{The broadening } \beta &= \sqrt{\beta_M^2 - \beta_s^2} \\ &= \sqrt{0.0168^2 - 0.003836^2} \\ &= 0.016375 \text{ radian} \end{aligned}$$

Where $\beta = 0.016375$ radian

$$2\Theta = 25.3671^\circ$$

$$\Theta = 12.6836^\circ$$

$$\lambda = 1.5418 \text{ \AA}$$

$$\begin{aligned} \text{The crystallite size} &= \frac{0.9 \times 1.5418}{0.016375 \times \cos(12.6836)} = 86.86 \text{ \AA} \\ &\approx 8.7 \text{ nm} \end{aligned}$$

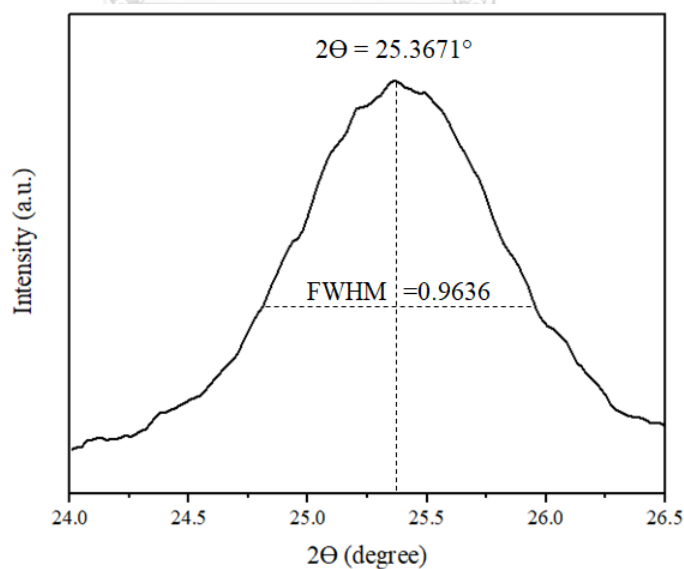


Figure B.1 The diffraction peak of TiO₂ that was calcined at 400 °C for five hours for calculation of the crystallite size.

APPENDIX C
CALCULATION OF THE AMOUNT OF ANATASE, RUTILE, AND BROOKITE
PHASES

The phase of TiO₂ can be detected at 2 Θ of 25.3°, 37.9°, 48.1°, 53.8°, 62.9°, and 75.3° were assigned to anatase phase, while diffraction peaks at 27.4°, 36.1°, and 41.3° corresponded to rutile phase and the peak at 30.8° was specified to brookite phase.

The weight fraction of TiO₂ sample can be calculated as the following equation (C.1- C.3)

$$W_A = \frac{k_A I_A}{k_A I_A + I_R + k_B I_B} \quad (\text{C.1})$$

$$W_R = \frac{I_R}{k_A I_A + I_R + k_B I_B} \quad (\text{C.2})$$

$$W_B = \frac{k_B I_B}{k_A I_A + I_R + k_B I_B} \quad (\text{C.3})$$

Where

W_A = Weight fraction of anatase phase of TiO₂

W_R = Weight fraction of rutile phase of TiO₂

W_B = Weight fraction of brookite phase of TiO₂

I_A = the intensity of main anatase peak height

I_R = the intensity of main rutile peak height

I_B = the intensity of main brookite peak height

k_A = the coefficient factor of anatase was 0.886

k_B = the coefficient factor of brookite was 2.721

Example: Calculation of the phase compositions of TiO_2 that was calcined at $400\text{ }^\circ\text{C}$ for 5 hours.

Table C.1 Height of the intensity of TiO_2 from Origin Pro 2018

Phase	2θ	Intensity of peak height
Anatase	25.37°	1482.24
Rutile	27.51°	297.11
Brookite	30.88°	103.59

Note: Origin Pro 2018 is a program for data processing and non-linear curve fitting.

$$W_A = \frac{(0.886)1482.24}{(0.886)1482.24 + 297.11 + (2.721)103.59} = 0.6940$$

$$W_R = \frac{297.11}{(0.886)1482.24 + 297.11 + (2.721)103.59} = 0.1570$$

$$W_B = \frac{(2.721)103.59}{(0.886)1482.24 + 297.11 + (2.721)103.59} = 0.1490$$

APPENDIX D

CALIBRATION CURVE OF METHYL ORANGE

The calibration curves for calculation concentration of methyl orange for photocatalytic degradation of methyl orange at maximum wavelength of 464 nm as the following figure.

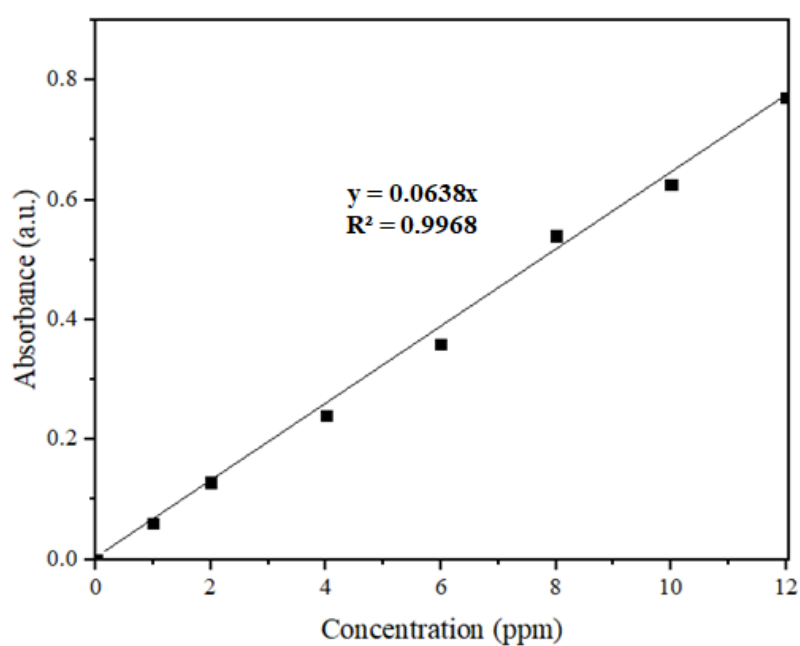


Figure D.1 The calibration curve of methyl orange from scanning by UV-Vis spectrophotometer Perkin-Elmer 650

APPENDIX E

CALCULATION FROM XPS SPECTRA RESULTS

Calculation of the amount of Ti^{3+} defects

The amount of Ti^{3+} defects from XPS measurement can be determined from percentage of peak area between Ti^{4+} and Ti^{3+} . Peak area of Ti 2p in XPS spectra can be calculated by Origin Pro 2018 program. Then, it can be calculated in the peak area ratio of $\text{Ti}^{3+} / \text{Ti}^{4+}$.

Example E.1 To determine the amount of Ti^{3+} defects of TiO_2 calcined at $400\text{ }^\circ\text{C}$ 5 hours from Figure E.1 and Table E.1

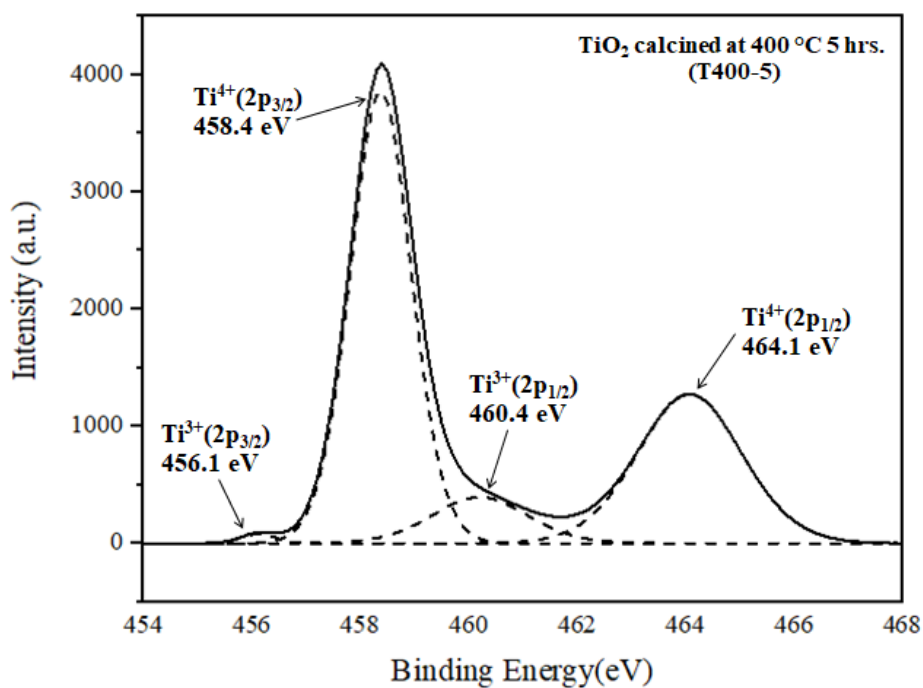


Figure E.1 The XPS spectra for TiO_2 nanoparticles; Ti 2p for T400-5

Table E.1 The peak area of titanium for T400-5 from XPS.

Binding energy (eV)	Peak	Peak Area	Total Peak Area	The peak area ratio of Ti^{3+} / Ti^{4+}
464.1	$Ti^{4+} (2p_{1/2})$	3170.945	8,644.819	0.111
458.4	$Ti^{4+} (2p_{3/2})$	5473.874		
460.2	$Ti^{3+} (2p_{1/2})$	931.955	962.82	
456.1	$Ti^{3+} (2p_{3/2})$	30.665		

$$\text{The amount of } Ti^{3+} \text{ defects} = \frac{\text{Total peak area of } Ti^{3+}}{\text{Total peak area of } Ti^{3+} + \text{Total peak area of } Ti^{4+}} \quad (E.1)$$

$$= \frac{962.82}{962.82 + 8644.819}$$

$$= 0.1002 = 10.02 \%$$

$$\text{The peak area ratio of } Ti^{3+} / Ti^{4+} = \frac{\text{Total peak area of } Ti^{3+}}{\text{Total peak area of } Ti^{4+}} \quad (E.2)$$

$$= \frac{962.82}{8644.819}$$

$$= 0.111$$

Calculation of the amount of oxygen vacancies

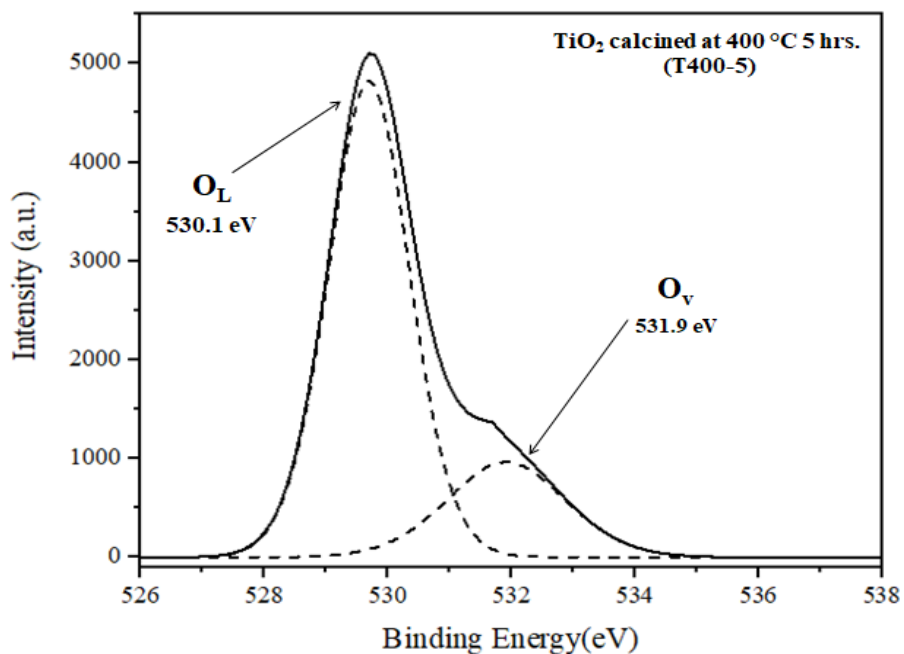


Figure E.2 The XPS spectra for TiO₂ nanoparticles; O 1s for T400-5

Table E.2 The peak area of oxygen for T400-5 from XPS.

Binding energy (eV)	Peak	Name	Peak Area
531.9	O _V	Oxygen vacancies	2335.1315
529.7	O _L	Lattice Oxygen	8024.3021

$$\text{The amount of oxygen vacancies} = \frac{\text{Total peak area of } O_V}{\text{Total peak area of } O_V + \text{Total peak area of } O_L} \quad (\text{E.3})$$

$$= \frac{2335.1315}{2335.1315 + 8024.3021}$$

$$= \frac{2335.1315}{10359.4336} = 0.2254 = 22.54 \%$$

APPENDIX F

CALCULATION OF THE BAND GAP FROM UV-VIS SPECTRA

The band gap energy (E_g) of the catalyst was estimated by the following equation (F.1):

$$E_g = \frac{hc}{\lambda} = h\nu \quad (\text{F.1})$$

$$\text{And } (\alpha h\nu)^2 = \left(\ln \left(\frac{10^{(2-A)}}{100} \right) \right) \times E_g^2 \quad (\text{F.2})$$

Where

E_g is the bandgap energy (eV) of the catalysts

h is the plank constant (6.62×10^{-34} Joules sec)

C is the speed of light = 3×10^8 meter/ sec

ν is the frequency

λ is the wavelength of spectrum (200-800 nm)

A is the absorbance

α is The absorption coefficient in cm^{-1}

$1 \text{ eV} = 1.60 \times 10^{-19} \text{ J}$

CHULALONGKORN UNIVERSITY

The band gap of the catalysts were determined by calculating E_g and $(\alpha h\nu)^2$ (see Equation F.1 and F.2), then plot E_g (x-axis) against $(\alpha h\nu)^2$ (y-axis), and the extrapolation of the linear part until its intersection with E_g axis.

Example: Calculation of the band gap in TiO_2

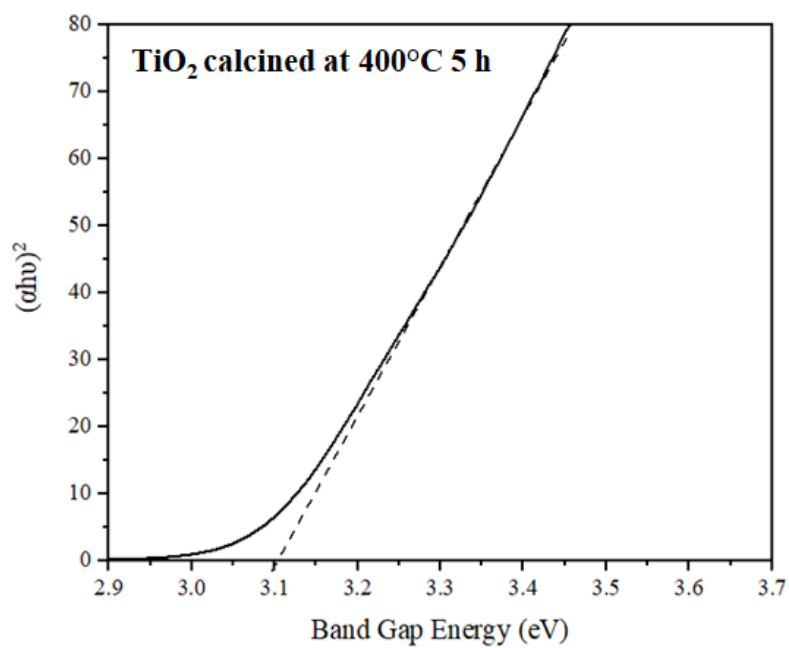


Figure F.1 The band gap of TiO_2

From Figure F.1:

The band gap energy of $\text{TiO}_2 = 3.10 \text{ eV}$

APPENDIX G

THE PROPERTIES OF LIGHTING INSTRUMENT

Intensity of both UV and visible light bulbs was measured by IL 1700 research radiometer (light sensor) as showed in Table G.1

Table G.1 The properties of light bulbs for using in the photocatalytic degradation

Type of light	Type of light bulbs	Power (W)	Intensity of UV light (%)	Intensity of visible light (%)
UV light (253 nm)	Phillips	75	99.69	0.31
Visible light (400-700 nm)	Daylight (Phillips)	18	1.01	98.99

APPENDIX H

THE MATHEMATICAL MODEL FROM STATISTICAL ANALYSIS

From statistical analysis, in order to determine the predicted value of photocatalytic degradation of methyl orange from the regression model, so it can be calculated by using the estimated regression coefficient which obtained from Minitab Statistical Software as the data in Table H.3 – H.6

The code and level values of operating variable for catalyst preparation as shown in Table H.1.

Table H.1 Values of operating variables used in the 2 x 2 x 3 factorial design study

Operating variables	Factor	Code	Level (Values)		
			Low	Medium	High
Calcination temperature (°C)	A	X ₁	400 (-1)	-	500 (+1)
Calcination time (h)	B	X ₂	5 (-1)	-	10 (+1)
Molar ratio of reducing agent to catalyst	C	X ₃	0:1	0.5:1	1:1

The codified mathematical model employed for 2x2x3 factorial design with interactions [70-72] was represented as follows:

$$Y = a_0 + a_1X_1 + a_2X_2 + a_3X_3 + a_{12} X_1X_2 + a_{13} X_1X_3 + a_{23} X_2X_3 + a_{123} X_1X_2X_3 \quad (H.1)$$

Where Y is the estimated response which represents the conversion percentage of methyl orange degradation.

a_0 is a constant term (the independent coefficient)

a_i (i=1,2,3) are linear coefficients for the variables, calcination temperature, calcination time, and molar ratio of reducing agent to catalyst respectively.

a_{ij} (i<j) are the coefficients of the interaction parameters X_i and X_j

The coefficients a_iX_i , $a_{ij}X_{ij}$, and $a_{ijk}X_{ijk}$ were reported by using Minitab

Statistical Software (Minitab Release 16)

Calculation method: Substituting coefficient by their values from Table H.3 – H.6 in the equation H.1 to obtain the estimated response which represents the removal percentage of methyl orange degradation.

For example, to determine the estimated response which represents the removal percentage of methyl orange degradation under UV light irradiation that included adsorption by using BT500-5-1 as the catalyst.

From the data in Table H.3, as shown in Table H.2

Table H.2 Estimated regression coefficients for the removal of methyl orange from the photocatalytic degradation under UV light irradiation that included adsorption of BT500-10-1 catalyst (from Table H.3)

Term	Variables	Coefficients	Standard Error Coefficients	T-Value	P-Value (* < 0.05)
Constant	a_0	56.269	0.382	147.43	0.000*
A					
500	a_1X_1	2.725	0.382	7.14	0.000*
B					
10	a_2X_2	1.771	0.382	4.64	0.001*
C					
1.0	a_3X_3	15.935	0.540	29.52	0.000*
A*B					
500 10	$a_{12}X_1X_2$	-0.751	0.382	-1.97	0.073
A*C					
500 1.0	$a_{13}X_1X_3$	1.339	0.540	2.48	0.029*
B*C					
10 1.0	$a_{23}X_2X_3$	5.355	0.540	9.92	0.000*
A*B*C					
500 10 1.0	$a_{123} X_1X_2X_3$	-0.477	0.540	-0.88	0.394

From equation (H.1), substitute coefficients by their values from Table H.2 in the equation H.1 to obtain the estimated response which represents the removal percentage of methyl orange degradation under UV light irradiation that included adsorption of BT500-10-1 catalyst as follows:

$$\begin{aligned}
 Y &= a_0 + a_1X_1 + a_2X_2 + a_3X_3 + a_{12} X_1X_2 + a_{13} X_1X_3 + a_{23} X_2X_3 + a_{123} X_1X_2X_3 \quad (\text{H.1}) \\
 &= 56.269 + 2.725 + 1.771 + 15.935 + (-0.751) + 1.339 + 5.355 + (-0.477) \\
 &= 82.166 \%
 \end{aligned}$$

$$\%Error = \left| \frac{Y_{\text{predicted}} - Y_{\text{experiment}}}{Y_{\text{experiment}}} \right| \times 100 \quad (\text{H.2})$$

$$\%Error = \left| \frac{82.166 - 82.17}{82.17} \right| \times 100$$

$$\%Error \approx 0.005 \%$$

H.1 the effects of catalyst preparation parameters on the photocatalytic degradation of methyl orange under UV light irradiation that included adsorption

Table H.3 Estimated regression coefficients for the removal of methyl orange from the photocatalytic degradation under UV light irradiation that included adsorption

Term	Variables	Coefficients	Standard Error Coefficients	T-Value	P-Value
Constant	a_0	56.269	0.382	147.43	0.000*
A					
400	a_1X_1	-2.725	0.382	-7.14	0.000*
500	a_1X_1	2.725	0.382	7.14	0.000*
B					
5	a_2X_2	-1.771	0.382	-4.64	0.001*
10	a_2X_2	1.771	0.382	4.64	0.001*
C					
0.0	a_3X_3	-18.419	0.540	-34.12	0.000*
0.5	a_3X_3	2.484	0.540	4.60	0.001*
1.0	a_3X_3	15.935	0.540	29.52	0.000*
A*B					
400 5	$a_{12}X_1X_2$	-0.751	0.382	-1.97	0.073
400 10	$a_{12}X_1X_2$	0.751	0.382	1.97	0.073
500 5	$a_{12}X_1X_2$	0.751	0.382	1.97	0.073
500 10	$a_{12}X_1X_2$	-0.751	0.382	-1.97	0.073

(* p-value < 0.05)

Table H.3 (continue)

Term	Variables	Coefficients	Standard Error Coefficients	T-Value	P-Value
A*C					
400 0.0	$a_{13}X_1X_3$	3.917	0.540	7.26	0.000*
400 0.5	$a_{13}X_1X_3$	-2.578	0.540	-4.78	0.000*
400 1.0	$a_{13}X_1X_3$	-1.339	0.540	-2.48	0.029*
500 0.0	$a_{13}X_1X_3$	-3.917	0.540	-7.26	0.000*
500 0.5	$a_{13}X_1X_3$	2.578	0.540	4.78	0.000*
500 1.0	$a_{13}X_1X_3$	1.339	0.540	2.48	0.029*
B*C					
5 0.0	$a_{23}X_2X_3$	3.761	0.540	6.97	0.000*
5 0.5	$a_{23}X_2X_3$	1.594	0.540	2.95	0.012*
5 1.0	$a_{23}X_2X_3$	-5.355	0.540	-9.92	0.000*
10 0.0	$a_{23}X_2X_3$	-3.761	0.540	-6.97	0.000*
10 0.5	$a_{23}X_2X_3$	-1.594	0.540	-2.95	0.012*
10 1.0	$a_{23}X_2X_3$	5.355	0.540	9.92	0.000*
A*B*C					
400 5 0.0	$a_{123} X_1X_2X_3$	1.109	0.540	2.05	0.062
400 5 0.5	$a_{123} X_1X_2X_3$	-0.631	0.540	-1.17	0.265
400 5 1.0	$a_{123} X_1X_2X_3$	-0.477	0.540	-0.88	0.394
400 10 0.0	$a_{123} X_1X_2X_3$	-1.109	0.540	-2.05	0.062
400 10 0.5	$a_{123} X_1X_2X_3$	0.631	0.540	1.17	0.265
400 10 1.0	$a_{123} X_1X_2X_3$	0.477	0.540	0.88	0.394
500 5 0.0	$a_{123} X_1X_2X_3$	-1.109	0.540	-2.05	0.062
500 5 0.5	$a_{123} X_1X_2X_3$	0.631	0.540	1.17	0.265
500 5 1.0	$a_{123} X_1X_2X_3$	0.477	0.540	0.88	0.394
500 10 0.0	$a_{123} X_1X_2X_3$	1.109	0.540	2.05	0.062
500 10 0.5	$a_{123} X_1X_2X_3$	-0.631	0.540	-1.17	0.265
500 10 1.0	$a_{123} X_1X_2X_3$	-0.477	0.540	-0.88	0.394

H.2 the effects of catalyst preparation parameters on the photocatalytic degradation of methyl orange under UV light irradiation, excluding the adsorption

Table H.4 Estimated regression coefficients for the removal of methyl orange from the photocatalytic degradation under UV light irradiation, excluding the adsorption

Term	Variables	Coefficients	Standard Error Coefficients	T-Value	P-Value
Constant	a_0	51.976	0.423	122.96	0.000*
A					
400	a_1X_1	-2.746	0.423	-6.50	0.000*
500	a_1X_1	2.746	0.423	6.50	0.000*
B					
5	a_2X_2	-1.894	0.423	-4.48	0.001*
10	a_2X_2	1.894	0.423	4.48	0.001*
C					
0.0	a_3X_3	-17.045	0.598	-28.51	0.000*
0.5	a_3X_3	1.834	0.598	3.07	0.010*
1.0	a_3X_3	15.210	0.598	25.44	0.000*
A*B					
400 5	$a_{12}X_1X_2$	-0.666	0.423	-1.58	0.141
400 10	$a_{12}X_1X_2$	0.666	0.423	1.58	0.141
500 5	$a_{12}X_1X_2$	0.666	0.423	1.58	0.141
500 10	$a_{12}X_1X_2$	-0.666	0.423	-1.58	0.141

(* p-value < 0.05)

Table H.4 (continue)

Term	Variables	Coefficients	Standard Error Coefficients	T-Value	P-Value
A*C					
400 0.0	$a_{13}X_1X_3$	3.370	0.598	5.64	0.000*
400 0.5	$a_{13}X_1X_3$	-1.837	0.598	-3.07	0.010*
400 1.0	$a_{13}X_1X_3$	-1.533	0.598	-2.56	0.025*
500 0.0	$a_{13}X_1X_3$	-3.370	0.598	-5.64	0.000*
500 0.5	$a_{13}X_1X_3$	1.837	0.598	3.07	0.010*
500 1.0	$a_{13}X_1X_3$	1.533	0.598	2.56	0.025*
B*C					
5 0.0	$a_{23}X_2X_3$	3.863	0.598	6.46	0.000*
5 0.5	$a_{23}X_2X_3$	1.507	0.598	2.52	0.027*
5 1.0	$a_{23}X_2X_3$	-5.370	0.598	-8.98	0.000*
10 0.0	$a_{23}X_2X_3$	-3.863	0.598	-6.46	0.000*
10 0.5	$a_{23}X_2X_3$	-1.507	0.598	-2.52	0.027*
10 1.0	$a_{23}X_2X_3$	5.370	0.598	8.98	0.000*
A*B*C					
400 5 0.0	$a_{123} X_1X_2X_3$	0.917	0.598	1.53	0.151
400 5 0.5	$a_{123} X_1X_2X_3$	-0.894	0.598	-1.50	0.161
400 5 1.0	$a_{123} X_1X_2X_3$	-0.023	0.598	-0.04	0.970
400 10 0.0	$a_{123} X_1X_2X_3$	-0.917	0.598	-1.53	0.151
400 10 0.5	$a_{123} X_1X_2X_3$	0.894	0.598	1.50	0.161
400 10 1.0	$a_{123} X_1X_2X_3$	0.023	0.598	0.04	0.970
500 5 0.0	$a_{123} X_1X_2X_3$	-0.917	0.598	-1.53	0.151
500 5 0.5	$a_{123} X_1X_2X_3$	0.894	0.598	1.50	0.161
500 5 1.0	$a_{123} X_1X_2X_3$	0.023	0.598	0.04	0.970
500 10 0.0	$a_{123} X_1X_2X_3$	0.917	0.598	1.53	0.151
500 10 0.5	$a_{123} X_1X_2X_3$	-0.894	0.598	-1.50	0.161
500 10 1.0	$a_{123} X_1X_2X_3$	-0.023	0.598	-0.04	0.970

H.3 the effects of catalyst preparation parameters on the photocatalytic degradation of methyl orange under visible light irradiation that included adsorption

Table H.5 Estimated regression coefficients for the removal of methyl orange from the photocatalytic degradation under visible light irradiation that included adsorption

Term	Variables	Coefficients	Standard Error Coefficients	T-Value	P-Value
Constant	a_0	44.402	0.348	127.77	0.000*
A					
400	a_1X_1	-2.875	0.348	-8.27	0.000*
500	a_1X_1	2.875	0.348	8.27	0.000*
B					
5	a_2X_2	-2.114	0.348	-6.08	0.000*
10	a_2X_2	2.114	0.348	6.08	0.000*
C					
0.0	a_3X_3	-21.193	0.491	-43.12	0.000*
0.5	a_3X_3	3.512	0.491	7.15	0.000*
1.0	a_3X_3	17.681	0.491	35.98	0.000*
A*B					
400 5	$a_{12}X_1X_2$	-0.829	0.348	-2.39	0.034*
400 10	$a_{12}X_1X_2$	0.829	0.348	2.39	0.034*
500 5	$a_{12}X_1X_2$	0.829	0.348	2.39	0.034*
500 10	$a_{12}X_1X_2$	-0.829	0.348	-2.39	0.034*

(* p-value < 0.05)

Table H.5 (continue)

Term	Variables	Coefficients	Standard Error Coefficients	T-Value	P-Value
A*C					
400 0.0	$a_{13}X_1X_3$	3.744	0.491	7.62	0.000*
400 0.5	$a_{13}X_1X_3$	-2.646	0.491	-5.38	0.000*
400 1.0	$a_{13}X_1X_3$	-1.098	0.491	-2.23	0.045*
500 0.0	$a_{13}X_1X_3$	-3.744	0.491	-7.62	0.000*
500 0.5	$a_{13}X_1X_3$	2.646	0.491	5.38	0.000*
500 1.0	$a_{13}X_1X_3$	1.098	0.491	2.23	0.045*
B*C					
5 0.0	$a_{23}X_2X_3$	3.453	0.491	7.03	0.000*
5 0.5	$a_{23}X_2X_3$	1.470	0.491	2.99	0.011*
5 1.0	$a_{23}X_2X_3$	-4.923	0.491	-10.02	0.000*
10 0.0	$a_{23}X_2X_3$	-3.453	0.491	-7.03	0.000*
10 0.5	$a_{23}X_2X_3$	-1.470	0.491	-2.99	0.011*
10 1.0	$a_{23}X_2X_3$	4.923	0.491	10.02	0.000*
A*B*C					
400 5 0.0	$a_{123} X_1X_2X_3$	1.128	0.491	2.30	0.041*
400 5 0.5	$a_{123} X_1X_2X_3$	-0.780	0.491	-1.59	0.139
400 5 1.0	$a_{123} X_1X_2X_3$	-0.348	0.491	-0.71	0.492
400 10 0.0	$a_{123} X_1X_2X_3$	-1.128	0.491	-2.30	0.041*
400 10 0.5	$a_{123} X_1X_2X_3$	0.780	0.491	1.59	0.139
400 10 1.0	$a_{123} X_1X_2X_3$	0.348	0.491	0.71	0.492
500 5 0.0	$a_{123} X_1X_2X_3$	-1.128	0.491	-2.30	0.041*
500 5 0.5	$a_{123} X_1X_2X_3$	0.780	0.491	1.59	0.139
500 5 1.0	$a_{123} X_1X_2X_3$	0.348	0.491	0.71	0.492
500 10 0.0	$a_{123} X_1X_2X_3$	1.128	0.491	2.30	0.041*
500 10 0.5	$a_{123} X_1X_2X_3$	-0.780	0.491	-1.59	0.139
500 10 1.0	$a_{123} X_1X_2X_3$	-0.348	0.491	-0.71	0.492

H.4 the effects of catalyst preparation parameters on the photocatalytic degradation of methyl orange under visible light irradiation, excluding the adsorption

Table H.6 Estimated regression coefficients for the removal of methyl orange from the photocatalytic degradation under visible light irradiation, excluding the adsorption

Term	Variables	Coefficients	Standard Error Coefficients	T-Value	P-Value
Constant	a_0	39.106	0.353	110.66	0.000*
A					
400	a_1X_1	-2.881	0.353	-8.15	0.000*
500	a_1X_1	2.881	0.353	8.15	0.000*
B					
5	a_2X_2	-2.155	0.353	-6.10	0.000*
10	a_2X_2	2.155	0.353	6.10	0.000*
C					
0.0	a_3X_3	-18.412	0.500	-36.84	0.000*
0.5	a_3X_3	2.547	0.500	5.10	0.000*
1.0	a_3X_3	15.865	0.500	31.75	0.000*
A*B					
400 5	$a_{12}X_1X_2$	-0.570	0.353	-1.61	0.133
400 10	$a_{12}X_1X_2$	0.570	0.353	1.61	0.133
500 5	$a_{12}X_1X_2$	0.570	0.353	1.61	0.133
500 10	$a_{12}X_1X_2$	-0.570	0.353	-1.61	0.133

(* p-value < 0.05)

Table H.6 (continue)

Term	Variables	Coefficients	Standard Error Coefficients	T-Value	P-Value
A*C					
400 0.0	$a_{13}X_1X_3$	2.805	0.500	5.61	0.000
400 0.5	$a_{13}X_1X_3$	-1.629	0.500	-3.26	0.007*
400 1.0	$a_{13}X_1X_3$	-1.175	0.500	-2.35	0.037*
500 0.0	$a_{13}X_1X_3$	-2.805	0.500	-5.61	0.000*
500 0.5	$a_{13}X_1X_3$	1.629	0.500	3.26	0.007*
500 1.0	$a_{13}X_1X_3$	1.175	0.500	2.35	0.037*
B*C					
5 0.0	$a_{23}X_2X_3$	3.374	0.500	6.75	0.000*
5 0.5	$a_{23}X_2X_3$	1.442	0.500	2.89	0.014
5 1.0	$a_{23}X_2X_3$	-4.816	0.500	-9.64	0.000*
10 0.0	$a_{23}X_2X_3$	-3.374	0.500	-6.75	0.000*
10 0.5	$a_{23}X_2X_3$	-1.442	0.500	-2.89	0.014*
10 1.0	$a_{23}X_2X_3$	4.816	0.500	9.64	0.000*
A*B*C					
400 5 0.0	$a_{123} X_1X_2X_3$	0.994	0.500	1.99	0.070
400 5 0.5	$a_{123} X_1X_2X_3$	-1.135	0.500	-2.27	0.042*
400 5 1.0	$a_{123} X_1X_2X_3$	0.141	0.500	0.28	0.782
400 10 0.0	$a_{123} X_1X_2X_3$	-0.994	0.500	-1.99	0.070
400 10 0.5	$a_{123} X_1X_2X_3$	1.135	0.500	2.27	0.042*
400 10 1.0	$a_{123} X_1X_2X_3$	-0.141	0.500	-0.28	0.782
500 5 0.0	$a_{123} X_1X_2X_3$	-0.994	0.500	-1.99	0.070
500 5 0.5	$a_{123} X_1X_2X_3$	1.135	0.500	2.27	0.042*
500 5 1.0	$a_{123} X_1X_2X_3$	-0.141	0.500	-0.28	0.782
500 10 0.0	$a_{123} X_1X_2X_3$	0.994	0.500	1.99	0.070
500 10 0.5	$a_{123} X_1X_2X_3$	-1.135	0.500	-2.27	0.042*
500 10 1.0	$a_{123} X_1X_2X_3$	0.141	0.500	0.28	0.782

APPENDIX I

GRAPHS FROM STATISTICAL ANALYSIS

I.1 Pareto chart of the standardized effects for the main effects and the interaction effects of the three factors

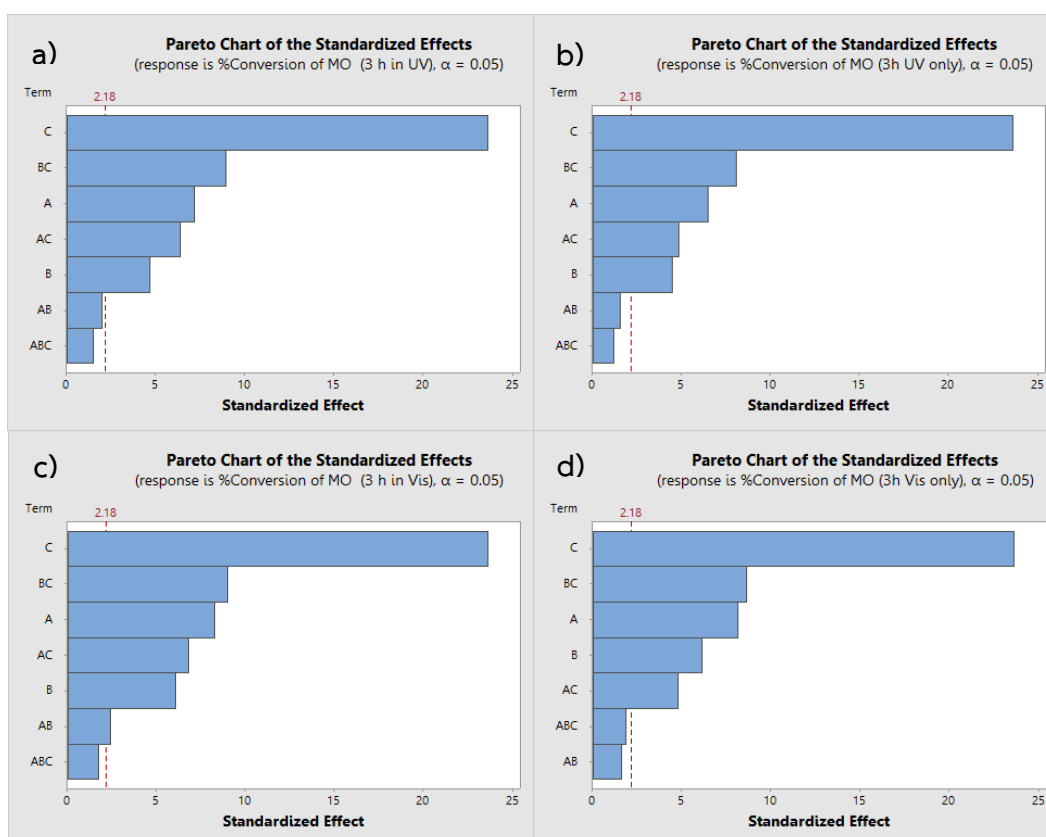


Figure I.1 Pareto chart of the standardized effects on the removal percentage of methyl orange under UV light irradiation that included adsorption (a); under UV light irradiation, excluding the adsorption (b); under visible light irradiation that included adsorption (c); under visible light irradiation, excluding the adsorption (d).

I.2 the plots of the effects of catalyst preparation parameters on the photocatalytic degradation of methyl orange under UV light irradiation that included adsorption

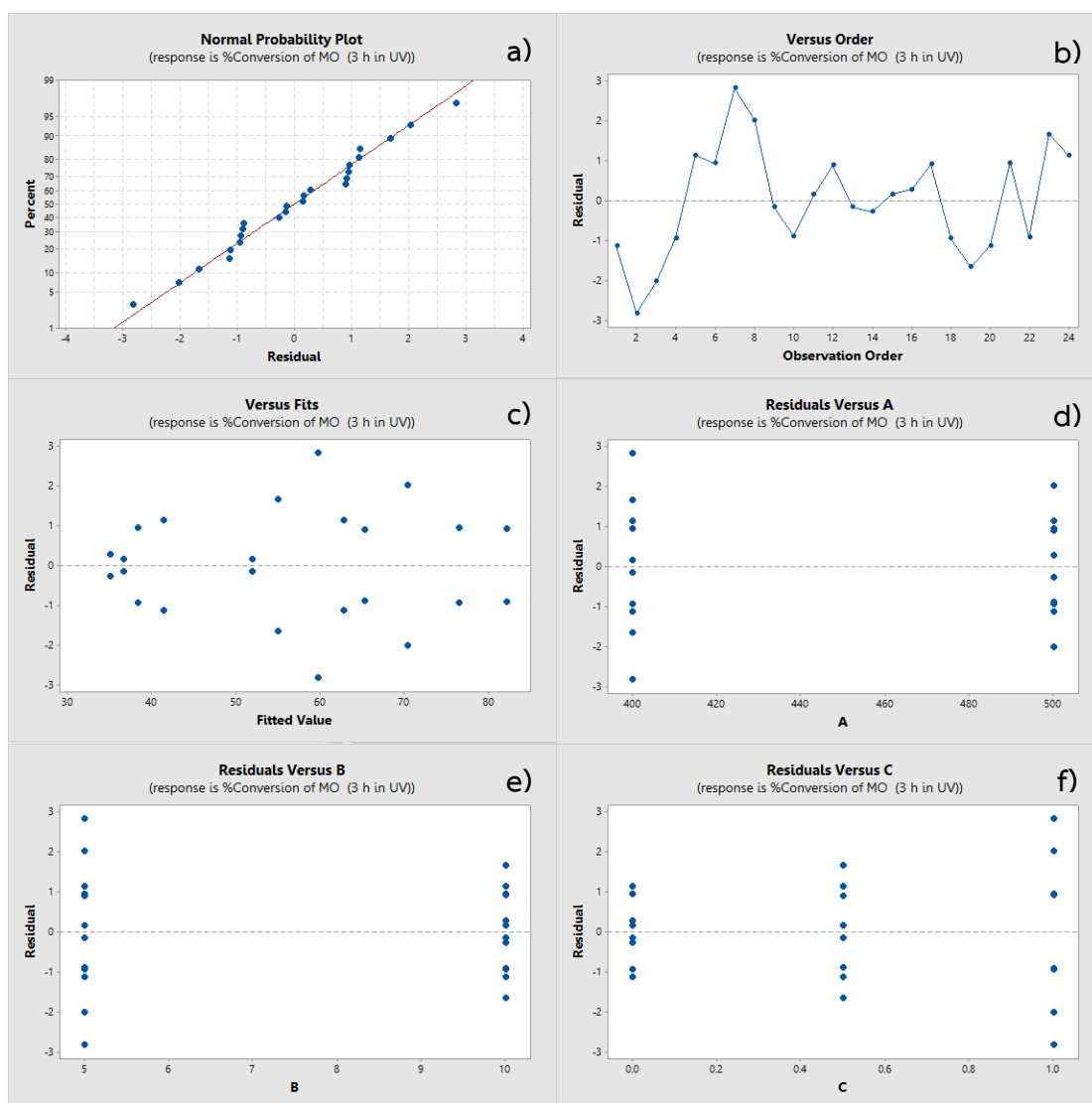


Figure I.2 The plot of normal probability of residuals (a); residuals versus observation order (b); residuals versus fits (c); residuals versus factor A (d); residuals versus factor B (e); residuals versus factor C (f) for the removal percentage of methyl orange under UV light irradiation that included adsorption

I.3 the plots of the effects of catalyst preparation parameters on the photocatalytic degradation of methyl orange under UV light irradiation, excluding the adsorption

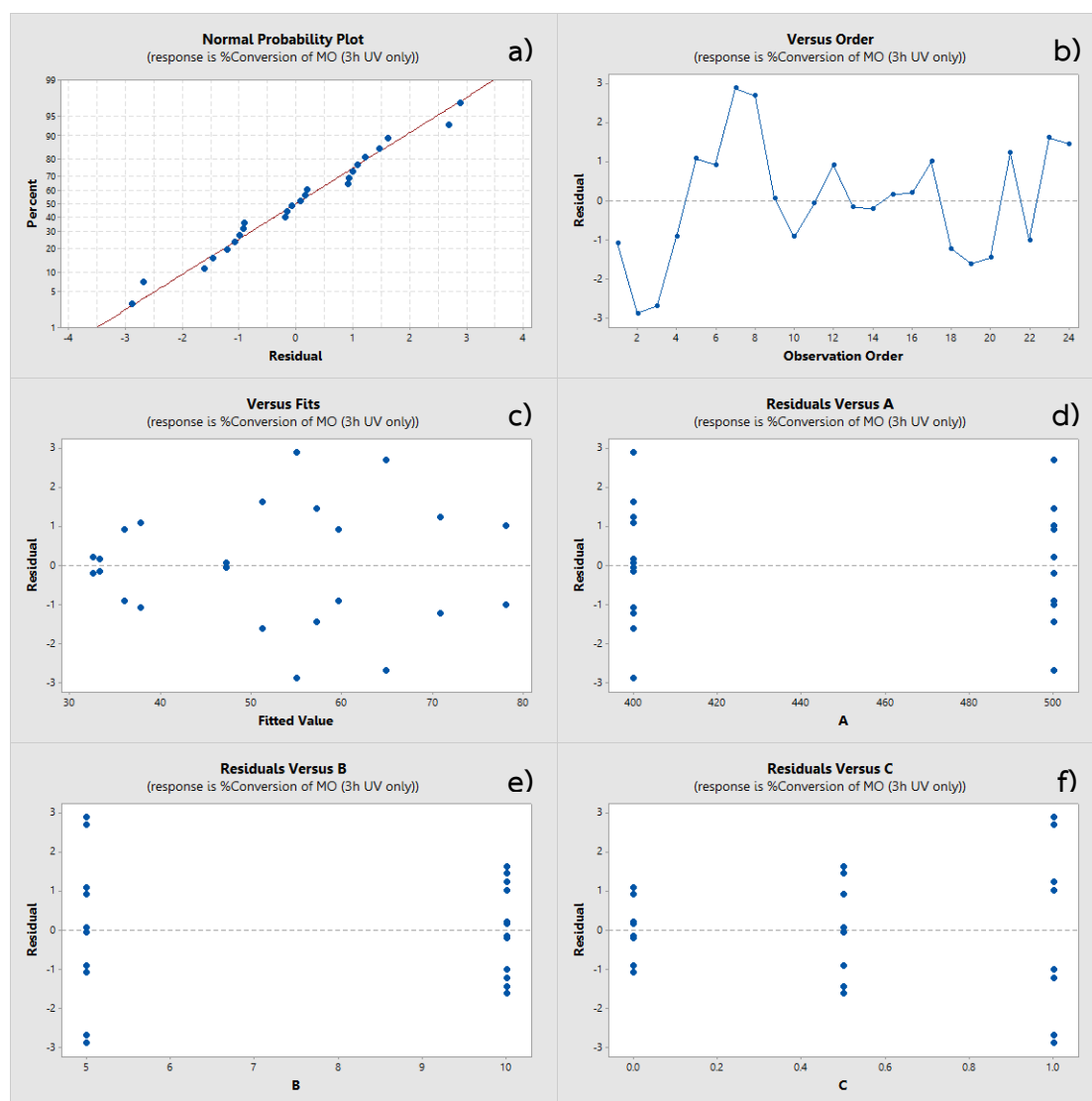


Figure I.3 The plot of normal probability of residuals (a); residuals versus observation order (b); residuals versus fits (c); residuals versus factor A (d); residuals versus factor B (e); residuals versus factor C (f) for the removal percentage of methyl orange under UV light irradiation, excluding the adsorption

I.4 the plots of the effects of catalyst preparation parameters on the photocatalytic degradation of methyl orange under visible light irradiation that included adsorption

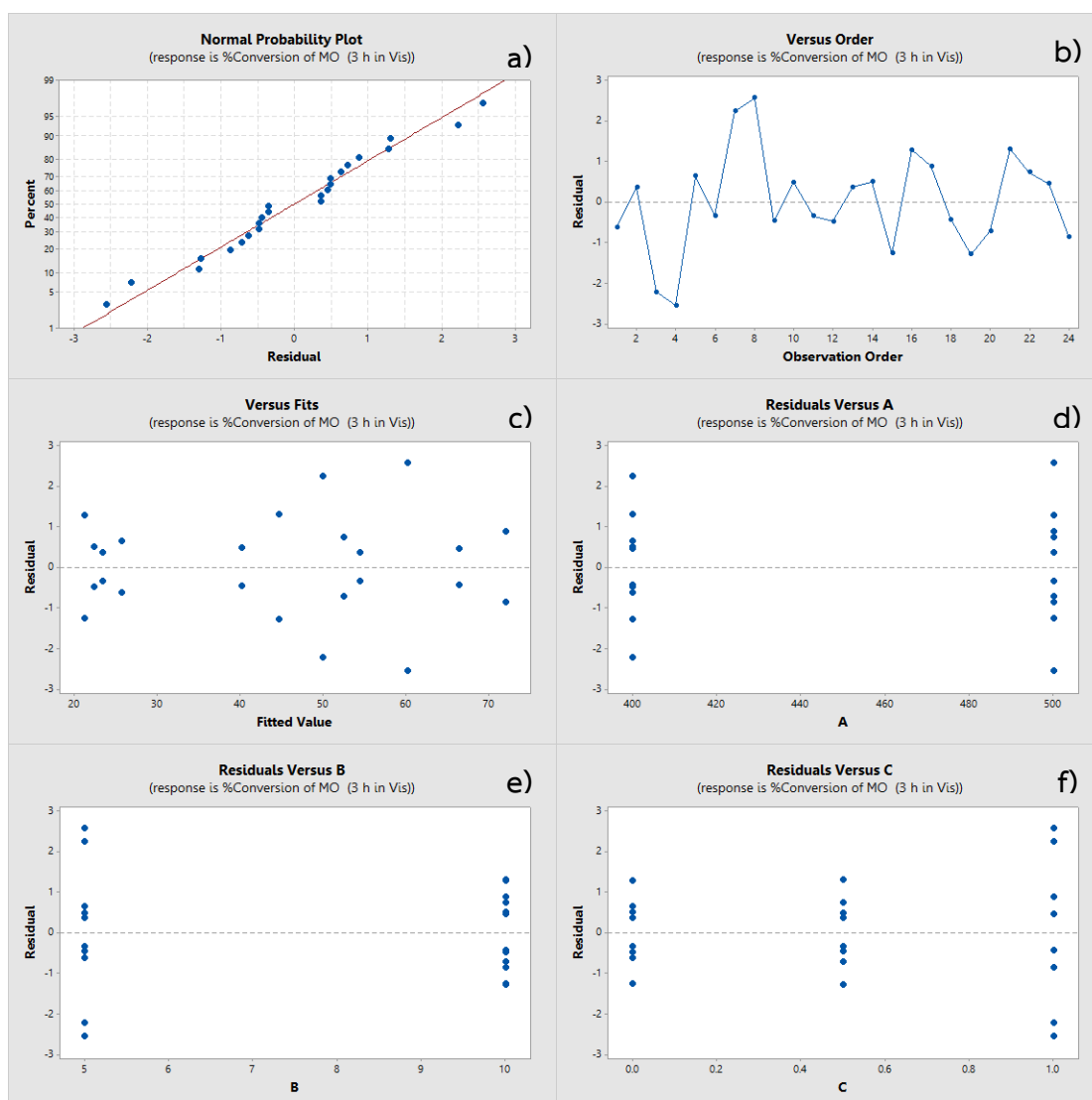


Figure I.4 The plot of normal probability of residuals (a); residuals versus observation order (b); residuals versus fits (c); residuals versus factor A (d); residuals versus factor B (e); residuals versus factor C (f) for the removal percentage of methyl orange under visible light irradiation that included adsorption

1.5 the plots of the effects of catalyst preparation parameters on the photocatalytic degradation of methyl orange under visible light irradiation, excluding the adsorption

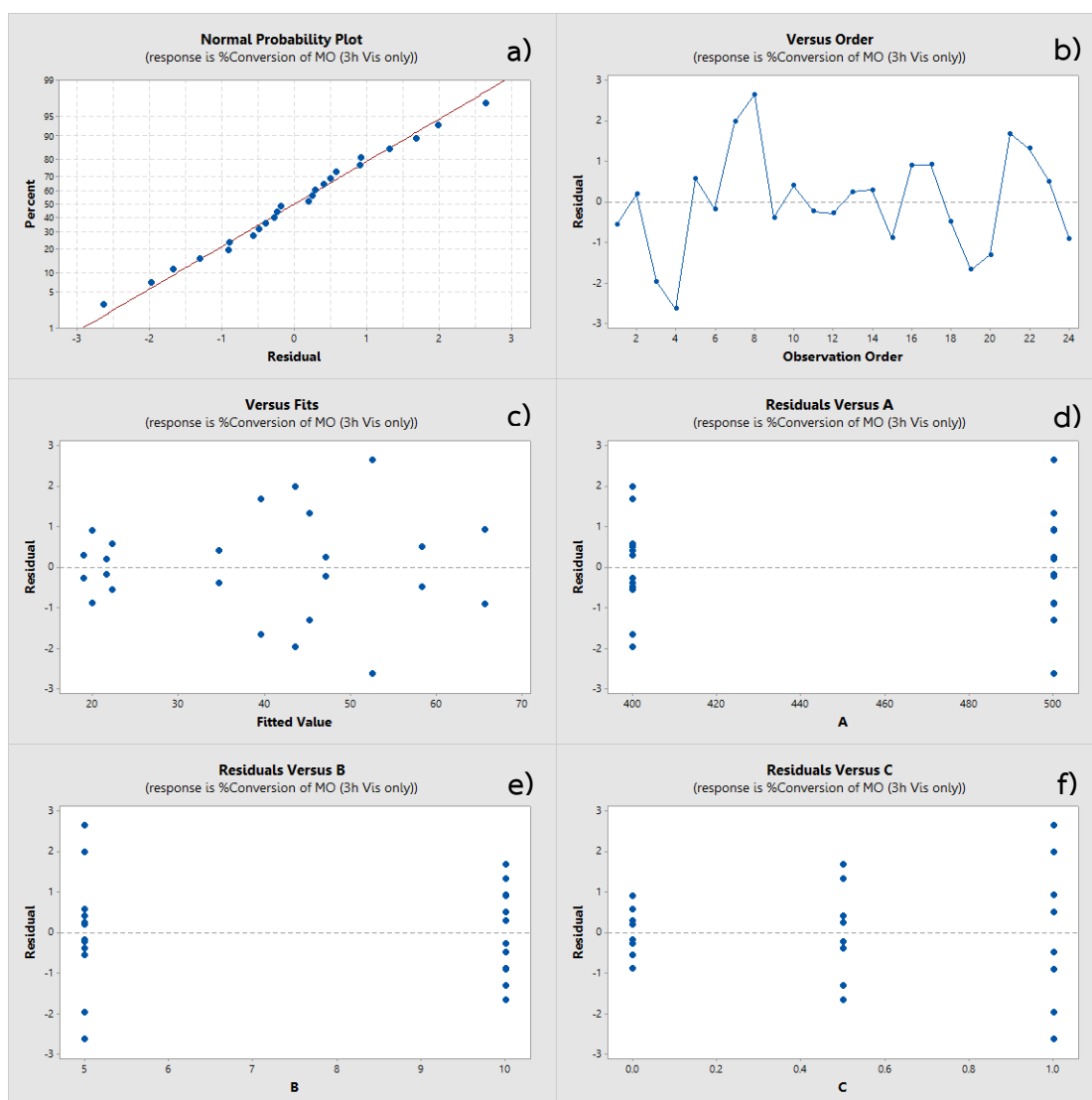


Figure I.5 The plot of normal probability of residuals (a); residuals versus observation order (b); residuals versus fits (c); residuals versus factor A (d); residuals versus factor B (e); residuals versus factor C (f) for the removal percentage of methyl orange under visible light irradiation, excluding the adsorption

VITA

NAME Saran Saensook

DATE OF BIRTH 16 March 1995

PLACE OF BIRTH Bangkok

INSTITUTIONS ATTENDED Bachelor Degree of Chemical Engineering from Faculty of Engineering, Mahidol University, Thailand in 2017
Master Study in the major in Chemical Engineering at Chulalongkorn University, Thailand in August 2017.

HOME ADDRESS 650 Moo 3 Jenjobthid road ,Naimueng Sub-district, Banphai district ,Khonkaen province 40110

PUBLICATION Saran Saensook and Akawat Sirisuk. Effect of calcination temperature and reducing agent used in the synthesis of black titanium dioxide on photocatalytic degradation of methyl orange. Proceeding of pure and applied chemistry international conference 2019; February 7-8, 2019; Bangkok International Trade and Exhibition Centre (BITEC), Bangkok, Thailand.